

THE CHANGES IN THE STRUCTURE OF GRAIN BOUNDARIES AND THEIR  
INFLUENCE ON THE ROOM TEMPERATURE DEFORMATION  
OF POLYCRYSTALS

by



Sandeep Sangal

A THESIS  
SUBMITTED TO THE FACULTY OF GRADUATE STUDIES  
IN PARTIAL FULFILLMENT OF THE REQUIREMENTS FOR THE DEGREE OF

DOCTOR OF PHILOSOPHY  
IN  
MECHANICAL ENGINEERING  
METALLURGY

DEPARTMENT OF MECHANICAL ENGINEERING  
UNIVERSITY OF MANITOBA  
WINNIPEG, MANITOBA  
CANADA

© 1988 Sandeep Sangal



National Library  
of Canada

Bibliothèque nationale  
du Canada

Canadian Theses Service    Service des thèses canadiennes

Ottawa, Canada  
K1A 0N4

The author has granted an irrevocable non-exclusive licence allowing the National Library of Canada to reproduce, loan, distribute or sell copies of his/her thesis by any means and in any form or format, making this thesis available to interested persons.

The author retains ownership of the copyright in his/her thesis. Neither the thesis nor substantial extracts from it may be printed or otherwise reproduced without his/her permission.

L'auteur a accordé une licence irrévocable et non exclusive permettant à la Bibliothèque nationale du Canada de reproduire, prêter, distribuer ou vendre des copies de sa thèse de quelque manière et sous quelque forme que ce soit pour mettre des exemplaires de cette thèse à la disposition des personnes intéressées.

L'auteur conserve la propriété du droit d'auteur qui protège sa thèse. Ni la thèse ni des extraits substantiels de celle-ci ne doivent être imprimés ou autrement reproduits sans son autorisation.

ISBN 0-315-51701-8

**THE CHANGES IN THE STRUCTURE OF GRAIN BOUNDARIES AND THEIR  
INFLUENCE ON THE ROOM TEMPERATURE DEFORMATION  
OF POLYCRYSTALS**

**BY**

**SANDEEP SANGAL**

A thesis submitted to the Faculty of Graduate Studies of  
the University of Manitoba in partial fulfillment of the requirements  
of the degree of

**DOCTOR OF PHILOSOPHY**

©      **1989**

Permission has been granted to the LIBRARY OF THE UNIVERSITY OF MANITOBA to lend or sell copies of this thesis, to the NATIONAL LIBRARY OF CANADA to microfilm this thesis and to lend or sell copies of the film, and UNIVERSITY MICROFILMS to publish an abstract of this thesis.

The author reserves other publication rights, and neither the thesis nor extensive extracts from it may be printed or otherwise reproduced without the author's written permission.

*Dedicated to Anna and Peter*



I hereby declare that I am the sole author of this thesis.

I authorize the University of Manitoba to lend this thesis to other institutions or individuals for the purpose of scholarly research.

Sandeep Sangal

I further authorize the University of Manitoba to reproduce this thesis by photocopying or by other means, in total or in part, at the request of other institutions or individuals for the purpose of scholarly research.

Sandeep Sangal

The University of Manitoba requires the signatures of all persons using or photocopying this thesis. Please sign below, and give address and date.

## ABSTRACT

During plastic deformation of polycrystals, grain boundaries interact with mobile lattice dislocations leading to the formation of so called *extrinsic grain boundary dislocations* (EGBDs). Since these dislocations are not a part of the equilibrium structure of grain boundaries, they lead to a *non-equilibrium grain boundary state*, i.e., a higher energy state. On annealing at high temperatures the annihilation of EGBDs occurs resulting in the equilibration of non-equilibrium grain boundary structure.

The major emphasis of this work has been to develop a description of the changes in the grain boundary structure and also the structure in the grain interior as a result of small plastic deformation and subsequent annealing over a wide range of temperatures. The resulting structural changes have then been correlated with the deformation behavior of polycrystals. For this purpose, detailed quantitative metallography and transmission electron microscopy (TEM) observations have been performed on 316L austenitic stainless steel specimens which were 2% pre-strained and subsequently annealed. The specimens were annealed at temperatures in the range of 500°C to 900°C for annealing times in the range of 1 to 30 minutes.

The above observations show that the EGBDs are annihilated at high temperatures without any significant

changes in the density or distribution of dislocations in the grain interior. Also, no detectable change in the grain size is observed as a result of the above annealing treatment. The results of the mechanical tests show that the recovery of yield stress in pre-strained specimens occurs in the range of annealing temperatures at which the annihilation of EGBDs occurs. Therefore, it has been concluded that the drop in yield stress is related to the annihilation of EGBDs, i.e., the transformation of non-equilibrium grain boundaries to their equilibrium state. A theoretical model has been proposed to predict the kinetics of transformation of non-equilibrium grain boundaries to equilibrium grain boundaries. The model assumes that the transformation involves the annihilation of EGBDs by climb via lattice diffusion of vacancies at the triple points. Due to the stress field of the EGBDs, there is a vacancy concentration gradient around the triple points. The profile of the vacancy concentration gradient has been obtained by assuming a steady state flux of vacancies. Using this vacancy concentration profile, the expressions for the rate of climb of EGBDs and the rate of their annihilation have been derived. The proposed model predicts that the time required for the equilibration of non-equilibrium grain boundaries is dependent not only on the annealing temperature but also on the initial density of EGBDs and the grain size of the polycrystal. It has been shown that the equilibration

behaviour predicted by the model is in good agreement with experimental results obtained for 316L stainless steel.

The grain size dependence of flow stress at room temperature in the regime of small strains (0 to 2%) has also been examined in annealed and 2% pre-strained and subsequently annealed polycrystals of 316L stainless steel. A Hall-Petch type of analysis was employed for grain sizes in the range of 3.4  $\mu\text{m}$  to 22.4  $\mu\text{m}$ . The analysis shows a linear increase in the Hall-Petch parameter  $\sigma_0(\epsilon)$  and a linear decrease in the Hall-Petch parameter  $K(\epsilon)$  with increasing strain in the annealed specimens. The increase in  $\sigma_0(\epsilon)$  has been associated with both, the work-hardening processes in the grain interior and the long range stress field of EGBDs. The EGBDs also act as sites of stress concentration, thereby making it easier to generate dislocations in the vicinity of grain boundaries. Therefore,  $K(\epsilon)$  which is a function of the stress required to generate dislocations, decreases with increasing strain in the early stages of plastic deformation. The observed drop in the flow stress as a result of annealing of pre-strained specimens has been related with the annihilation of dislocations at and in the vicinity of grain boundaries.

## ACKNOWLEDGEMENTS

I wish to express my sincere thanks to Professor K. Tangri for his patient guidance and constant encouragement throughout the course of this work. I would also like to thank Mr. Don Mardis, Mr. John Van Dorp and Mr. Roy Hartle for their valuable technical assistance. The cooperation and valuable discussions with Dr. K. Kurzydowski in this work is gratefully acknowledged. The support of my friends and colleagues: Rita, Rakesh, Fanny, Ken, John, Alok, Ravi, Aparna ..., has been a constant source of encouragement. Of these, my best friend and who is also my wife Rita deserves special mention for giving me support through the initial stages to the final preparation of this document.

Finally, the graduate fellowship granted by the University of Manitoba is gratefully acknowledged.

## TABLE OF CONTENTS

	<u>Page</u>
ABSTRACT	vi
ACKNOWLEDGEMENTS	ix
TABLE OF CONTENTS	x
LIST OF FIGURES	xiii
LIST OF TABLES	xvi
LIST OF SYMBOLS	xvii
 CHAPTER 1	
INTRODUCTION AND OBJECTIVES	1
 CHAPTER 2	
GRAIN BOUNDARY EFFECTS	6
2.1. THE GRAIN BOUNDARY ENERGY STATE	12
2.2. INTERACTION OF GRAIN BOUNDARIES WITH LATTICE DISLOCATIONS	16
2.3. THE INFLUENCE OF GRAIN SIZE AND STRUCTURE OF GRAIN BOUNDARIES ON THE MECHANICAL PROPERTIES OF POLYCRYSTALS	36
2.3.1. THE HALL-PETCH MODELS	36
2.3.2. THE EFFECT OF GRAIN BOUNDARY STRUCTURE	48
 CHAPTER 3	
EXPERIMENTAL PROCEDURE	60
3.1. THERMO-MECHANICAL TREATMENTS	60
3.2. TENSILE TESTS	64
3.3. TRANSMISSION ELECTRON MICROSCOPY	66
3.4. QUANTITATIVE METALLOGRAPHY	66

## CHAPTER 4

RESULTS AND DISCUSSION	71
4.1. THE RELATIONSHIP BETWEEN CHANGES IN GRAIN BOUNDARY STRUCTURE AND PROPERTIES OF POLYCRYSTALS	71
4.1.1. EXPERIMENTAL RESULTS	72
4.1.1.1. TENSION TEST RESULTS	74
4.1.1.2. METALLOGRAPHY MEASUREMENTS RESULTS	80
4.1.1.3. TRANSMISSION ELECTRON MICROSCOPY OBSERVATIONS	86
4.1.2. STRUCTURE-PROPERTY CORRELATION	94
4.2. A THEORETICAL MODEL FOR THE KINETICS OF TRANSFORMATION OF NON-EQUILIBRIUM GRAIN BOUNDARIES TO THEIR EQUILIBRIUM STATE	96
4.2.1. DEVELOPMENT OF THE MODEL FOR THE ANNIHILATION OF EGBDs	98
4.2.1.1. STRESS FIELD AT THE TRIPLE POINTS	101
4.2.1.2. VACANCY CONCENTRATION PROFILE AT THE TRIPLE POINTS	103
4.2.1.3. ANNIHILATION RATE OF EGBDs	107
4.2.2. CALCULATIONS	110
4.2.3. COMPARISON OF PREDICTED RESULTS WITH EXPERIMENTAL OBSERVATIONS	112
4.3. THE ROLE OF GRAIN BOUNDARIES IN THE GRAIN SIZE DEPENDENCE OF FLOW STRESS IN POLYCRYSTALS	120
4.3.1. EXPERIMENTAL RESULTS	121
4.3.1.1. SLIP LINE OBSERVATIONS	122
4.3.1.2. TENSION TEST RESULTS	124
4.3.1.2.1. AS-ANNEALED SPECIMENS	124
4.3.1.2.2. PRE-STRAINED AND ANNEALED (AT 550°C) SPECIMENS	127



	<u>Page</u>
4.3.1.2.3. PRE-STRAINED AND ANNEALED (AT 800°C) SPECIMENS	132
4.3.2. VARIATION OF $\sigma_o(\epsilon)$ WITH STRAIN	133
4.3.3. THE EFFECT OF EGBDs	134
4.3.4. VARIATION OF $K(\epsilon)$ WITH STRAIN	143
4.3.5. GRAIN SIZE DEPENDENCE OF THE WORK-HARDENING RATE	145
4.3.6. EFFECT OF PRE-STRAIN AND ANNEALING AT 550°C	146
4.3.7. EFFECT OF PRE-STRAIN AND ANNEALING AT 800°C	147
 CHAPTER 5	
CONCLUSIONS	151
REFERENCES	154
APPENDIX A	
IMPLEMENTATION OF METALLOGRAPHIC TECHNIQUES ON AN IMAGE ANALYSIS SYSTEM	160
APPENDIX B	
DERIVATION OF THE AVERAGE VACANCY CONCENTRATION NEAR THE TRIPLE POINTS	166

# LIST OF FIGURES

	<u>Page</u>
2.1. A symmetrical tilt and twist grain boundary	7
2.2. Measured relative energies as a function of misorientation angle	10
2.3. Three grain boundary planes meeting at a triple edge	15
2.4. An electron micrograph showing a grain boundary containing EGBDs, dislocation pile-ups	18
2.5. A schematic of the model for the spreading of a dislocation core	19
2.6. Splitting of a lattice dislocation into five boundary dislocations	22
2.7. Dissociation of a lattice dislocation into partial dislocations	23
2.8. Plots of the spreading temperature versus spreading time	27
2.9. Dependence of the mean spreading temperature of EGBDs on annealing temperature and time	29
2.10. Dependence of yield stress on the annealing temperature for a constant annealing time	31
2.11. EGBDs climb towards the triple points	33
2.12. Plots of flow stress as a function of $\ell^{-1/2}$ in $\alpha$ - iron	42
2.13. The variation of the Hall-Petch parameters $\sigma_0(\epsilon)$ and $K(\epsilon)$ as a function of strain in polycrystalline aluminum	54
2.14. The variation of $K(\epsilon)$ as a function of strain in 70:30 brass	56
2.15. Plots of $\sigma_0(\epsilon) - \sigma_0(\epsilon = 0)$ as a function of strain in $\alpha$ - brasses of varying Zn content	58
3.1. A schematic sketch of the multi-zone furnace and the temperature profile	63

	<u>Page</u>
3.2. A typical curve for the specimen temperature versus time	65
3.3. An optical micrograph of an annealed specimen of 316L stainless steel	68
3.4. A schematic of the measurement procedure for grain boundary length, dihedral angles and grain boundary curvature	70
4.1. Variation of yield stress as a function of annealing temperature in 316L stainless steel	76
4.2. Variation of yield stress as a function of annealing time in 316L stainless steel	78
4.3. Distribution of grain boundary lengths	81
4.4. Variation in grain boundary length, standard deviation of dihedral angles, fraction of curved grain boundaries and intercept length as a function annealing temperature	82
4.5. Distribution of dihedral angles	85
4.6. Distribution of intercept lengths	87
4.7. TEM micrographs for the as-annealed material	88
4.8. TEM micrographs for the 2% pre-strained material	89
4.9. TEM micrographs for specimens pre-strained and annealed at 600°C for 5 minutes	90
4.10. TEM micrographs for specimens pre-strained and annealed at 800°C for 5 minutes	91
4.11. A schematic of EGBDs at a grain boundary and the vacancy concentration profile	100
4.12. Variation of $\rho/\rho_0$ and yield stress as a function of annealing temperature in 316L stainless steel	114
4.13. Variation of $\rho/\rho_0$ and yield stress as a function of annealing time in 316L stainless steel	116
4.14. Optical micrographs of slip lines in 316L stainless steel	123

	<u>Page</u>
4.15. Stress-strain curves for the as-annealed specimens	125
4.16. Plots of flow stress versus $\ell^{-1/2}$	128
4.17. The variation of the Hall-Petch parameters $\sigma_0(\epsilon)$ and $K(\epsilon)$ with plastic strain $\epsilon$	129
4.18. Stress-strain curves for the as-annealed, pre-strained and annealed at 550°C and 800°C	131
4.19. Stress-field of EGBDs	140
A.1. Flow chart of the program developed for intercept length measurements	161
A.2. Logical combinations of the grain boundary image with grid lines	162
A.3. Processing of the image of grain boundaries	163
A.4. Flow chart of the program developed for the measurements of dihedral angles, grain boundary length and grain boundary curvature	165

## LIST OF TABLES

2.1. The Hall - Petch models	40
2.2. The calculated values of the stress required to generate dislocations at a pre-existing EGBD	51
3.1. The nominal composition of 316L stainless steel	61
3.2. Grain size measurements in specimens of 316L stainless steel	61
4.1. Thermo-mechanical histories of the 316L stainless steel specimens	73
4.2. Experimentally estimated values of the critical temperature	79
4.3. The results of the measurements of grain boundary length, dihedral angles, curvature and mean intercept length	83
4.4. An overview of the processes occurring as a function annealing temperature after a given pre-strain $\epsilon$	97
4.5. Values of material parameters for 316L stainless steel	111
4.6. Values of the constants A and B in equation (4.19) for specimens of different grain sizes	126
4.7. Estimated percentage annihilation of EGBDs as a function of grain size	149

## CHAPTER 1

### INTRODUCTION AND OBJECTIVES

The influence of grain boundaries on the deformation behaviour of polycrystals is a widely studied problem in physical metallurgy. The effects of grain boundaries on the properties of polycrystals can be broadly classified into two categories: 1) the grain size effects, and 2) the grain boundary structure effects. In a strict sense, these two effects cannot be treated in isolation as has often been the case in numerous studies in the past. The relationship between grain size and the mechanical properties of polycrystalline materials has been a subject of extensive experimental and theoretical investigations. But, a vast majority of these studies neglect the structural aspects of grain boundaries and explain the work-hardening behavior of polycrystals based on the following assumptions:

1. Grain boundaries act as an effective slip barrier and therefore the grain size determines the slip distance and consequently the mechanical properties.
2. Since the grains in a polycrystal are randomly oriented, the deformation in the individual grains must be such that the material continuity is maintained between adjacent grains.
3. As a consequence of the restraint due to the grain

boundaries, the deformation is inherently inhomogeneous, varying not only from grain to grain but also within individual grains.

The models developed to describe the dependence of flow stress on grain size of polycrystals (e.g., the dislocation pile-up models and the work-hardening models) based on the above assumptions which are essentially of a geometrical nature, ignore the changes in the grain boundary structure during plastic deformation (Balluffi, Komen and Schober 1972, Pond and Smith 1977, and Clark and Smith 1979). More recent studies have shown that the grain boundaries not only act as obstacles to dislocation movement, but also act as dislocation sources (Li 1963, Singh and Tangri 1970, Murr 1974 and 1975, and Malis and Tangri 1979) in the early stages of plastic deformation and as sinks (Valiev, Gertsman and Kaibyshev 1980, and Grabski, Valiev, Wyrzykowski and Lojkowski 1981) for lattice dislocations at elevated temperatures. The properties of the grain boundaries can be changed by introducing extrinsic defects (e.g., *extrinsic grain boundary dislocations*) in their structure. Grain boundaries containing these *extrinsic grain boundary dislocations* have a higher energy state leading to the so called *non-equilibrium state*. It has been shown that the presence of non-equilibrium grain boundaries can markedly affect the mechanical properties of metals and alloys. Though

there are numerous investigations which deal with the formation and annihilation of EGBDs, there are very few studies (Valiev et al 1980, and Grabski et al 1981) which attempt to correlate the behaviour of EGBDs with the overall deformation behavior of polycrystals. Therefore, the major emphasis of this work has been to develop a description of the changes in the grain boundary structure as a result of plastic deformation and subsequent annealing over a wide range of temperatures. The resulting structural changes at grain boundaries have been related to the plastic flow of polycrystals.

Chapter 2 examines some of the main grain boundary effects which occur as a result of plastic deformation and as a result of annealing of deformed materials. It is followed by a discussion on the possible influence of the changes in the grain boundary structure on the flow parameters of polycrystal deformation.

Chapter 3 outlines the various experimental procedures used in this study. The experimental procedures include *thermo-mechanical treatments, mechanical tests, transmission electron microscopy, and quantitative metallography.*

Chapter 4 presents the results of experimental and theoretical studies, followed by a discussion on the relationship between the micro-structural changes both within grains and at grain boundaries and the room temperature



deformation behavior in polycrystals of 316L austenitic stainless steel. The changes in the structure of grain boundaries due to plastic deformation and subsequent annealing have been described in terms of changes in the density and distribution of dislocations by TEM observations and in terms of the changes in the geometry of the grain boundary network by metallographic measurements. A theoretical model has also been proposed to predict the kinetics of the above changes. It has been shown that the quantitative predictions of the model are in agreement with experimental observations. Finally, the role of grain boundary structure on the flow stress of polycrystals of varying grain size has been examined by means of a Hall-Petch type of relationship. The Hall-Petch analysis is used to obtain the variation of the Hall-Petch parameters  $\sigma_0(\epsilon)$  and  $K(\epsilon)$  as a function of strain. This variation has been correlated with the changes in the grain boundary structure during plastic deformation.

In summary, the main objectives of this investigation may be listed as follows:

1. Description of the changes in the structure of grain boundaries as a result of the formation of EGBDs during plastic deformation and their annihilation on subsequent annealing.
2. The relationship between the changes in the grain

boundary structure and the flow stress of polycrystals in the range of small strains.

3. Development of a theoretical model to predict the kinetics of the annihilation of EGBDs as a result of annealing of deformed materials.
4. The role of grain boundary structure in the grain size dependence of flow stress in the early stages of plastic deformation at room temperature.

## CHAPTER 2

### GRAIN BOUNDARY EFFECTS

Grain boundaries, important microstructural elements in polycrystalline materials, have properties which are quite different from those of the grain interior. The specific properties of major concern here are the interaction of grain boundaries with dislocations under given external conditions of stress and temperature. These interactions play an important role in determining the mechanical properties (e.g., flow stress) of polycrystalline metals and alloys. In this chapter some of the key grain boundary effects and their influence on the mechanical properties have been reviewed.

A grain boundary delineates the region of contact between two crystals of different orientations as illustrated in figure (2.1). Figures (2.1a) and (2.1b) show two simple types of grain boundaries: the symmetrical tilt and the symmetrical twist respectively. A tilt grain boundary is formed when two crystals are rotated about an axis parallel to the plane of the boundary (see figure 2.1a). A twist grain boundary is formed when two crystals are rotated about an axis perpendicular to the plane of the boundary (see figure 2.1b). The angle of rotation  $\theta$  (shown in figures 2.1a and 2.1b) is the misorientation angle of the two crystals. In general, the misorientation relationship can be expressed by

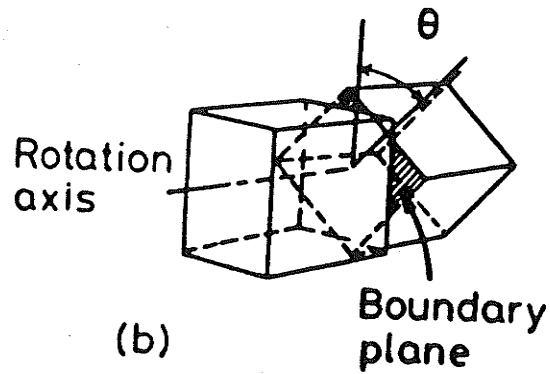
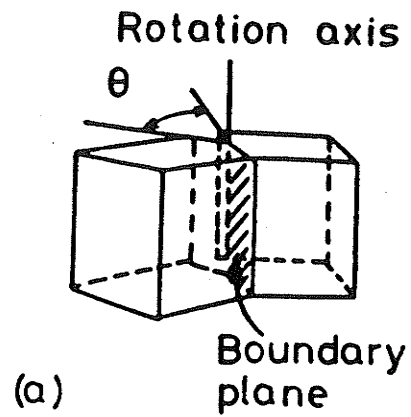
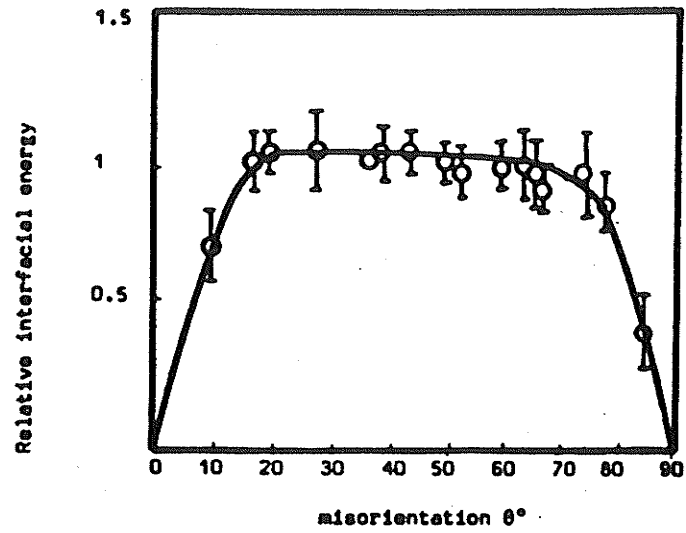


**Figure 2.1:** A symmetrical (a) tilt grain boundary, and (b) twist grain boundary formed as a result of rotations about axes parallel and perpendicular to the boundary plane respectively.

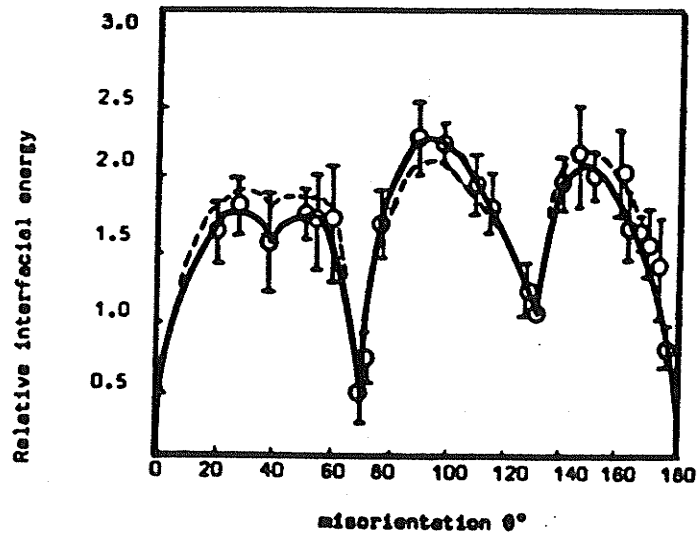
rotations about three mutually perpendicular axes. The rotations, given by  $\theta_x$ ,  $\theta_y$  and  $\theta_z$ , are known as the *misorientation parameters* between the two crystals. In figures (2.1a) and (2.1b), the grain boundary plane is located symmetrically with respect to the two crystals, i.e., parallel to the rotation axis in the case of the tilt boundary and perpendicular to the rotation axis in the case of the twist boundary. In general, the grain boundary plane may take up any arbitrary orientation resulting in an asymmetrical grain boundary. The orientation of a grain boundary plane can be described by rotations,  $\phi_y$  and  $\phi_z$  about two mutually perpendicular axes. These two rotations ( $\phi_y$  and  $\phi_z$ ) are known as the *orientation parameters* for a grain boundary. Since it is difficult to obtain a description of the grain boundary structure and its energy as a function of all the five parameters ( $\theta_x$ ,  $\theta_y$ ,  $\theta_z$ ,  $\phi_y$  and  $\phi_z$ ), three parameters ( $\theta_y$ ,  $\theta_z$  and  $\phi_y$ ) are usually kept constant. The variation in the energy of a grain boundary can therefore be expressed as a function of  $\theta$  and  $\phi$  only.

Several models have been developed to describe the structure of grain boundaries. Some of the models are: 1) dislocation models (Taylor 1934, Burgers 1940, Bragg 1940, Read and Shockley 1950, and Li 1961); 2) coincidence models (Kronberg and Wilson 1949, Frank 1950, Bollmann 1967, and 1970, Bollmann and Perry 1969, and Warrington and Bollmann

1972); 3) plane matching models (Pumphrey 1972, Balluffi and Schober 1972, and Ralph, Howell and Page 1977); and 4) polyhedral unit models (Weins, Chalmers, Gleiter and Ashby 1969, and Gleiter 1977). It may be mentioned that these models were initially proposed to explain the structure of low energy grain boundaries (low angle grain boundaries or special high angle grain boundaries). For example, the low angle grain boundaries can be adequately described by the dislocation model as developed by Taylor (1934), Burgers (1940), and Bragg (1940). The energy of low angle grain boundaries is computed from the dislocation theory based on linear elasticity. However, for grain boundaries with misorientations greater than approximately  $15^\circ$ , the dislocation cores overlap making it physically impossible to identify the individual dislocations. These grain boundaries have been termed as *random grain boundaries*. Whereas the low angle boundaries have large areas of undistorted atomic sites between the two crystal lattices, random grain boundaries contain large areas of poor fit between the two crystals. This leads to a relatively high energy for random grain boundaries. Figure (2.2a) shows an experimentally observed variation of energy for a tilt grain boundary as a function of the misorientation angle  $\theta$  in aluminum when the rotation axis is [100]. From the figure it can be seen that for low energy grain boundaries ( $\theta < 15^\circ$ ), the energy increases



(a)



(b)

**Figure 2.2:** Measured relative energies as a function of misorientation angle  $\theta$  of (a) [100] tilt boundaries and (b) [110] tilt boundaries in aluminum (Hasson and Goux 1971).

rapidly with increasing value of  $\theta$ . For most high angle grain boundaries ( $\theta > 15^\circ$ ), the energy is more or less independent of orientation. However, not all high angle grain boundaries are characterized by a highly disordered structure. There are some high angle grain boundaries termed as *special grain boundaries*, which have significantly lower energies than that of random grain boundaries. These boundaries occur at specific misorientations. Figure (2.2b) shows (in contrast to figure 2.2a) that when the rotation axis is  $[110]$ , there are several high angle orientations which have significantly lower energies than the random grain boundaries. Several investigations (Read and Shockley 1950, Li 1961, Bishop and Chalmers 1968, Chalmers and Gleiter 1971, Hasson and Goux 1971, and Pumphrey 1976,) have been carried out to explain the existence of these special grain boundaries. Read and Shockley (1950) originally proposed that if the orientation relationship between the two crystal lattices is such that the boundary consists of equally spaced dislocations, the energy of the boundary is relatively low. Based on this model quantitative predictions of the grain boundary energy have been made by Li (1961) and Hasson and Goux (1971). The low energy structure of special grain boundaries has also been explained (Bishop and Chalmers 1968 and Pumphrey 1976) based on the fact, that these boundaries consist of a high density of coincidence sites (atomic sites common to both crystal



lattices). The high density of the shared sites leads to the low energy of these coincidence grain boundaries.

It is neither necessary for the purposes of this thesis nor possible to discuss in detail the models which describe the structure of grain boundaries. However, for the sake of completeness a number of review articles and conference proceedings which cover this broad area quite comprehensively are listed as follows: Gleiter and Chalmers 1971, Chaudhari and Matthews 1972, Chadwick and Smith 1976, Johnson and Blakely 1979, Balluffi 1980, Gleiter 1982, and Valiev, Gertsman and Kaibyshev 1986. In the subsequent sections, the concept of the energy state of grain boundaries in annealed and in deformed polycrystalline materials has been discussed. The interaction of grain boundaries with lattice dislocations as a result of plastic deformation and annealing is examined. Finally, the influence of grain boundaries on the mechanical properties of polycrystals has been briefly reviewed.

## 2.1. THE GRAIN BOUNDARY ENERGY STATE

The grain boundary energy state is usually classified as an *equilibrium* or a *non-equilibrium state*. But a precise definition of the energy state of grain boundaries has not been possible as yet. The problem in defining the energy

state lies in the fact that the equilibrium or a reference state for any grain boundary is unknown. It should also be recognized that the grain boundary itself is a non-equilibrium crystal defect in a material. Therefore, a thermodynamic definition for an *equilibrium grain boundary state* can be given as follows: at a given temperature, external stress and chemical composition and for given crystallographic parameters, an equilibrated grain boundary has a minimum free energy and a *non-equilibrium grain boundary* will have an energy higher than that of the equilibrium grain boundary.

The non-equilibrium grain boundary state can be created by introducing defects in an equilibrium grain boundary. The grain boundary defects are of two types: 1) intrinsic and 2) extrinsic. The intrinsic defects, such as, the intrinsic grain boundary dislocations (IGBDs) are a necessary part of the grain boundary structure (Schober and Balluffi 1971 and Balluffi, Komen and Schober 1972) and do not give rise to long range stress fields. Therefore, the grain boundary remains in its low energy state. However, extrinsic grain boundary dislocations (EGBDs), the most commonly observed extrinsic defects (Balluffi et al 1972, Pond and Smith 1977, and Clark and Smith 1979) are not a part of the equilibrium structure of grain boundaries. Since EGBDs also possess long range stress fields (the significance of which in plastic

deformation will be a subject of considerable discussion in this work), the grain boundaries containing EGBDs are at a higher energy state or a non-equilibrium state. Section 2.2 deals in detail with the creation of EGBDs and their interaction with grain boundaries.

So far, the equilibrium and the non-equilibrium state has been considered for isolated grain boundaries. But, in polycrystalline materials, the grains are randomly oriented which gives rise to a range of misorientations between adjacent grains. The different misorientations may lead to the formation of both, high energy random grain boundaries and low energy special grain boundaries. The grain boundary network formed during annealing of polycrystals arranges itself in an overall low energy configuration. Figure (2.3) shows a sketch of three grain boundary planes meeting at a triple edge. For the configuration of figure (2.3) to be in equilibrium the boundary tensions  $\gamma_1$ ,  $\gamma_2$  and  $\gamma_3$  must be balanced. Mathematically, the equilibrium configuration can be expressed by the following relationship (Smith 1948):

$$\frac{\gamma_1}{\sin \alpha_{23}} = \frac{\gamma_2}{\sin \alpha_{13}} = \frac{\gamma_3}{\sin \alpha_{12}} \quad (2.1)$$

where  $\alpha_{23}$ ,  $\alpha_{13}$  and  $\alpha_{12}$  are the angles between the grain boundary planes. Thus, the equilibrium state of annealed polycrystals can now be defined as follows: the individual

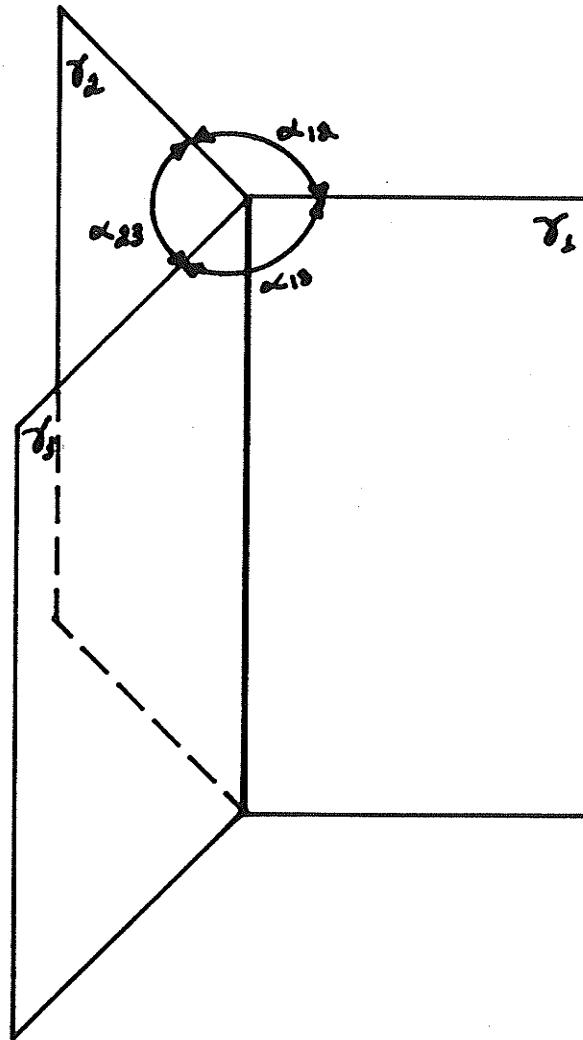


**Figure 2.3:** Three grain boundary planes meeting at a triple edge:  $\gamma_1$ ,  $\gamma_2$  and  $\gamma_3$  are the grain boundary energies; and  $\alpha_{23}$ ,  $\alpha_{13}$  and  $\alpha_{12}$  are the angles between the planes.

grain boundaries as well as the entire grain boundary network have a minimum energy; and the grain interior has an equilibrium density of dislocations which is typically in the range of  $10^6$  to  $10^7 \text{ cm}^{-2}$ . This definition of the equilibrium state will be used for polycrystals which have been annealed at sufficiently high temperatures for sufficiently long times.

## 2.2. INTERACTION OF GRAIN BOUNDARIES WITH LATTICE DISLOCATIONS

The interaction of grain boundaries with lattice dislocations occurs during recrystallization and during plastic deformation of materials. During recrystallization, migrating grain boundaries sweep up the dislocations in the deformed matrix (Grabski and Korski 1970 and Varin and Tangri 1980 and 1982). During plastic deformation, the mobile lattice dislocations interact with the grain boundaries (Balluffi et al 1972, Pond and Smith 1977, and Clark and Smith 1979). This interaction of a grain boundary with a dislocation creates a new line defect which was called by Balluffi et al (1972) as an *extrinsic grain boundary dislocation* (EGBD).

If the temperature of deformation is lower than  $0.2 T_m$  for pure metals and  $0.5 T_m$  for alloys, then the EGBDs retain their identity and their contrast is visible in the TEM

image. Figure (2.4) shows an electron micrograph of EGBDs visible on a grain boundary in 316L stainless steel after 2% plastic deformation. However, as the temperature is increased beyond a certain critical value (denoted as  $T_d$ ), the image of the EGBDs widens and eventually disappears. This phenomenon has been observed in a number of in-situ TEM observations (for example, Ishida, Hasegawa and Nagata 1968, Pumphrey and Gleiter 1975, and Lojkowski and Grabski 1979). The widening of the image of the EGBDs is believed to occur either by the process of delocalization or spreading of the cores of the EGBDs (Gleiter 1971, Ishida et al 1968, and Pumphrey and Gleiter 1974) or by the dissociation of EGBDs into partial dislocations with small Burgers vectors (Bollmann, Michaut and Sanifort 1972, Darby, Pond and Smith 1977, Schindler and Balluffi 1978, and Clark and Smith 1979).

The core delocalization or spreading model proposes that the dislocation core spreads out in the boundary plane as shown schematically in figure (2.5). Figure (2.5a) shows a lattice dislocation with a localized core approaching a grain boundary. Figure (2.5b) shows an extra-half plane introduced at the grain boundary. The core of the dislocation spreads out as shown in figure (2.5c). The driving force for the spreading process is the reduction in the energy. The reduction in the energy can be viewed in the following manner:

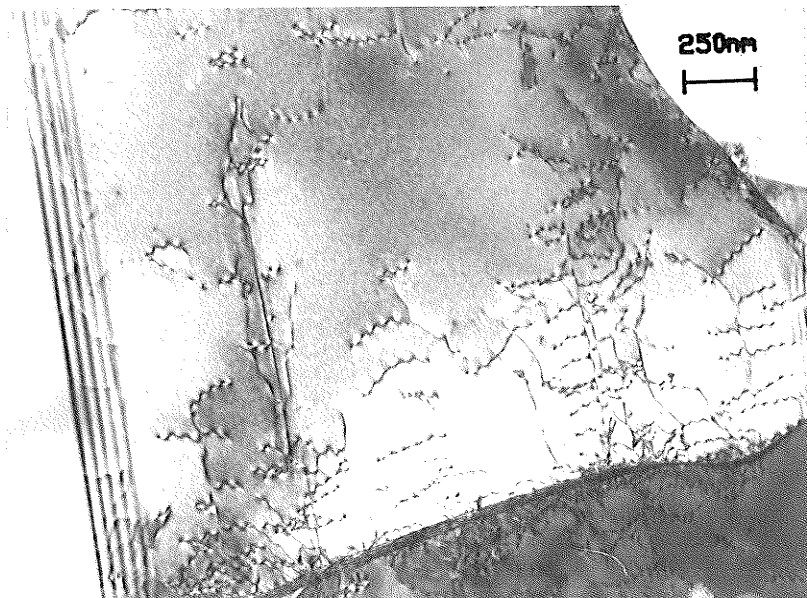
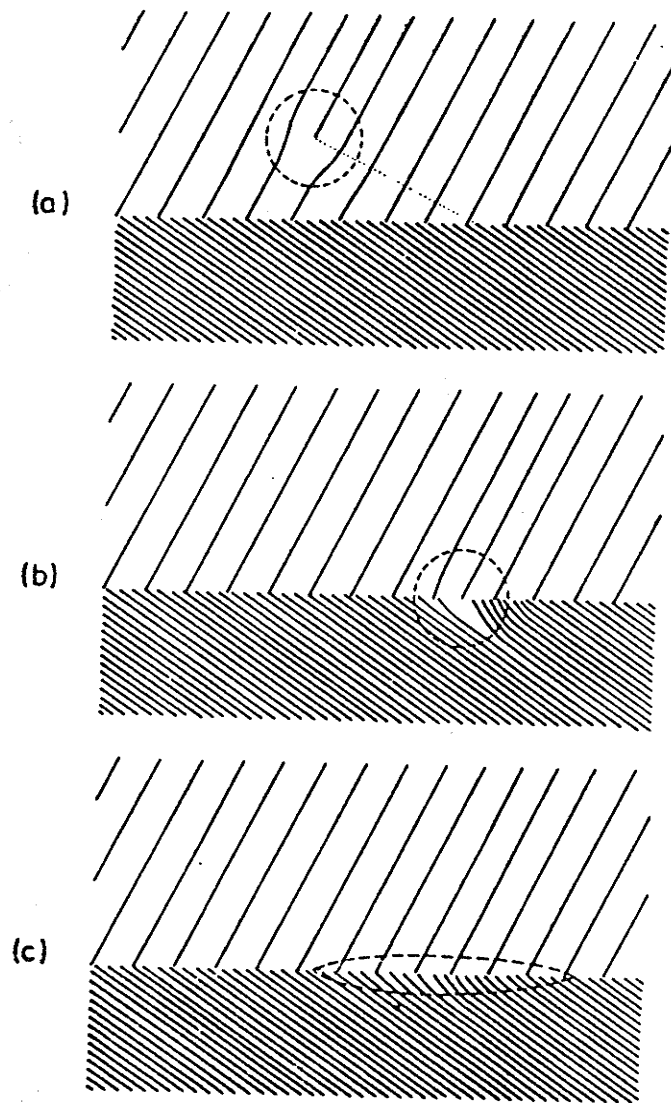


Figure 2.4: An electron micrograph showing a grain boundary containing EGBDs, dislocation pile-ups and/or emission profiles after 2% plastic deformation in 316L stainless steel of grain size  $3.4\ \mu\text{m}$ .



**Figure 2.5:** A schematic of the model for the spreading of a dislocation core: (a) a lattice dislocation with a localized core (circled) approaches a grain boundary and (b) introduces an extra half-plane at the boundary; (c) the strain energy is reduced by the spreading of the core (Pumphrey and Gleiter 1974).



The total energy of any dislocation is the sum of the elastic strain energy and the energy stored in the dislocation core. For example, the total energy of an edge dislocation can be written as (Hirth and Lothe 1982):

$$E_{\text{total}} = E_{\text{core}} + \frac{Gb^2}{4\pi(1-\nu)} \ln\left(\frac{R}{r'_0}\right) \quad (2.2)$$

where  $G$  is the shear modulus,  $b$  is the Burgers vector,  $\nu$  is the Poisson's ratio,  $R$  is the outer cutoff radius, and  $r'_0$  is the core radius. From equation (2.2), it is clear that the elastic strain energy decreases with increasing core size, i.e., increasing value of  $r'_0$ . Whereas, the energy stored in the dislocation core increases with increasing core size. The dislocation structure of minimum total energy corresponds to an equilibrium core size, i.e., the total energy in the elastic strain field and the dislocation core is a minimum. Thus, an EGBD in a highly ordered low energy grain boundary would remain stable since the process of spreading would require more energy than the energy gained in reducing the elastic strain field. TEM observations (Pumphrey and Gleiter 1974, Varin 1979, and Mori and Tangri 1979) made on low energy special grain boundaries show that the grain boundary dislocations are much more stable. However, in high energy random grain boundaries there is little long range order (as compared with special grain boundaries) and therefore the

system can reduce the total energy by spreading of the dislocation core. It is this reduction in the strain energy of the dislocation which causes the disappearance of the contrast in the electron microscope.

The dissociation model proposes that EGBDs split into partial dislocations with small Burgers vectors. Such a model appears to have a physical meaning in the case of a well defined boundary structure, e.g., special grain boundaries. An example of such a process is shown in the electron micrograph of figure (2.6). However, in the case of random grain boundaries there has been no evidence of the splitting of EGBDs into partial dislocations. Also, in these boundaries the Burgers vector of the partial dislocations would be so small that the concept no longer retains its physical significance. In such a case, the core spreading model can be equivalently represented by the dissociation model by an infinite number of dislocations of infinitesimal Burgers vectors (Darby, Schindler and Balluffi 1978).

Johannesson and Tholen (1972) derived the kinetics of spreading based on the dissociation model. The rate of dissociation was calculated by estimating the rate of separation of two partial dislocations, as shown in figure (2.7). The rate of separation being controlled by grain boundary diffusion, is given by

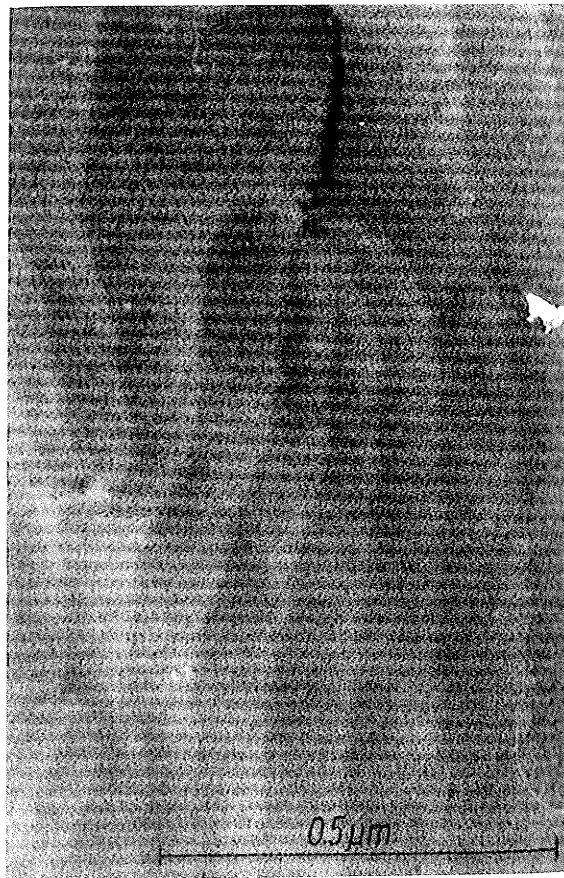
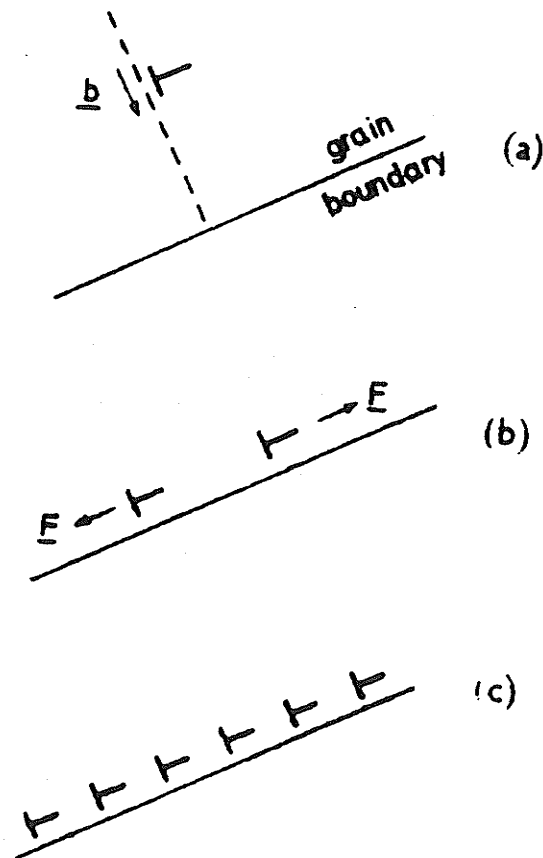


Figure 2.6: Splitting of a lattice dislocation into five boundary dislocations in a  $\Sigma = 39$  boundary in stainless steel (Bollmann, Michaut and Sanifort 1972).



**Figure 2.7:** Dissociation of a lattice dislocation into partial dislocations with small Burgers vector (Johannesson and Tholen 1972).

$$\frac{dS}{dt} = \frac{GbV.D^{gb}}{2\pi(1-\nu)kTS^2} \quad (2.3)$$

where  $S$  is the distance of separation between the two dislocations of Burgers vector  $b$ ,  $D^{gb}$  is the grain boundary self-diffusion coefficient,  $V$  is the atomic volume and  $k$  is the Boltzmann constant. By integrating equation (2.3), a relation between the spreading time ( $t_d$ ) and the spreading temperature ( $T_d$ ) for a given critical separation distance  $a$ , can be derived:

$$t_d = \frac{2\pi(1-\nu)k.a^3T_d}{3GbV.D^{gb}} \quad (2.4)$$

Since  $D^{gb} = D_o^{gb} \exp\left(-\frac{\Delta Q_{gb}}{RT_d}\right)$  (where  $D_o^{gb}$  is the frequency factor,  $\Delta Q_{gb}$  is the activation energy for grain boundary self-diffusion, and  $R$  is the gas constant), equation (2.4) can be re-written as

$$t_d = A.T_d \exp\left(\frac{\Delta Q_{gb}}{RT_d}\right) \quad (2.5)$$

$$\text{where } A = \frac{2\pi(1-\nu)k.a^3}{3GbV.D_o^{gb}} .$$

Lojkowski and Grabski (1981) derived another equation based on the assumption that the widened core of the

dislocation can be modeled by a continuous distribution of dislocations with infinitesimally small Burgers vectors. These infinitesimally small dislocations repel each other and by climbing spread out in the grain boundary plane. Assuming that grain boundary diffusion controls the rate of climb, they derived the following relationship between spreading time and the spreading temperature:

$$t_d = A \cdot T_d \exp \left( \frac{\Delta Q_{gb}}{RT_d} \right) \quad (2.6)$$

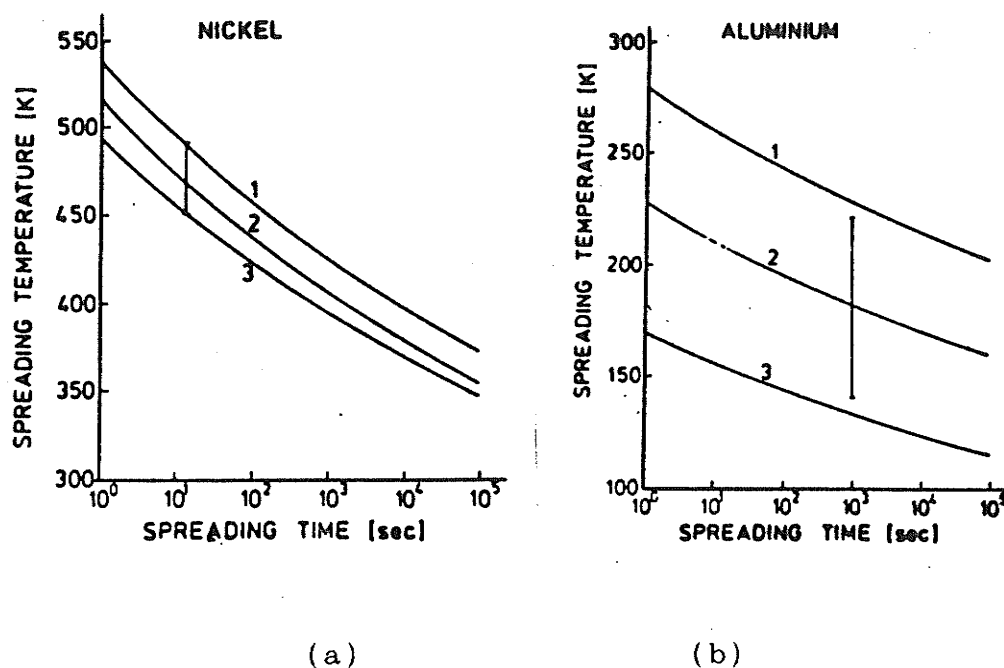
where  $A = \frac{10kT \cdot S^3}{GV\lambda \cdot D_o^{gb}}$ , and  $S$  is the dislocation core width and  $\lambda$  is the grain boundary width.

On examining equations (2.5) and (2.6) it can be seen that the two models discussed above yield similar kinetics for the spreading of EGBDs. The grain boundary width  $\lambda$  can be assumed to be in the range of  $4b$  to  $6b$  (approximately 10 to 15  $\text{\AA}$  for most materials). For  $\lambda = 4b$ , equation (2.6) predicts the spreading time  $t_d$  to be slightly higher than that predicted by equation (2.5). For  $\lambda = 6b$ , equation (2.6) predicts more or less the same spreading time  $t_d$  as predicted by equation (2.5). Thus, the experimentally observed spreading kinetics cannot be used to deduce the validity of either of the two models discussed above.

The disappearance of the EGBD contrast in the TEM image

is supposed to occur when the core width  $S$  reaches in the range of 1 to 2 extinction distances. Using equation (2.6), the calculated curves of spreading temperature  $T_d$  versus spreading time  $t_d$  for nickel and aluminum are shown in figure (2.8). The vertical bars in the figure represent the results of the measurements of spreading temperatures and times of EGBDs in polycrystalline nickel (Pumphrey and Gleiter 1974) and high purity polycrystalline aluminum (Lojkowski and Grabski 1979). Thus, it can be concluded that the disappearance kinetics of EGBDs predicted by equation (2.6) is in agreement with the experimental results.

However, the disappearance of the EGBD contrast does not imply their complete annihilation, i.e., the complete recovery of the non-equilibrium structure of grain boundary. The complete annihilation of EGBDs requires that their Burgers vector must go to zero. Neither the core spreading model nor the dissociation model discussed above can explain the recovery of non-equilibrium grain boundaries on annealing at high temperatures. On a boundary of finite length containing a certain density of EGBDs, the spreading of the cores cannot continue indefinitely. The spreading process must stop after a finite core width is reached. The final core width being dependent on (a) the equilibrium core width determined by the structure of grain boundary and/or (b) the interaction between adjacent spread out EGBDs (Varin,



The following diffusion data has been used to calculate the above curves:

Nickel (polycrystals)

curve 1:  $\lambda D_0 = 8.75 \times 10^{-10}$  and  $\Delta Q = 118.4 \text{ kJ.mol}^{-1}$   
 curve 2:  $\lambda D_0 = 5.00 \times 10^{-10}$  and  $\Delta Q = 111.4 \text{ kJ.mol}^{-1}$   
 curve 3:  $\lambda D_0 = 3.50 \times 10^{-10}$  and  $\Delta Q = 114.8 \text{ kJ.mol}^{-1}$

Aluminum (bicrystals)

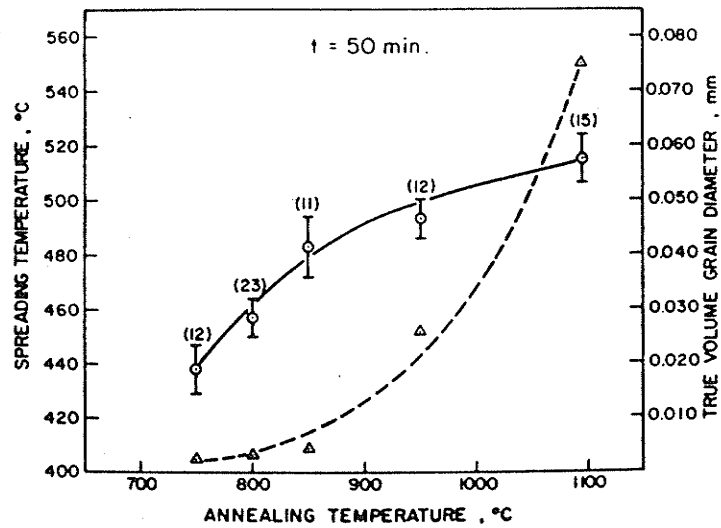
curve 1:  $\lambda D_0 = 7.00 \times 10^{-8}$  and  $\Delta Q = 76.0 \text{ kJ.mol}^{-1}$   
 curve 2:  $\lambda D_0 = 1.70 \times 10^{-10}$  and  $\Delta Q = 36.0 \text{ kJ.mol}^{-1}$   
 curve 3:  $\lambda D_0 = 1.6 \times 10^{-9}$  and  $\Delta Q = 52.0 \text{ kJ.mol}^{-1}$

**Figure 2.8:** Plots of the spreading temperature versus spreading time for (a) nickel and (b) aluminum; the bars indicate the experimental values (Lojkowski and Grabski 1981).

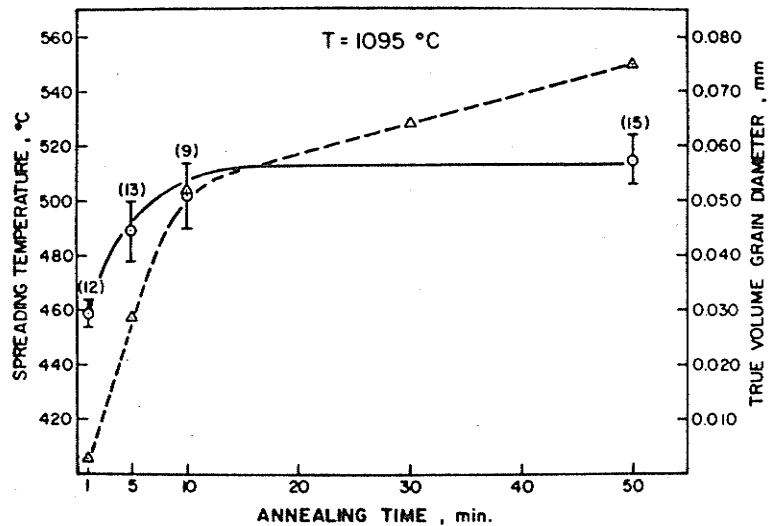


Kurzydowski and Tangri 1987). As discussed earlier, the equilibrium core width will be small on special grain boundaries and large on random grain boundaries. Also, higher the density of EGBDs on a given grain boundary, smaller would be the widening of their cores.

Experimental observations (Varin and Tangri 1982, Valiev, Gertsman and Kaibyshev 1980, and Grabski, Valiev, Wyrzykowski and Lojowski 1981) also show that grain boundaries remain in a non-equilibrium state even after the image of the EGBDs is no longer visible in the electron microscope. Varin and Tangri (1982) made use of the spreading temperature as an indicator of the state of the grain boundaries after annealing of heavily deformed specimens. Low values of the spreading temperature indicate that the grain boundaries are in a non-equilibrium state (Pumphrey and Gleiter 1974 and 1975, and Varin and Tangri 1980). Figure (2.9a) shows the variation of the spreading temperature (solid line) and the grain diameter (broken line) as a function of annealing temperature at a constant annealing time of 50 minutes in cold-worked specimens of an austenitic stainless steel. The measured spreading temperature of  $438^{\circ}\text{C}$  after annealing at  $750^{\circ}\text{C}$  is significantly lower than the measured value of  $515^{\circ}\text{C}$  after annealing at  $1095^{\circ}\text{C}$ . This implies that the grain boundaries after annealing at  $750^{\circ}\text{C}$  are in a non-equilibrium state, i.e., the strain field of the



(a)



(b)

**Figure 2.9:** Dependence of the mean spreading temperature of EGBDs (solid line) and the true volume grain diameter (broken line) on (a) the annealing temperature and (b) the annealing time of cold worked specimens of austenitic stainless steel; numbers in the bracket indicate the number of boundaries employed for each data point (Varin and Tangri 1982).

EGBDs has not been annihilated. Beyond the annealing temperature of  $750^{\circ}\text{C}$  (see figure 2.9a) the increase in the spreading temperature indicates the onset of the equilibration of grain boundaries. From figure (2.9b), it can be seen that the spreading temperature becomes constant beyond an annealing time of 10 minutes for a constant annealing temperature of  $1095^{\circ}\text{C}$ . This implies that an annealing time of 10 minutes is sufficient for the equilibration of grain boundaries at this temperature.

The above observations are in agreement with the investigation (Grabski et al 1981) on the changes in the yield stress as a result of equilibration of grain boundaries. The results of the investigation are plotted in figure (2.10) which shows the dependence of yield stress on the annealing temperature at a constant annealing time of 5 minutes for 1% pre-strained specimens of 310 stainless steel. In-situ TEM observations show that the image of the EGBDs disappears at a temperature of 735 K ( $462^{\circ}\text{C}$ ). But the yield stress remains more or less unchanged up to annealing temperatures of 770 K ( $497^{\circ}\text{C}$ ). Thus, it can be concluded that the structure of grain boundaries remains essentially unchanged after the spreading of EGBDs. Figure (2.10) also shows that yield stress recovery takes place on annealing at a temperature of  $897^{\circ}\text{C}$ . But the TEM observations (Grabski et al 1981) showed no change in the density of dislocations

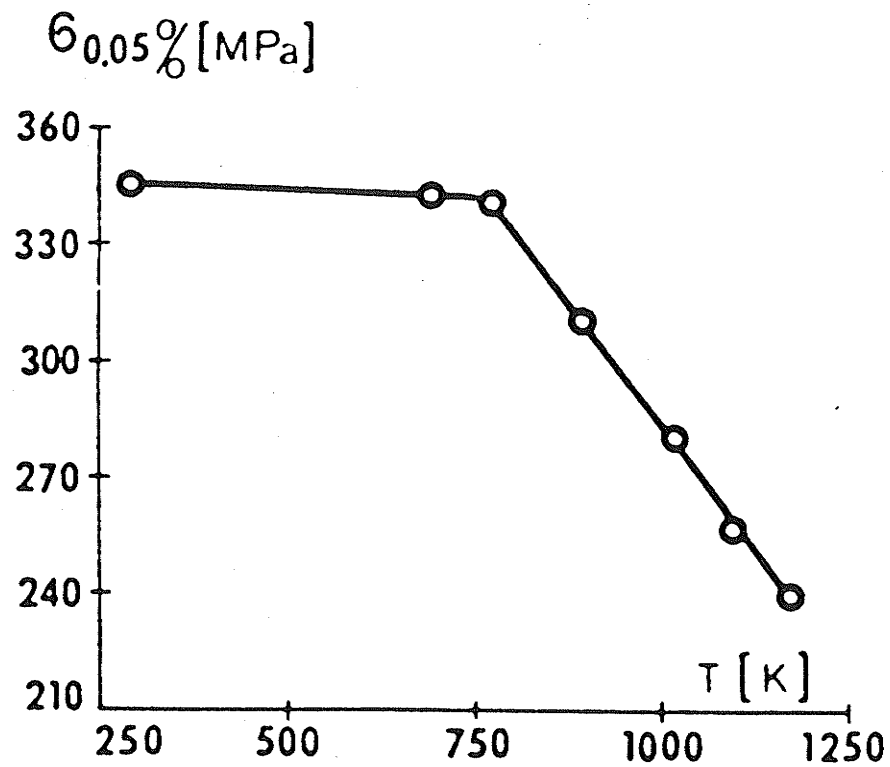


**Figure 2.10:** Dependence of yield stress on the annealing temperature for a constant annealing time of 5 minutes in 1% pre-strained specimens of 310 stainless steel of grain size  $7.0 \mu\text{m}$  (Grabski, Valiev, Wyrzykowski and Lojkowski 1981).

inside the grains. Therefore, it was concluded that the recovery of the grain boundary structure must be responsible for the recovery of yield stress.

From the above discussion it is evident that after the dislocations have spread out, some other micro-mechanism must be initiated to explain the phenomenon of recovery of non-equilibrium grain boundary structure. A model proposed by Varin and Kurzydowski (1983) attempts to explain the recovery of non-equilibrium grain boundaries. Their model assumes that the annihilation of EGBDs occurs via climb accompanied by plastic deformation at the triple points. The resulting plastic deformation at the triple points is accommodated by volume diffusion of vacancies, as shown in figure (2.11). The deformation rate  $\dot{\epsilon}$ , during accommodation by volume diffusion has been assumed to follow the equation for Nabarro-Herring type diffusional creep derived by Ashby (1971):

$$\dot{\epsilon} = \frac{20\sigma VD}{kT \cdot \ell^2} \quad (2.7)$$

where the stress  $\sigma$  near a triple point is assumed to be given by

$$\sigma = \frac{Gb\rho}{2\pi(1-\nu)} \quad (2.8)$$

and  $D_s$  is the lattice self-diffusion coefficient,  $\ell$  is the

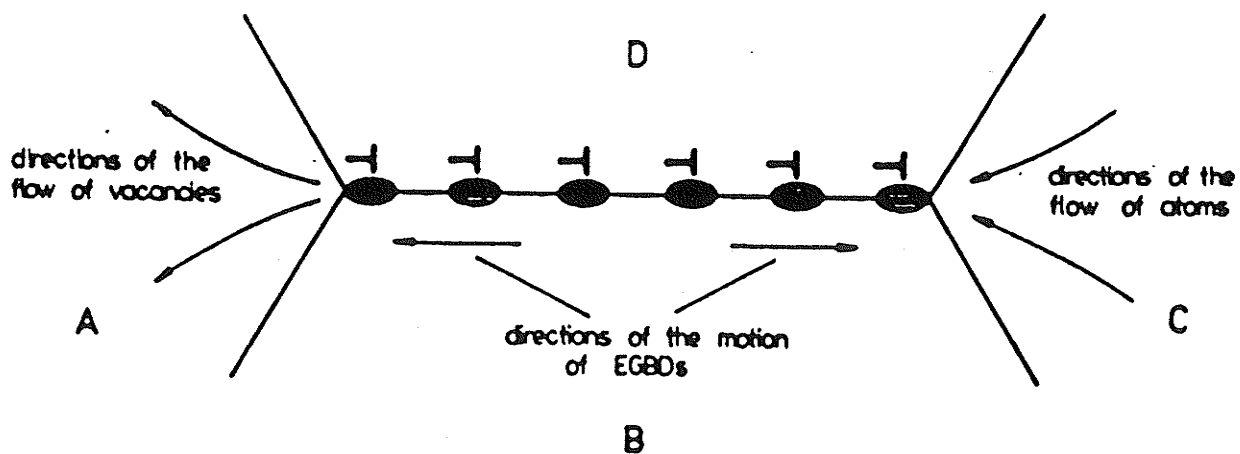


**Figure 2.11:** GGBDs climb towards the triple points as a result of volume diffusion of vacancies (Varin and Kurzydowski 1983).

grain size and  $\rho$  is the density of EGBDs. Relating the deformation rate  $\dot{\epsilon}$  to the annihilation rate of EGBDs, they derived the following relation between annealing time and temperature required for the equilibration of non-equilibrium grain boundaries (equilibration process being assumed to be completed when the density of EGBDs drops below 10% of the initial density):

$$t = \frac{2.3kT\pi(1-\nu)\ell^2}{20GVD_s} \quad (2.9)$$

The authors did not attempt to relate the annihilation process with other changes in microstructure (e.g., changes in the vicinity of grain boundaries). The predicted results were reported to be in agreement with some experimental results on the equilibration of grain boundaries obtained in a deformed austenitic stainless steel (Varin 1982). However, equation (2.9) is unable to explain the experimental results shown in figures (2.9) and (2.10). For heavily deformed stainless steel specimens the recovery of grain boundaries occurs at an annealing temperature of 1095°C at an annealing time of 10 minutes (see figure 2.9b). Whereas equation (2.9) predicts a much larger annealing time of 92 minutes at this annealing temperature. Similarly, for the 1% deformed specimens the time required to equilibrate the grain boundaries is 5 minutes at an annealing temperature of 897°C

(see figure 2.10), while equation (2.9) predicts an annealing time of 96 minutes (approximately 20 times larger than that obtained experimentally). The above calculations were made by using the following values of the parameters in equation (2.9):  $k = 1.18 \times 10^{-23} \text{ J.K}^{-1}$ ;  $\nu = 0.283$ ;  $V = 8.38 \times 10^{-30} \text{ m}^3$ ;  $G = 8.43 \times 10^{10} \text{ N.m}^{-2}$ ; and the grain sizes  $\ell$  were taken as  $52.0 \text{ }\mu\text{m}$  (read from the broken curve in figure 2.8b) and  $7.0 \text{ }\mu\text{m}$  (given in figure 2.9).

It is suggested that this lack of correlation between the experimental results is due to the following reasons:

1. The assumption of the stress near a triple point given by equation (2.8) is valid only for a dislocation pile-up and not for the dislocation configuration shown in figure (2.11) (the configuration can be better approximated by the dislocation arrangement in a tilt boundary).
2. The predicted values of the equilibration time and temperature are independent of the starting density of EGBDs (see equation 2.9). This appears to be somewhat unrealistic. It can be seen from the experimental observations that the equilibration time and temperature are much higher for the heavily deformed material (figure 2.9) than for the material deformed to small strains (figure 2.10).
3. It may also be pointed out that the physical process



of the EGBD annihilation shown by the authors in figure (2.11) is incorrect. The direction of the motion of the EGBDs shown in the figure requires that the vacancies flow inwards (towards the triple point) rather than outwards as shown in region A.

In view of the above mentioned discrepancies, a new model (to be discussed in chapter 4) has been proposed which also takes into account changes in the microstructure to the annihilation of EGBDs as a result of annealing at elevated temperatures.

### 2.3. THE INFLUENCE OF GRAIN SIZE AND STRUCTURE OF GRAIN BOUNDARIES ON THE MECHANICAL PROPERTIES OF POLYCRYSTALS

#### 2.3.1. THE HALL-PETCH MODELS

Since the original work by Hall (1951) and Petch (1953), there have been several models proposed to describe the influence of grain size on the yield and flow stress of metals and alloys. In general, a vast majority of data in literature (e.g., Armstrong, Codd, Douthwaite and Petch 1962, Fujita and Tabata 1973, Meakin and Petch 1974, Lloyd 1980, and Hansen and Ralph 1982) shows that the variation in the yield and flow stress with grain size follows a Hall-Petch type of relationship:

$$\sigma(\epsilon) = \sigma_0(\epsilon) + K(\epsilon)\ell^{-1/2} \quad (2.10)$$

where  $\sigma(\epsilon)$  is the flow stress,  $\ell$  is the grain size and  $\sigma_0(\epsilon)$  and  $K(\epsilon)$  are constants at a given strain  $\epsilon$ .

Deviations from the Hall-Petch relationship have also been reported (Grange 1966, Morrison 1966, Abrahamson 1970, Fujita and Tabata 1973, Thompson 1975 and 1977, and Lloyd 1980) for some materials under certain grain size range and testing conditions. These deviations have been usually observed in the range of fine grain sizes (less than 5.0  $\mu\text{m}$ ). The experimental data on fine grained aluminum and aluminum alloys, and nickel (Thompson 1975 and Lloyd 1980) exhibits one of the following features: 1)  $\ell^{-1}$  instead of  $\ell^{-1/2}$  dependence of  $\sigma(\epsilon)$ ; 2) two slopes in the Hall-Petch plots ( $\sigma(\epsilon)$  versus  $\ell^{-1/2}$ ). Stress-strain curve crossings (Thompson 1977) have also been observed in fine grained (3.4  $\mu\text{m}$ ) and coarse grained (150  $\mu\text{m}$ ) polycrystals of copper.

The above results have been explained on the basis that fine grained materials develop a highly inhomogeneous distribution of dislocations (a high density of dislocations in the vicinity of grain boundaries). However, the experimental data for such fine grained materials is scarce and also shows a larger scatter. This makes it difficult to arrive at a unique explanation on the deformation behavior. The situation is further complicated by the fact that there may be differences in the microstructure of fine and coarse

grain sized specimens. The microstructural differences include texture, dislocation density and distribution, grain boundary structure and grain size distribution. Specimen thickness is also an important factor which may have a significant effect on the reported data. As shown by Miyazaki, Shibata and Fujita (1979), specimen thickness is critical for materials with low stacking fault energy (SFE) where as many as 50 grains are required in the thickness direction to obtain a representative polycrystal deformation behavior. Thus, in order to understand the deformation behavior of these ultra fine-grained materials well documented experimental data is necessary which at present is rather scarce.

The various attempts made to rationalize the Hall-Petch relationship can be broadly classified into two categories:

1. The dislocation pile-up models (Hall 1951, Petch 1953, Cottrell 1958, and Armstrong et al 1962) : These models are based on a concept of pile-up of dislocations at a grain boundary. The models assume that the flow stress of a polycrystal is controlled by the pile-up stress causing propagation of slip across grain boundaries.
2. The work-hardening models (Conrad 1963, Kocks 1970, Ashby 1970, Thompson, Baskes and Flanagan 1973, and Mecking 1981) : The models in this category propose

that the flow stress is governed by the accumulation of dislocations in the grains. The flow stress is taken to be proportional to the square root of the density of dislocations.

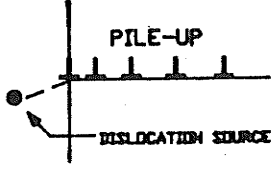
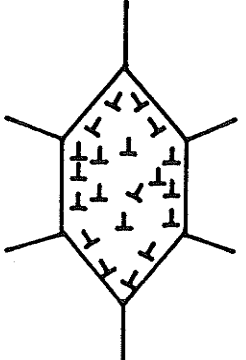
These two types of models are discussed in detail below and their main features are also summarised in Table (2.1).

The basic idea underlying the *dislocation pile-up model* is that the stress concentration produced by a pile-up of dislocations at a grain boundary activates dislocation sources in the neighbouring grain. The stress at the head of the pile-up is proportional to the density of dislocations (number per unit length) in the pile-up, which in turn is expected to be proportional to the grain size. This leads to the grain size dependence of flow stress. Based on this concept, Armstrong et al (1962) proposed that if  $\tau_c$  is the critical stress required to operate a dislocation source at a distance  $r$  from the grain boundary (see figure in Table 2.1) then  $K(\epsilon)$  in equation (2.10) is given by the following equation:

$$K(\epsilon) = m^2 \tau_c r^{1/2} \quad (2.11)$$

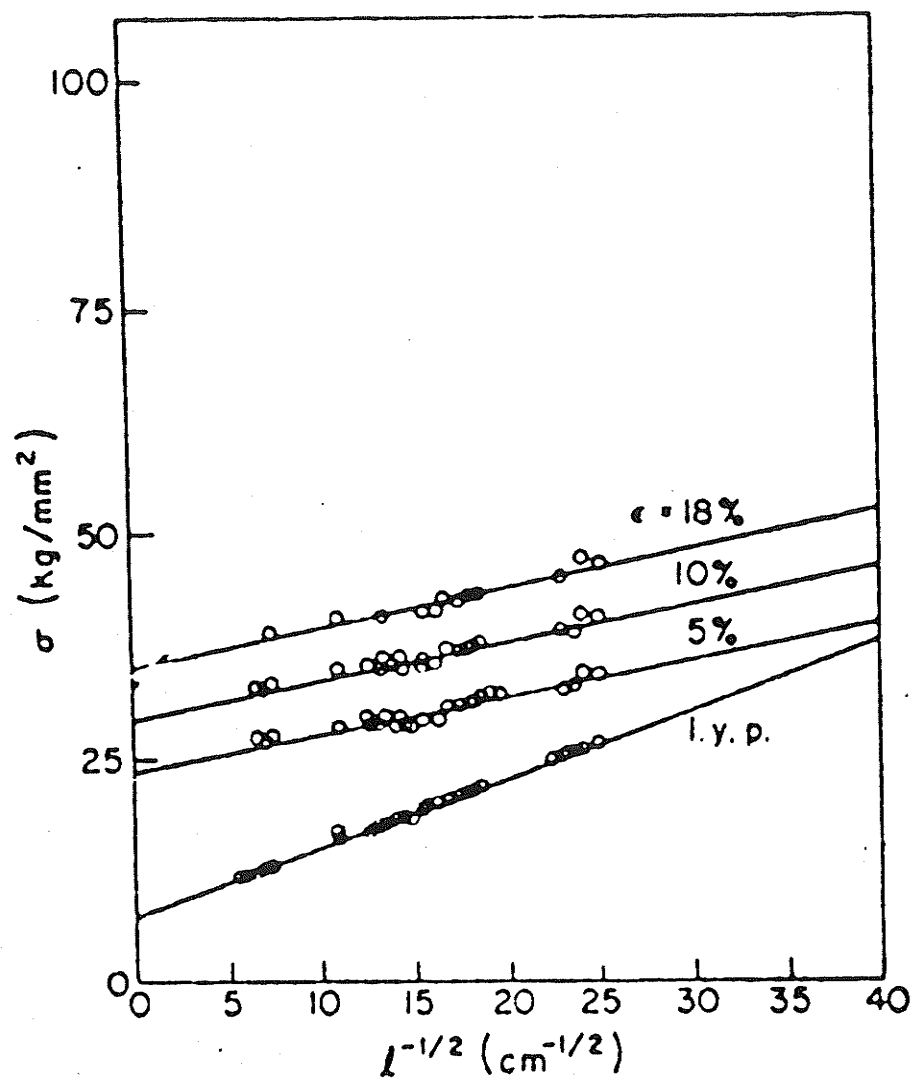
where  $m$  is the Taylor orientation factor. From equation (2.11), it can be deduced that  $K(\epsilon)$  would increase if  $\tau_c$  increases (i.e., increase in the difficulty of operating a dislocation source) during plastic deformation. Generation of unlocked dislocation sources during deformation would

TABLE 2.1  
The Hall - Petch models

<p>DISLOCATION PILE-UP MODELS (Hall 1951 Petch 1953 Cottrell 1958 Armstrong et al 1962)</p> 	<p>Flow stress is controlled by the pile-up stress at GBs causing propagation of slip in the neighbouring grain. From <u>Armstrong et al (1962)</u>:</p> $\sigma(\epsilon) = \sigma_o(\epsilon) + m^2 \tau_c r^{1/2} \ell^{-1/2}$ <p><math>m</math> = orientation factor <math>\tau_c</math> = stress required to activate a dislocation source</p>	<p><math>\sigma_o(\epsilon)</math> = friction stress. <math>K(\epsilon) = m^2 \tau_c r^{1/2}</math> <math>\tau_c</math> is expected to vary with strain which in turn would lead to the variation of <math>K(\epsilon)</math> with strain.</p>
<p>WORK-HARDENING MODELS (Conrad 1963 Ashby 1970 Thompson et al 1973)</p> 	<p><u>Original Model by Conrad (1963)</u>:</p> $\epsilon = \beta(\rho b \ell) \quad \text{gives,}$ $\sigma(\epsilon) = \sigma_o(\epsilon) + \alpha G b \left( \frac{\epsilon}{b \beta} \right)^{1/2} \ell^{-1/2}$	<p>Predicts a parabolic <math>\sigma - \epsilon</math> curve <math>K(\epsilon) \propto \epsilon^{1/2}</math>, continuously increases with strain.</p>
	<p><u>Ashby (1970)</u>:</p> $\sigma(\epsilon) = \sigma_o(\epsilon) + \alpha G b (\rho_g + \rho_s)^{1/2}$ $\rho_g = C_1 \epsilon / b \lambda_g; \quad \rho_g \gg \rho_s$ $\sigma(\epsilon) = \sigma_o + \alpha G b \left( \frac{C \epsilon}{b} \right)^{1/2} \ell^{-1/2}$	<p>Predicts a parabolic <math>\sigma - \epsilon</math> curve <math>K(\epsilon) \propto \epsilon^{1/2}</math> Model emphasizes dislocation activity in the vicinity of grain boundaries.</p>
	<p><u>Thompson et al (1973)</u>:</p> <p>Each grain regarded as a composite consisting of a hard mantle zone and a soft grain interior</p> $\sigma(\epsilon) = \sigma_o + \left( 1 - \frac{\lambda_s}{\ell} \right) \frac{K_1}{\lambda_s} + \frac{\lambda_s}{\ell} \left( \frac{K_2}{\ell^{1/2}} \right)$ <p><math>K_1</math> and <math>K_2</math> are experimental constants.</p>	<p><u>Small strains</u>: GB contribution dominates Predicts a decreasing <math>K(\epsilon)</math> with strain. <u>Large strains</u>: Grain interior contribution dominates. <math>\sigma(\epsilon) \propto \ell^{-1}</math></p>

decrease  $\tau_c$ , thereby resulting in a decrease in  $K(\epsilon)$  as a function of strain. The effect of unlocking of dislocation sources on  $K(\epsilon)$  can be easily understood in materials like annealed  $\alpha$  - iron which exhibit a yield point because dislocations are locked by the Cottrell mechanism. Figure (2.12) shows the plots of flow stress as a function of the inverse of the square root of grain size at various strain levels for room temperature deformation of  $\alpha$  - iron. The plots show that the value of  $K(\epsilon)$  (given by the slopes of the lines in figure 2.12) decreases sharply on deformation beyond the lower yield point. This decrease in  $K(\epsilon)$  has been associated with both the newly created dislocation sources and the unpinning of the previously locked dislocation sources. In the case of fcc materials where the yield point is normally absent because there is little dislocation locking,  $K(\epsilon)$  has been observed to show an initial increase up to a certain strain level and on further straining it is observed to decrease. The decrease in  $K(\epsilon)$  beyond a certain strain has been usually ascribed to the onset of recovery processes (e.g., Lloyd 1980). A more detailed discussion on the factors which influence the variation of  $K(\epsilon)$  with strain is discussed in section (2.3.2).

$\sigma_o(\epsilon)$  is interpreted as the friction stress in the grain interior. It is expected to vary with strain as a result of dislocation accumulation and interaction within the grains.



**Figure 2.12:** Plots of flow stress as a function of  $l^{-1/2}$  in  $\alpha$  - iron deformed to different strain levels at room temperature (Armstrong et al 1962).

The work-hardening in the grain interior has been approximated (Armstrong et al 1962) to the mono - crystal hardening (Hirsch 1975) where similar dislocation interactions occur. The relationship between the hardening in the grain interior of polycrystals and the mono-crystal hardening can be obtained by the following relationships:

$$\sigma(\epsilon) = m\tau(\gamma) \quad (2.12)$$

and

$$\epsilon = \frac{\gamma}{m} \quad (2.13)$$

where  $m$  is the average orientation factor,  $\tau$  and  $\gamma$  are the resolved shear stress and shear strain respectively. From equations (2.12) and (2.13), the work-hardening in the grain interior is related to the work-hardening in mono-crystals by the following equation:

$$\frac{d\sigma_o}{d\epsilon} = m^2 \cdot \frac{d\tau}{d\gamma} \quad (2.14)$$

A discussion on the validity of the above equation in terms of microstructural changes is given in section (2.3.2).

The concept of *work-hardening* to explain the Hall-Petch relationship was first proposed by Conrad (1963). The model is based on the well known experimental observation that flow stress of polycrystals can be described by the equation:



$$\sigma(\epsilon) = \sigma_o + \alpha Gb \sqrt{\rho} \quad (2.15)$$

where  $\sigma_o$  is the friction stress,  $\alpha$  is a constant factor,  $G$  is the shear modulus and  $\rho$  is the density of dislocations in the grains. Assuming that the density of dislocations is inversely proportional to the grain size, Conrad derived the following equation:

$$\sigma(\epsilon) = \sigma_o + \alpha Gb \left( \frac{\epsilon}{b\beta} \right)^{1/2} \ell^{-1/2} \quad (2.16)$$

where  $\beta$  is a constant. Equation (2.16) predicts a parabolic stress-strain curve and therefore can be used to describe the variation of flow stress with grain size in only a limited number of materials, e.g., Nb (Conrad 1967).

Ashby (1970) extended the work-hardening approach to take into account the inhomogeneous nature of plastic deformation within the individual grains. He suggested that the process of work-hardening can be understood in terms of statistically stored dislocations  $\rho_s$  and geometrically necessary dislocations  $\rho_g$  (see figure in Table 2.1). By a simple arithmetic addition of the two densities,  $\rho_g$  (given by  $\frac{C_1 \epsilon}{b\lambda_g}$ ) and  $\rho_s$  (given by  $\frac{C_2 \epsilon}{b\lambda_s}$ ), and using equation (2.15) Ashby derived a relation for the flow stress:

$$\sigma(\epsilon) = \sigma_o + \alpha Gb (\rho_g + \rho_s)^{1/2} = \sigma_o + \alpha Gb \left( \frac{C_1 \epsilon}{b\lambda_g} + \frac{C_2 \epsilon}{b\lambda_s} \right)^{1/2} \quad (2.17)$$

where  $\lambda_g$  and  $\lambda_s$  are the slip distances for the geometrically necessary and the statistically stored dislocations, and  $C_1$  and  $C_2$  are constants. In general,  $\rho_s$  can be neglected because  $\rho_g$  is much higher than  $\rho_s$ . Therefore, equation (2.17) reduces to the Hall-Petch relationship given by equation (2.10). As in the case of equation (2.16), equation (2.17) also predicts a parabolic stress-strain dependence.

Thompson et al (1973) suggested that since the geometrically necessary dislocations are concentrated in the grain boundary vicinity, each grain can be regarded as a composite consisting of a hard mantle zone and a soft grain interior. The contributions from the two regions to the overall flow stress are obtained by multiplying the stresses by the respective area fractions of each region. The sum of the two contributions gives the following relationship between flow stress and grain size:

$$\sigma(\epsilon) = \sigma_o + \left( 1 - \frac{\lambda_s}{\ell} \right) \frac{K_1}{\lambda_s} + \frac{\lambda_s}{\ell} \left( \frac{K_2}{\ell^{1/2}} \right) \quad (2.18)$$

where  $K_1$  and  $K_2$  are experimental constants.

In the range of small strains  $\lambda_s$  is of the order of grain size and thus, equation (2.18) reduces to the Hall-Petch equation with

$$K(\epsilon) \simeq \frac{\lambda_s K_2}{\ell} \quad (2.19)$$

The density of statistically stored dislocations increases with strain. As a result, the slip distance  $\lambda_s$  and thereby  $K(\epsilon)$  decreases with increasing strain. Ashby's model (equation 2.17) on the other hand, predicts a continuous increase in  $K(\epsilon)$  with strain. At large strains, the statistical term dominates leading to a  $\epsilon^{-1}$  dependence of the flow stress. At intermediate strains, both the geometrically necessary and the statistically stored dislocations govern the flow stress. This leads to a complex relationship between flow stress and grain size.

In view of the above discussion, it is clear that the proposed models are based on different assumptions and therefore they predict different variations of the Hall-Petch parameters with strain. For example, the models do not uniquely predict the strain dependence of  $K(\epsilon)$  with strain. The parameter  $K(\epsilon)$  may increase with strain (equations 2.16 and 2.17) or may decrease with strain (equation 2.19). Equation (2.11) based on the pile-up model does not explicitly describe the variation of  $K(\epsilon)$  (which is dependent on the variation of the critical stress to generate dislocations as a function of strain).

It may be pointed out that since the work-hardening models have been developed from a purely geometric consideration, it is difficult to attach physical significance to the parameters involved in the derived

equations. For example, equation (2.19) which relates  $K(\epsilon)$  to the slip distance of statistically stored dislocations in the small strain regime, does not permit one to interpret  $K(\epsilon)$  in terms of operative mechanisms during the early stages of deformation. Even though equation (2.18) has been applied successfully to explain the deformation behavior of aluminum, copper and brass (Thompson et al 1973, and Thompson and Baskes 1973), it has limited utility in developing an understanding of the physics of deformation. Another limitation of equations (2.18) and (2.19) is that they have several adjustable parameters ( $\sigma_o$ ,  $K_1$ ,  $K_2$  and  $\lambda_s$ ) and therefore one can expect a good fit on experimental data obtained from a wide range of metals and alloys. Thus, a good fit does not necessarily imply the validity of the model. A better method of verification would be to test the validity of the assumptions made in the model. Unfortunately, this is not an easy task, since it is difficult to distinguish the two dislocation densities: geometrically necessary and statistically stored dislocations. This is particularly true in the case of high stacking fault energy (SFE) materials. TEM observations (Thomas 1963, Hansen and Bay 1982, Hansen and Ralph 1982) show that it is difficult to obtain a quantitative description of the composite structure (hard mantle zone and a soft grain interior) as demanded by the model. Thus, the work-hardening models in their present form

are not particularly suited for gaining an understanding on the processes which govern the overall deformation behavior of polycrystals. In low SFE materials (e.g.,  $\alpha$ -brasses and austenitic stainless steels), the dislocations are confined in their slip planes leading to the formation of dislocation pile-ups at grain boundaries (Thomas 1963, Meakin and Petch 1974). Figure (2.4) shows the existence of dislocation pile-ups and other microstructural features (e.g., emission profiles and EGBDs) in a deformed 316L austenitic stainless steel. Therefore, the dislocation pile-up model may be the best approximation to explain the deformation of low SFE materials.

However, all models, including the dislocation pile-up model, neglect the influence of the grain boundary structure on the flow stress. It was shown in section 2.2 (figure 2.9) that grain boundary structure has a significant influence on the mechanical properties of polycrystals. However, no attempt was made to explain the dependence of the mechanical properties on the grain boundary structure. Therefore, the next section examines the influence of the grain boundary structure on the deformation behavior from a mechanistic point of view.

### 2.3.2. THE EFFECT OF GRAIN BOUNDARY STRUCTURE

It is generally recognized that grain boundaries are sources of lattice dislocations (Li 1963, Singh and Tangri 1970, Murr 1974 and 1975, and Malis and Tangri 1979) during plastic deformation of polycrystalline materials. The structure of grain boundaries can affect the conditions for dislocation emission from grain boundaries, which in turn would have an effect on the deformation behavior of polycrystals. However, there are only a limited number of investigations (Murr 1974, 1975 and 1981, Gleiter 1977, Grabski 1982, Varin, Kurzydowski and Tangri 1987) which relate the structure of grain boundaries to the generation of dislocations at and in the vicinity of grain boundaries. In-situ TEM observations (Murr 1974 and 1975) show that grain boundary ledges are a common source of lattice dislocations. These ledges which can be described by an array of single or agglomerated extrinsic grain boundary dislocations (EGBDs), have been shown to be a principal source of dislocations in the early stages of plastic deformation. The number of sources increase with increasing plastic deformation which leads to a larger number of emission profiles in the TEM image. If the EGBDs are the principal sources of dislocations as the above mentioned observations suggest, then the increase in the density of grain boundary dislocations with

strain would significantly affect the process of emission of dislocations at grain boundaries.

The idea that an EGBD can be a potential site for the generation of dislocations at grain boundaries has been further developed in a theoretical model proposed by Varin, Kurzydowski and Tangri (1987). Their model proposes that an EGBD produces a stress concentration site which facilitates the generation of lattice dislocations in the vicinity of the EGBD. In other words, the presence of an EGBD reduces the stress required to generate dislocations. The authors found that in the presence of EGBDs with localized cores, the stress required to generate dislocations becomes very small. As the core width of an EGBD increases (e.g., by annealing) the stress concentration decreases and therefore the required stress to generate dislocations increases. Table (2.2) shows the calculated values of the stress required to generate dislocations as a function of the core width of an EGBD. However, an external stress can constrict the core of an EGBD with a wide core (Gleiter 1977, and Grabski 1982). Such a mechanism can be envisaged by assuming a spread out EGBD to be described by partial dislocations with very small Burgers vectors (see section 2.2). Then the applied stress can push the partial dislocations together leading to the localization of a delocalized core of an EGBD. But as yet there is no satisfactory model which can describe the localization

TABLE 2.2

The calculated values of the stress required to generate dislocations at a pre-existing extrinsic grain boundary dislocation as a function of various core widths of the extrinsic grain boundary dislocation (Varin, Kurzydowski and Tangri 1987).

Core width of an EGBD (m)	Stress ( $\tau$ ) required to generate dislocations
$1 \times 10^{-9}$	Very small
$2 \times 10^{-9}$	Very small
$3 \times 10^{-9}$	G/255
$3.5 \times 10^{-9}$	G/120
$4 \times 10^{-9}$	G/90
$5 \times 10^{-9}$	G/63
$\tau = \frac{G}{30} - \frac{0.77Gb}{\pi(1-\nu)} \frac{1}{S}$ <p>where S is the EGBD core width</p>	



phenomenon. Also, such a mechanism is expected to operate only if the temperature of deformation is low. At high temperatures there will always be a tendency for the dislocation to spread its core and thus it will not be an effective stress concentrator.

Since EGBDs are not a part of the equilibrium structure of the grain boundary, their presence results in uncanceled long range elastic stress field (e.g., Gleiter 1977). It is expected that the long range stresses will contribute to the work-hardening of polycrystals. Therefore, the existence of these stresses cannot be neglected in any detailed study on the influence of the grain boundary structure on the deformation characteristics. In spite of this fact, it has merited little discussion in literature.

The above discussed grain boundary structural effects can be isolated by examining their impact on the experimentally observed variation of the Hall-Petch parameters  $\sigma_0(\epsilon)$  and  $K(\epsilon)$  in equation (2.10). In light of the experimental observations available in literature, some of the proposed ideas are briefly discussed below. The exact nature of the role played by the grain boundary structure and its implications on the Hall-Petch analysis is discussed in detail in chapter 4.

Figure (2.13) shows the variation of the Hall-Petch parameters  $\sigma_0(\epsilon)$  and  $K(\epsilon)$  for polycrystalline aluminum

deformed at room temperature. From the figure, it can be seen that  $K(\epsilon)$  initially increases and goes through a peak and then continuously decreases with strain. The initial increase in  $K(\epsilon)$  has been associated with grain boundary strengthening and/or increased difficulty in the operation of grain boundary dislocation sources. The decrease in  $K(\epsilon)$  observed beyond a certain strain has been associated with the formation of dislocation cells and sub-grains as a result of recovery processes (e.g., cross-slip which occurs rather easily in high SFE materials like aluminum). The reason for this decrease is that the recovery processes occur at a higher rate in the fine grained materials as compared with the coarse grained materials (Lloyd 1980). This leads to a much faster decrease in the work-hardening rate of the fine grained material beyond a certain strain which in turn results in the observed decrease in  $K(\epsilon)$ . Thus, the physical interpretation of  $K(\epsilon)$  in the higher strain regime becomes questionable since the specimens of different grain sizes may have widely different dislocation structures. TEM observations (Lloyd 1980) made on aluminum confirm that the coarse grained material at large strains shows a well defined cell structure in the entire grain area. While the fine grained material shows large density of dislocations in the vicinity of grain boundaries and few dislocations in the grain interior. Also, the formation of cells or sub-grains

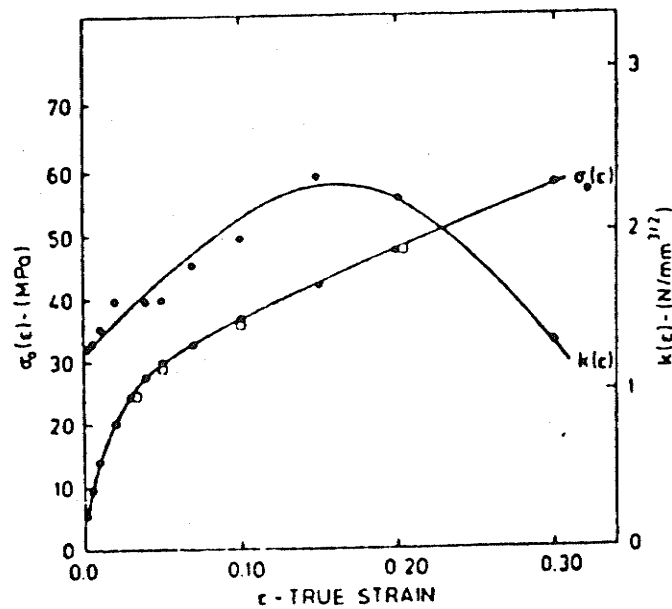


**Figure 2.13:** The variation of the Hall-Petch parameters  $\sigma_0(\epsilon)$  and  $K(\epsilon)$  as a function of strain in polycrystalline aluminum deformed at room temperature (Fujita and Tabata 1973).

implies that the initial value of the grain size can no longer be used in the Hall-Petch relationship (equation 2.10).

Figure (2.14) shows the plot of  $K(\epsilon)$  as a function of strain in 70:30 brass deformed at room temperature.  $K(\epsilon)$  shows a small increase and then becomes more or less constant. On further straining  $K(\epsilon)$  is observed to drop. Thus, the trend of the variation of  $K(\epsilon)$  is similar to that observed in the polycrystalline aluminum (see figure 2.13). However, such a variation in  $K(\epsilon)$  cannot be explained as a result of recovery processes, since no significant recovery is expected in  $\alpha$  - brass which is a low SFE material. Meakin and Petch (1974) suggested that this decrease may be due to the unlocking of dislocation sources at the head of dislocation pile-ups. This is presumably because with plastic deformation, the density of dislocations in the individual pile-ups and the density of pile-ups themselves increase with strain leading to a higher stress concentrations at and in the vicinity of grain boundaries. The high stresses produced, leads to a decrease in the stress required to generate dislocations and/or unlock previously locked dislocation sources in the vicinity of pile-ups. Another possible mechanism which may be proposed here is that the dislocations are preferentially emitted in the vicinity of EGBDs. As discussed earlier in this section, EGBDs being powerful

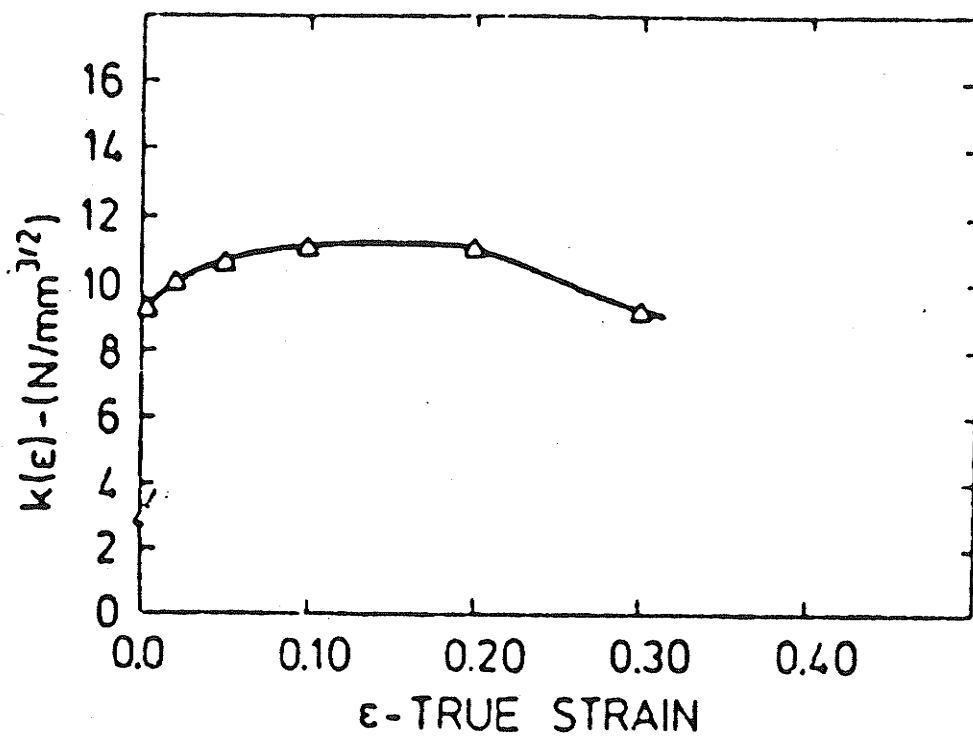


**Figure 2.14:** The variation of  $K(\epsilon)$  as a function of strain in 70:30 brass deformed at room temperature (Meakin and Petch 1974).

stress concentrators, can lead to a decrease in the stress required to generate dislocations at grain boundaries. Such a mechanism can also be expected to operate in the case of high SFE materials where also EGBDs are formed during plastic deformation. But, in these materials, the recovery mechanisms which are initiated at small strains, may dominate the plastic deformation process.

Referring to figure (2.13) again, it may be seen that  $\sigma_o(\epsilon)$  varies parabolically with strain for aluminum deformed at room temperature. In contrast for low SFE  $\alpha$ -brass polycrystals (produced by a high Zn content)  $\sigma_o(\epsilon) - \epsilon$  curve is linear (Meakin and Petch 1974) up to large strains. In the case of relatively high SFE  $\alpha$ -brass (produced by decreasing the Zn content)  $\sigma_o(\epsilon) - \epsilon$  curve is parabolic as shown in figure (2.15). The departure from linearity in the plots of  $\sigma_o(\epsilon)$  versus strain, as the Zn content in  $\alpha$  - brasses is decreased, i.e., as the SFE increases can be clearly observed in figure (2.15). Meakin and Petch concluded, that this departure from linearity occurs due to the onset of recovery at small strains in high SFE materials.

$\sigma_o(\epsilon)$  which is the friction stress in the grain interior has been associated with mono-crystal hardening characteristics (see equations 2.12 - 2.14). The linear variation of  $\sigma_o(\epsilon)$  with strain is associated with stage II type of hardening in mono-crystals (Hirsch 1975) which is

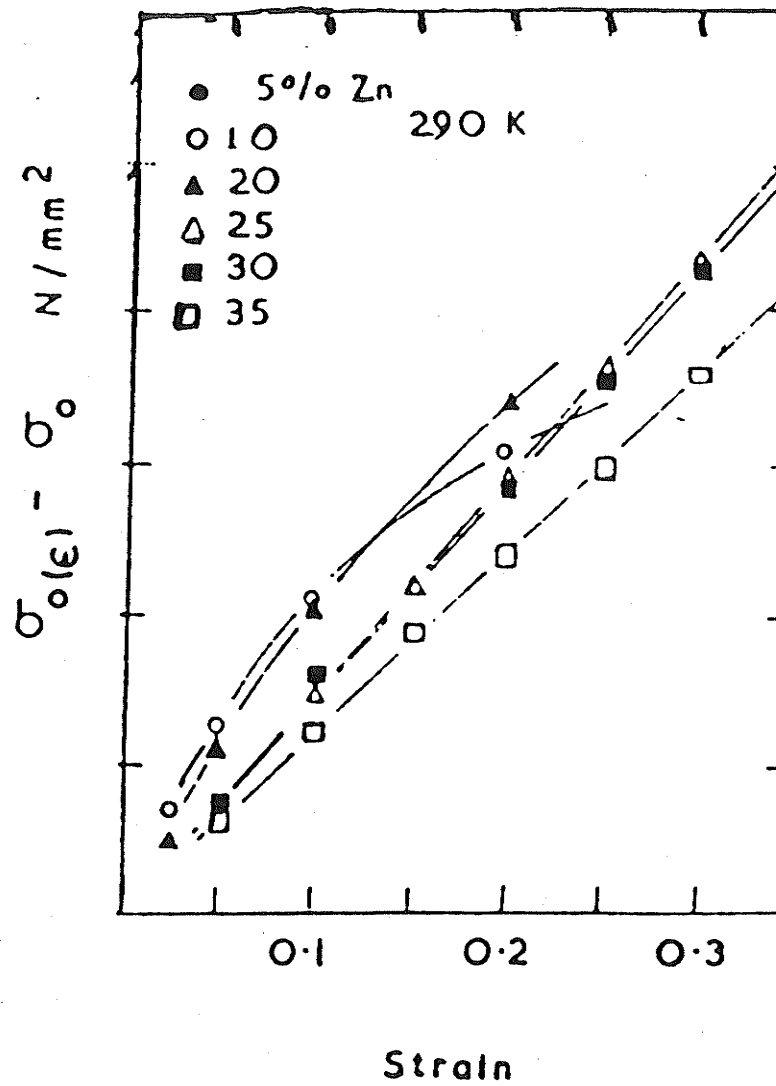


**Figure 2.15:** Plots of  $\sigma_0(\epsilon) - \sigma_0(\epsilon = 0)$  as a function of strain in the room temperature deformation of  $\alpha$  - brasses of varying Zn content (Meakin and Petch 1974).

characterized by dislocation accumulation by multiple slip with no evidence of cross-slip. The parabolic  $\sigma_o(\epsilon) - \epsilon$  curve is associated with stage III type of hardening in mono-crystals which is characterized by recovery processes.

Armstrong (1983), compared the experimental slope of  $\sigma_o(\epsilon) - \epsilon$  curve for 70:30 brass with the computed slope of stage II. Using equation (2.14), he found that the calculated value of  $76 \text{ N.mm}^{-2}$  is considerably lower (10 times lower) than the experimental value of  $760 \text{ N.m}^{-2}$ . The difference has been explained on the basis that in mono-crystals, dislocations can escape to the free surface, while in polycrystals the dislocations are trapped at grain boundaries forming EGBDs, pile-ups, etc. The presence of EGBDs would produce a long range stress field. This long range stress field would also contribute to the friction stress  $\sigma_o(\epsilon)$  in the grain interior. Since the density of EGBDs increases with plastic deformation, this contribution would increase with strain leading to higher work-hardening rates in the grain interior. In chapter 4 the effect of the presence of EGBDs on the variation of the Hall-Petch parameters and thereby the overall deformation behavior of polycrystals is discussed in detail.



## CHAPTER 3

### EXPERIMENTAL PROCEDURE

The experiments were performed on a commercial 316L stainless steel. The nominal composition of the steel is given in Table 3.1. The as-received material was in the form of a plate of thickness 15mm. The techniques used in the thermo-mechanical treatments, mechanical tests, transmission electron microscopy observations and quantitative metallography measurements are discussed in the following sections.

#### 3.1. THERMO-MECHANICAL TREATMENTS

The as-received plate of 316L stainless steel was cold rolled to 92% and then recrystallized for 1 hour over a temperature range of 900°C to 1000°C. This resulted in a range of grain sizes (defined as the mean intercept length  $\ell$ , see section 3.4) varying from 3.4  $\mu\text{m}$  to 22.4  $\mu\text{m}$ . Table 3.2 shows the individual values of the grain size produced at different annealing temperatures. Table 3.2 also lists the ratio ( $\text{SD}/\ell$ ) of the standard deviation (SD) to the mean grain size ( $\ell$ ) measured over 50 fields (each field contained approximately 100 grains) for each specimen. It can be seen

TABLE 3.1

The nominal composition of commercial 316L stainless steel  
(Boyer and Gall 1985).

	C	Cr	Ni	Mo	Mn	Si	P	S	Fe
%	0.03	16	10	2	2	1	0.045	0.03	balance

TABLE 3.2

Grain size ( $\ell$ ) measurements in specimens of 316L stainless  
steel annealed at different temperatures for a constant  
annealing time of 1 hour.

T (°C)	$\ell$ ( $\mu\text{m}$ )	SD/ $\ell$
900	3.4	0.090
930	5.6	0.097
955	8.9	0.080
970	11.2	0.084
985	18.0	0.081
990	21.0	0.077
1000	22.4	0.073

that the ratio ( $SD/\ell$ ) is approximately same for the range of grain sizes examined. This implies that the spatial variation of grain size (i.e., field to field variation) obtained as a result of the above thermo-mechanical treatments was similar in all specimens. It may be noted that the annealing temperatures greater than or equal to  $900^{\circ}\text{C}$  lead to an equiaxed grain structure. The grain boundaries at these annealing temperatures are expected to be in their equilibrated state (Varin and Tangri 1982). Hereafter, these specimens will be referred to as the *as-annealed specimens*.

Some of the annealed specimens were pre-strained to 2% in tension and subsequently annealed at temperatures in the range of  $550^{\circ}\text{C}$  to  $1000^{\circ}\text{C}$  for annealing times varying from 1 to 30 minutes. The short annealing times (less than or equal to 5 minutes) were obtained in a multi-zone furnace where the heating up time was minimised to approximately 15 seconds. Figure (3.1a) shows a schematic diagram of the multi-zone furnace used for the heat treatment. Figure (3.1b) shows the temperature profile along the length of the furnace. The temperature profile shows that there are three constant temperature zones in the furnace: zone A (kept at approximately room temperature), zone C (kept at the required annealing temperature  $T$ ), and zone B (kept at a temperature  $T'$ , approximately  $200^{\circ}\text{C}$  higher than that in zone C). The specimen to be annealed is initially kept at room temperature

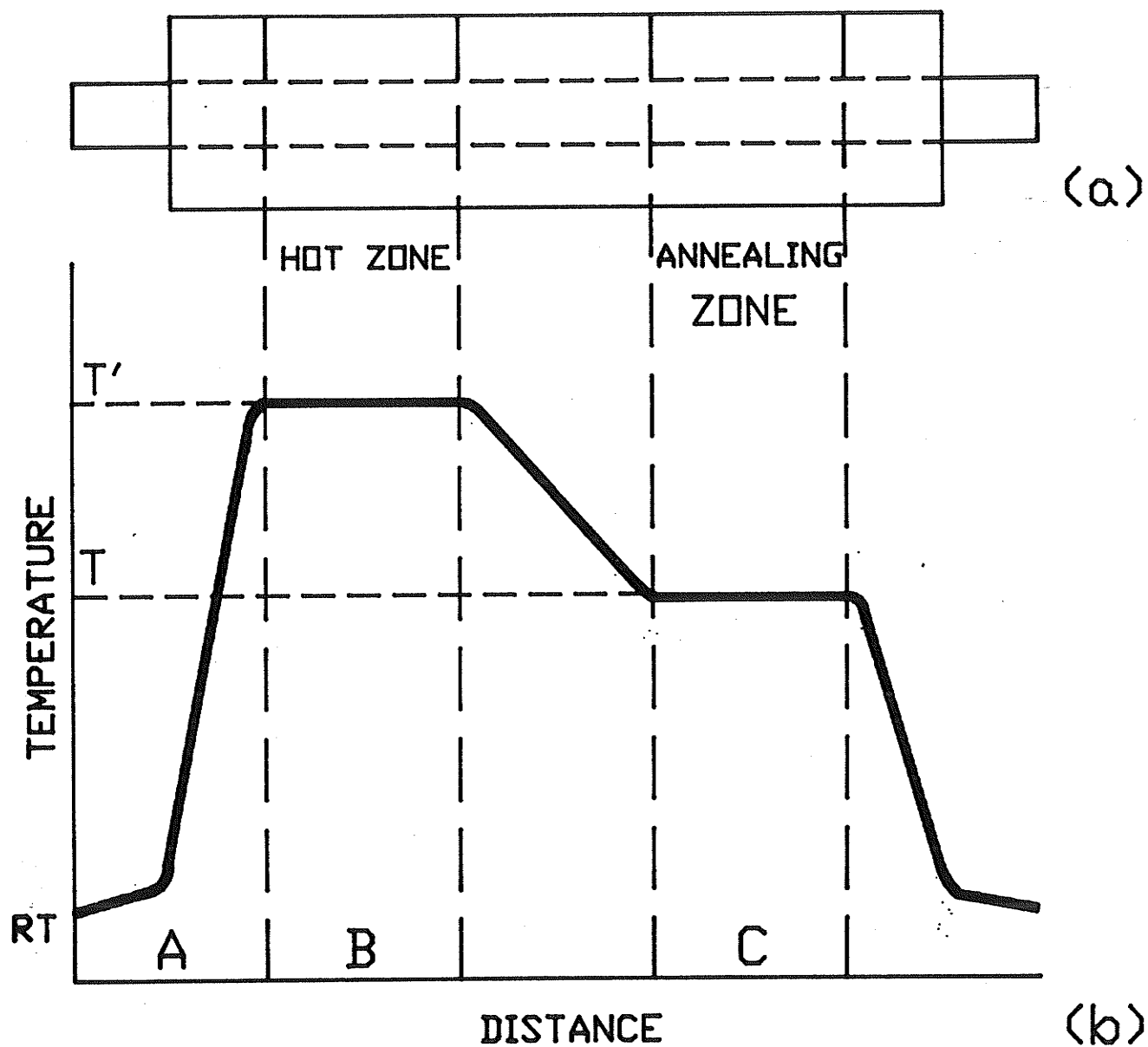


**Figure 3.1:** (a) A schematic sketch of the multi-zone furnace and (b) the temperature profile along the length of the furnace.

in zone A. A thermocouple, directly attached to the specimen is used to continuously monitor the specimen temperature. The specimen is pulled into the hot zone B for rapid heating of the specimen. When the specimen temperature reaches to a value  $50^{\circ}\text{C}$  lower than the annealing temperature  $T$ , it is pulled in zone C and annealed for the appropriate annealing time followed by water quenching. Figure (3.2) shows a typical temperature versus time curve for a specimen which was annealed at  $800^{\circ}\text{C}$ . It can be seen from the figure that it takes only 15 seconds for the specimen to reach the desired annealing temperature.

### 3.2. TENSILE TESTS

The strips of the rolled material were machined using an Induma N/C milling machine to prepare standard plate type tensile specimens. The specimens had a cross-section area of approximately  $1.2 \times 6.6 \text{ mm}^2$  and a gauge length of 25.4 mm. Thickness of 1.2 mm ensures that the ratio of thickness to grain size is at least 50 grains for all the grain sizes considered (see Table 3.2). Thus, the deformation behavior of these specimens would reflect that for *true polycrystals* (Miyazaki et al 1979). The tension tests were performed at room temperature on an Instron universal testing machine on-line with a PDP-11 system for data acquisition. The

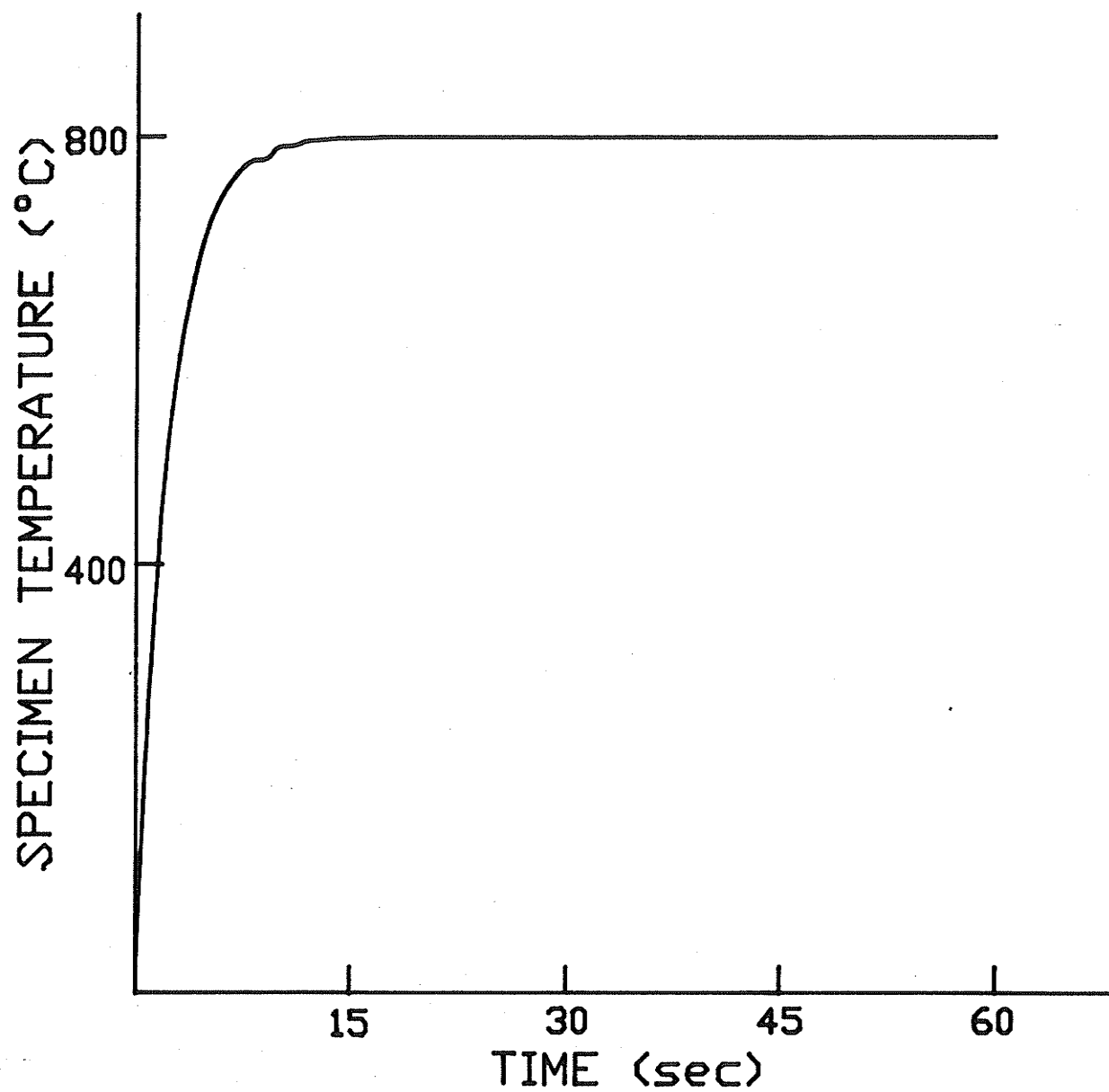


Figure 3.2: A typical curve for the specimen temperature versus time for an annealing temperature of 800°C.

applied strain rate for the tests was  $10^{-4} \text{ s}^{-1}$ .

### 3.3. TRANSMISSION ELECTRON MICROSCOPY

Thin foils for transmission electron microscopy (TEM) were prepared by chemical thinning of tensile specimens using a heated solution of 50% HCl, 10%  $\text{HNO}_3$ , 5%  $\text{H}_3\text{PO}_4$ , and 35%  $\text{H}_2\text{O}$  (Hirsch, Howie, Nicholson, Pashley and Whelan 1977). Disks of 3 mm diameter were made with Agemaspark spark cutting machine. Final thinning was completed using a Struers Tenupol-2 twin jet electropolishing unit operating at 14.5 V and 70 mA using a 15% perchloric acid: methanol electrolyte at  $-40^\circ\text{C}$ . The foils thus prepared were examined with a JEOL 2000 FX scanning transmission electron microscope operating at an accelerating potential of 200 KV.

### 3.4. QUANTITATIVE METALLOGRAPHY

Metallographic measurements were performed on observations made on the surface of the tensile specimens using light microscopy. The surface layer of the specimens was removed by chemical thinning (the chemical solution was the same as that used for TEM foil preparation, section 3.3)

followed by mechanical polishing<sup>\*</sup>. The grain boundaries were revealed by electrochemical etching (Stephenson 1979): electrolyte: 60% HNO<sub>3</sub>; electrode: platinum; current density: 0.66 mA/mm<sup>2</sup>. This etching procedure ensures that the twin boundaries are not revealed. Another advantage of such an etching technique is that it preferentially etches the grain boundaries resulting in a sharp black and white contrast, as shown in the optical micrograph of figure (3.3). Such a contrast is ideal for metallographic measurements on automatic image analysis systems.

The following metallographic measurements were performed:

- 1) intercept length,  $\ell$ ,
- 2) grain boundary length,  $L$ ,
- 3) dihedral angles,  $\phi$ , and
- 4) grain boundary curvature.

To perform the above measurements, special computer programs were developed for a Leitz TAS PLUS image analysis system. For intercept length measurements, the program generates an image of a grid of parallel lines, in three different orientations 120° apart superimposed on the image of grain boundaries. The programs measure the grain boundary length as the distance between two triple points, and the

---

<sup>\*</sup>Chemical thinning followed by mechanical polishing results in the removal of 10 to 30 grains thick surface layer.



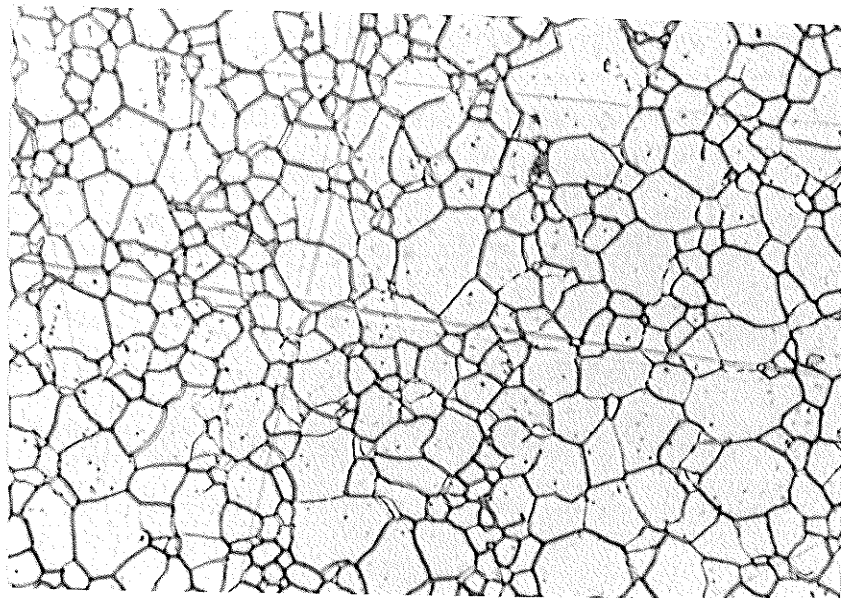
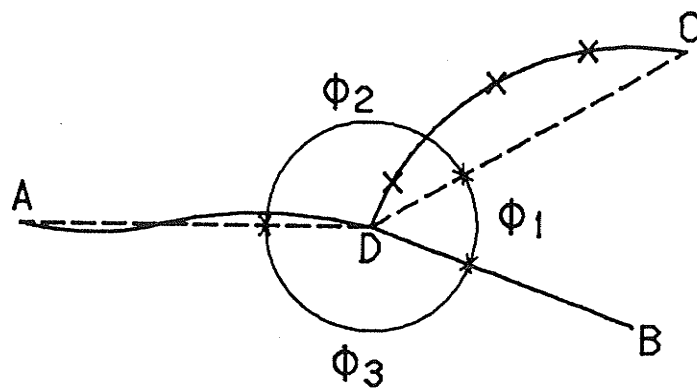


Figure 3.3: An optical micrograph of an annealed specimen of 316L stainless steel.

dihedral angles as the angles between straight lines joining adjacent triple points. For curvature measurements, the coordinates of individual points on a grain boundary are determined. Figure (3.4) schematically illustrates the procedure of the above measurements. The programs developed for these measurements are discussed in greater detail in appendix A with an emphasis on the possible sources of errors and the methods used to minimise them.



**Figure 3.4:** A schematic of the measurement procedure for grain boundary length ( $L$ ), dihedral angles ( $\phi$ ) and the grain boundary curvature.

## CHAPTER 4

### RESULTS AND DISCUSSION

In this chapter the effect of the changes in the grain boundary structure (e.g., changes in the density of EGBDs) as a result of pre-strain and annealing on the mechanical properties of polycrystals of 316L stainless steel of varying grain size has been examined. As discussed in section (2.2), the spreading of EGBDs on annealing does not lead to the recovery of the non-equilibrium grain boundary structure. There is no satisfactory model to date which can describe the annihilation of EGBDs as a result of annealing at high temperatures. Therefore, a theoretical model has been developed to obtain a quantitative description of the kinetics of the transformation of non-equilibrium grain boundaries to equilibrium grain boundaries. A detailed study has also been carried out to obtain a relationship between the Hall-Petch parameters  $\sigma_0(\epsilon)$  and  $K(\epsilon)$  in equation (2.10) and the structure of grain boundaries.

#### 4.1. THE RELATIONSHIP BETWEEN CHANGES IN GRAIN BOUNDARY STRUCTURE AND PROPERTIES OF POLYCRYSTALS

The changes in the grain boundary structure produced as a result of 2% pre-strain and subsequent annealing are

described in terms of the changes in the density of dislocations at and in the vicinity of grain boundaries and the changes in the geometry of the grain boundary network. The changes in the geometry of the grain boundary network were measured on the surface of the specimens in terms of the changes in the grain boundary length ( $L$ ), dihedral angles ( $\phi$ ), grain boundary curvature, and intercept length ( $\ell$ ). The measurement techniques of the above metallographic parameters are discussed in section 3.4 (see also figure 3.4). These changes have then been correlated with the mechanical properties of polycrystals of 316L stainless steel.

#### 4.1.1. EXPERIMENTAL RESULTS

The experiments were done on 316L stainless steel specimens of two grain sizes: 3.4  $\mu\text{m}$  (fine grain size) and 18.0  $\mu\text{m}$  (coarse grain size) produced by annealing of cold rolled material (refer to section 3.1 and Table 3.2).

Metallographic measurements were performed on the specimens of the fine grained material (grain size: 3.4  $\mu\text{m}$ ) with the thermo-mechanical histories shown in Table (4.1).

Specimens employed for metallographic measurements were also used for transmission electron microscopy (TEM) studies.

TABLE 4.1

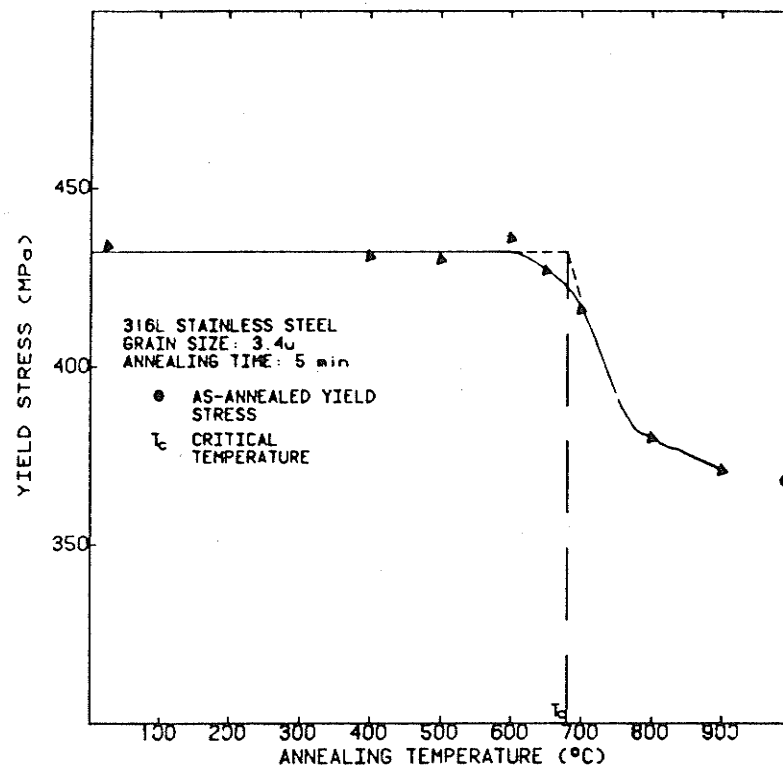
Thermo-mechanical histories of the 316L stainless steel specimens.

- A. As-annealed, annealed at  $900^{\circ}\text{C}$  for 1 hour.
- B. As under A and then pre-strained to 2%.
- C. As under B and then annealed at  $600^{\circ}\text{C}$  for 5 minutes.
- D. As under B and then annealed at  $800^{\circ}\text{C}$  for 5 minutes.

#### 4.1.1.1. TENSION TEST RESULTS

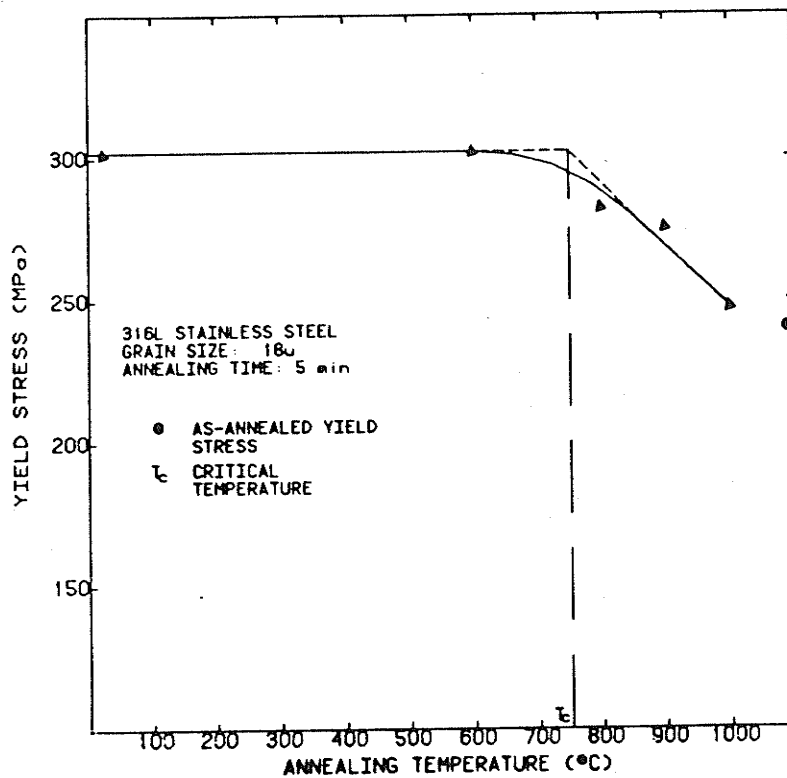
The results of the measurements of the yield stress (0.2% offset) on the material of both grain sizes (3.4  $\mu\text{m}$  and 18.0  $\mu\text{m}$ ), pre-strained to 2% and subsequently annealed at various temperatures and annealing times are shown in figures (4.1) and (4.2). Figures (4.1a) and (4.1b) show the variation of yield stress as a function of annealing temperature at a constant annealing time of 5 minutes for the specimens of grain sizes 3.4  $\mu\text{m}$  and 18.0  $\mu\text{m}$  respectively. Figures (4.2a) and (4.2b) show the variation of yield stress as a function of annealing time at constant annealing temperatures of 800°C and 750°C respectively for the fine grained specimens.

From figures (4.1a) and (4.1b), it can be seen that there exists a critical temperature  $T_c$ , at a given constant annealing time, beyond which the yield stress is observed to drop. The values of  $T_c$  (the method for estimating  $T_c$  is shown in the figures) , listed in Table (4.2) are 680°C and 750°C for the specimens with grain sizes of 3.4  $\mu\text{m}$  and 18.0  $\mu\text{m}$  respectively. It may be noted that the critical temperature  $T_c$  is larger than the spreading temperature  $T_d$  at which the image contrast of EGBDs as observed in TEM disappears after 30 seconds. For this type of steel  $T_d$  has been estimated to be approximately 500°C for random grain boundaries (Varin and Tangri 1982, and Kurzydowski et al 1985). The implication of



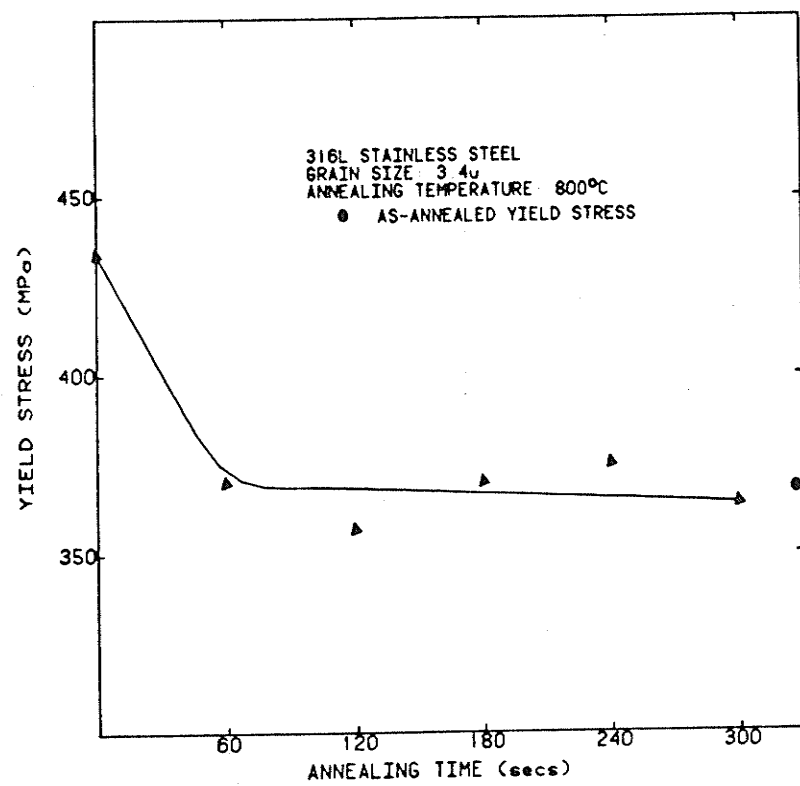
(a)



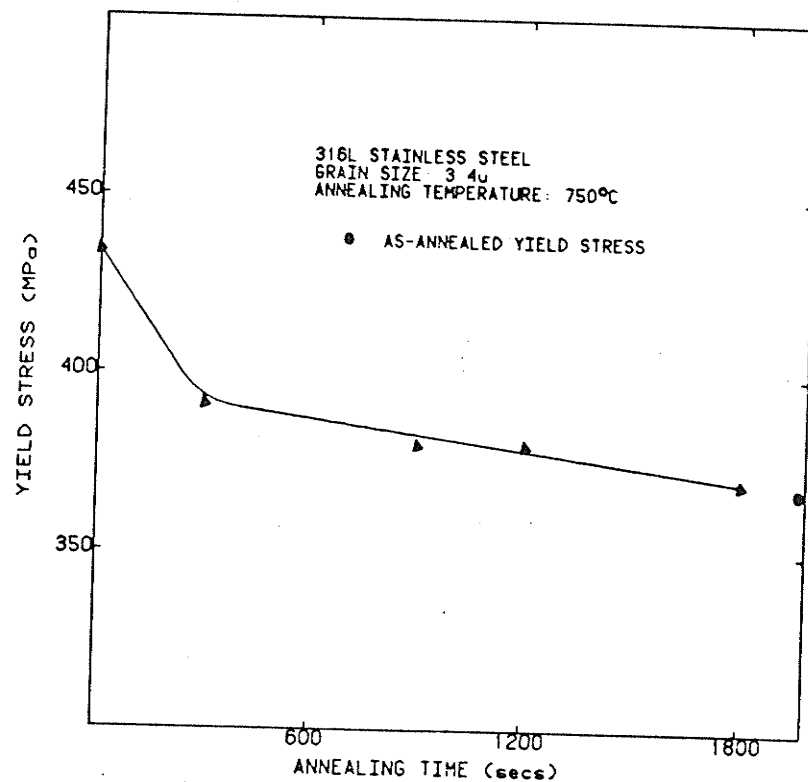


(b)

**Figure 4.1:** Variation of yield stress as a function of annealing temperature for a constant annealing time of 5 minutes after 2% pre-strain in 316L stainless steel specimens of grain sizes (a) 3.4  $\mu\text{m}$  and (b) 18.0  $\mu\text{m}$ .



(a)



(b)

**Figure 4.2:** Variation of yield stress in 2% pre-strained 316L stainless steel specimens of grain size 3.4  $\mu$ m as a function of annealing time for constant annealing temperatures of (a) 800°C and (b) 750°C.

TABLE 4.2

Experimentally estimated values of the critical temperature  $T_c$  for fine and coarse grained 316L stainless steel.

Grain Size ( $\mu\text{m}$ )	Annealing Time (minutest)	Critical Temperature $T_c$ ( $^{\circ}\text{C}$ )
3.4	5	680
18.0	5	750
$T_c$ is defined as shown in figures (4.1a) and (4.1b)		

this observation, as also noted earlier, is that the fading of TEM contrast of the EGBDs does not coincide with the recovery of the yield stress or with the recovery of non-equilibrium grain boundaries.

The critical temperature  $T_c$  depends on the time of annealing and generally longer times result in lower values of  $T_c$ . On increasing the annealing temperature beyond  $T_c$ , the yield stress steadily decreases to a stable value similar to that observed in the as-annealed material. Figures (4.2a) and (4.2b) show that the yield stress continuously decreases with increasing annealing time for a given annealing temperature. Thus, it can be concluded that there is a combination of annealing temperature (denoted by  $T_r$ ) and annealing time (denoted by  $t_r$ ) at which the yield stress of the pre-strained specimens is completely recovered.

#### 4.1.1.2. METALLOGRAPHY MEASUREMENTS RESULTS

Results of the grain boundary length measurements are shown in the form of histograms in figure (4.3). Mean values and 95% confidence limits (Spiegel 1975) obtained from the distribution of the grain boundary lengths are plotted in figure (4.4a) and are also listed in Table (4.3). The results indicate that there is no significant difference in the values of the mean grain boundary length for specimens A, B

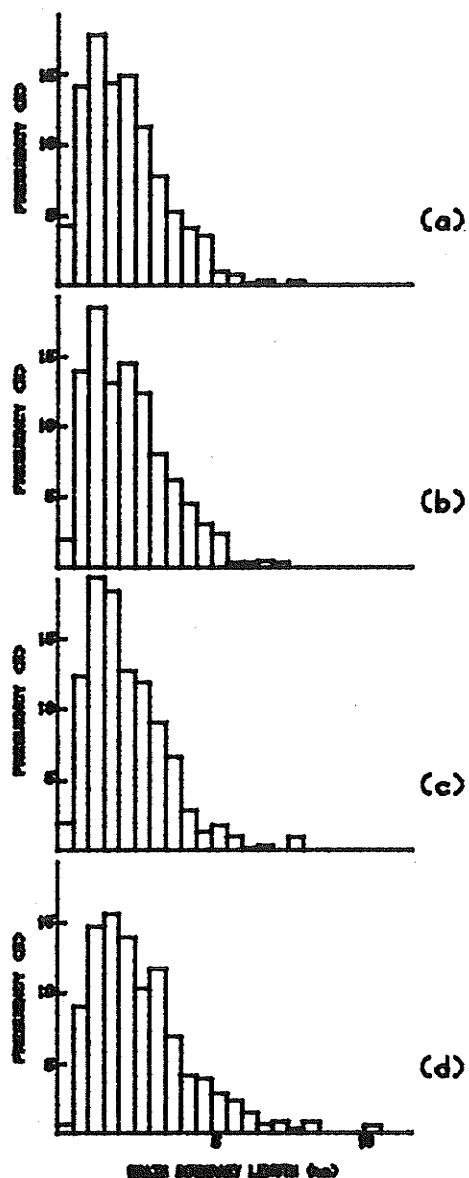


**Figure 4.3:** Distribution of grain boundary lengths for the (a) as-annealed, (b) 2% pre-strained specimens, and subsequently annealed at (c) 600°C and (d) 800°C for 5 minutes.

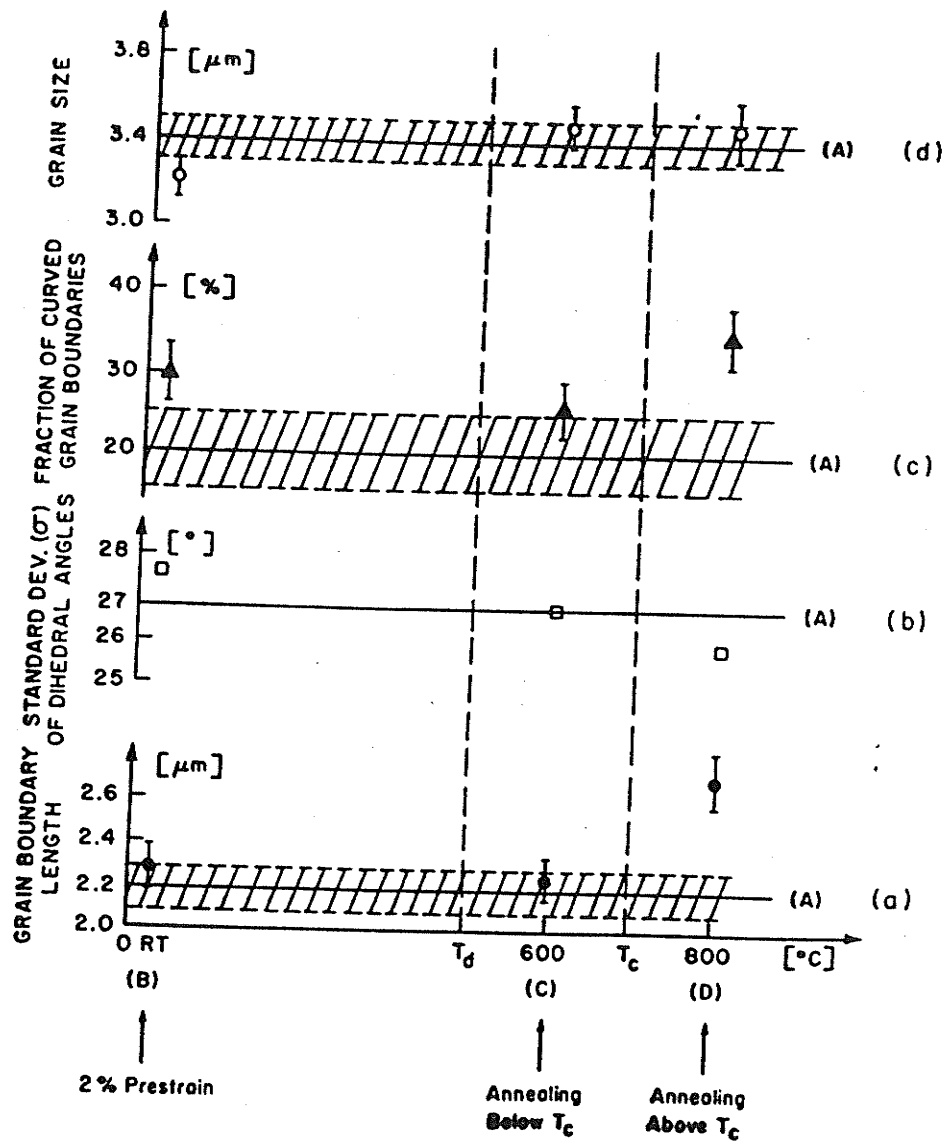


**Figure 4.4:** Variation in the (a) mean grain boundary length, (b) standard deviation of dihedral angles, (c) fraction of curved grain boundaries, and (d) mean intercept length as a function annealing temperature for a constant annealing time of 5 minutes in specimens of grain size 3.4 μm.

TABLE 4.3

The results of the measurements of grain boundary length, dihedral angles, curvature and mean intercept length for specimens A, B, C and D for the fine grained material.

	A	B	C	D
Mean grain boundary <sup>*</sup> length ( $\mu\text{m}$ )	2.18 $\pm$ 0.09	2.28 $\pm$ 0.09	2.23 $\pm$ 0.10	2.71 $\pm$ 0.13
Standard deviation of dihedral angles ( $^{\circ}$ ) <sup>*</sup>	26.76	27.60	26.80	25.89
Fraction of curved grain boundaries <sup>*</sup> (%)	21.6 $\pm$ 4.5	29.9 $\pm$ 3.4	26.8 $\pm$ 3.7	34.9 $\pm$ 3.7
Mean intercept <sup>**</sup> length ( $\mu\text{m}$ )	3.39 $\pm$ 0.10	3.23 $\pm$ 0.11	3.48 $\pm$ 0.11	3.47 $\pm$ 0.14
<sup>*</sup> number of measurements exceeded 500. <sup>**</sup> mean intercept length was calculated from 50 fields with an area of $73 \times 63 \mu\text{m}^2$ for each field. Total number of intercepts measured exceeded 3000.				



and C. However, the mean grain boundary length for specimen D (annealed at 800°C for 5 minutes) is significantly higher than those for specimens A, B and C. Also the scatter (i.e., the 95% confidence limit) of grain boundary lengths for specimen D is broader than the scatter for the other specimens.

The distributions of the dihedral angles for specimens A through D are shown as histograms in figure (4.5). The plot of the standard deviation of dihedral angles as a function of pre-strain and annealing temperature is shown in figure (4.4b). The values of the standard deviations are listed in Table 4.3 (the mean value of the dihedral angles being 120°). From figure (4.4b) the following deductions can be made:

- 1) 2% pre-strain results in a larger scatter of dihedral angles.
- 2) Subsequent annealing at 600°C and 800°C decreases the scatter of the dihedral angles (even though the difference in the standard deviation is small, it can be shown using the F-Test (Spiegel 1975) that due to the large number of measurements it is statistically significant). The standard deviation of the dihedral angles for specimen C (annealed at 600°C for 5 minutes) drops to the value obtained for specimen A (as-annealed). The standard deviation for specimen D (annealed at 800°C for 5 minutes) drops to a value

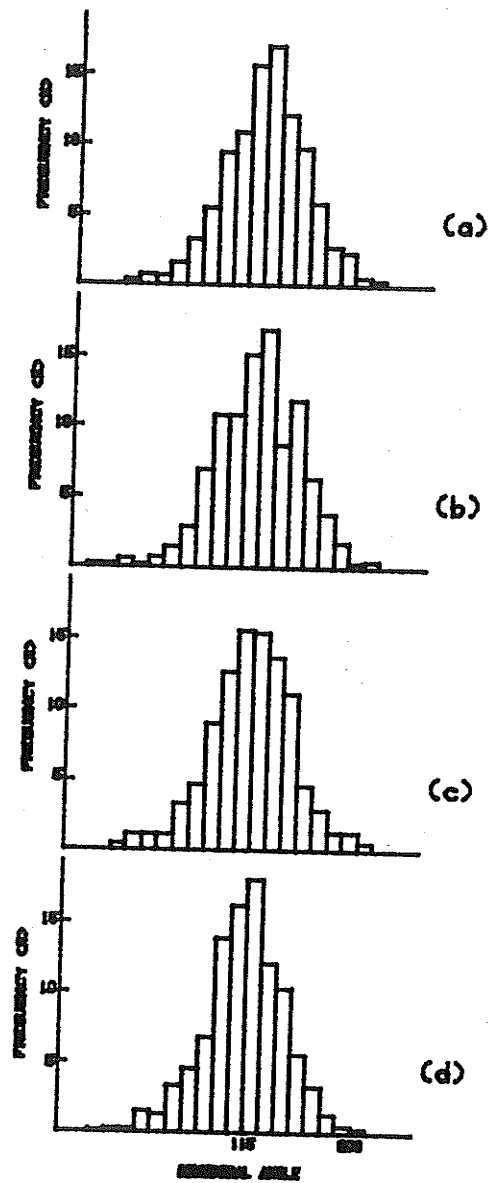


**Figure 4.5:** Distribution of dihedral angles for the (a) as-annealed, (b) 2% pre-strained specimens, and subsequently annealed at (c) 600°C and (d) 800°C for 5 minutes.

lower than that for specimen A.

The results of the analysis of grain boundary curvature are shown in Table (4.3) and are also plotted as a function of annealing temperature in figure (4.4c). The results indicate that there is a significant difference in the fraction of curved grain boundaries between specimens A (as-annealed) and D (annealed at 800°C for 5 minutes).

Mean intercept length was measured over 50 fields (approximately 200 grains per field) on specimens A through D. Figure (4.6) shows the histograms of the distribution of intercept lengths. Figure (4.4d) shows the plot of mean intercept length for specimens A through D. The mean values of the intercept length and the 95% confidence limit for each specimen are presented in Table (4.3). It can be seen that the mean intercept length slightly decreases after 2% pre-strain and is slightly higher than the initial value after annealing at 600°C. On annealing beyond 600°C, the value of the mean intercept length remains unchanged.

#### 4.1.1.3. TRANSMISSION ELECTRON MICROSCOPY OBSERVATIONS

Typical dislocation structures within the grain interior as well as at the grain boundaries of specimens A, B, C and D are shown in the TEM micrographs of figures (4.7), (4.8), (4.9) and (4.10) respectively. Figures (4.7a) and (4.7b) show

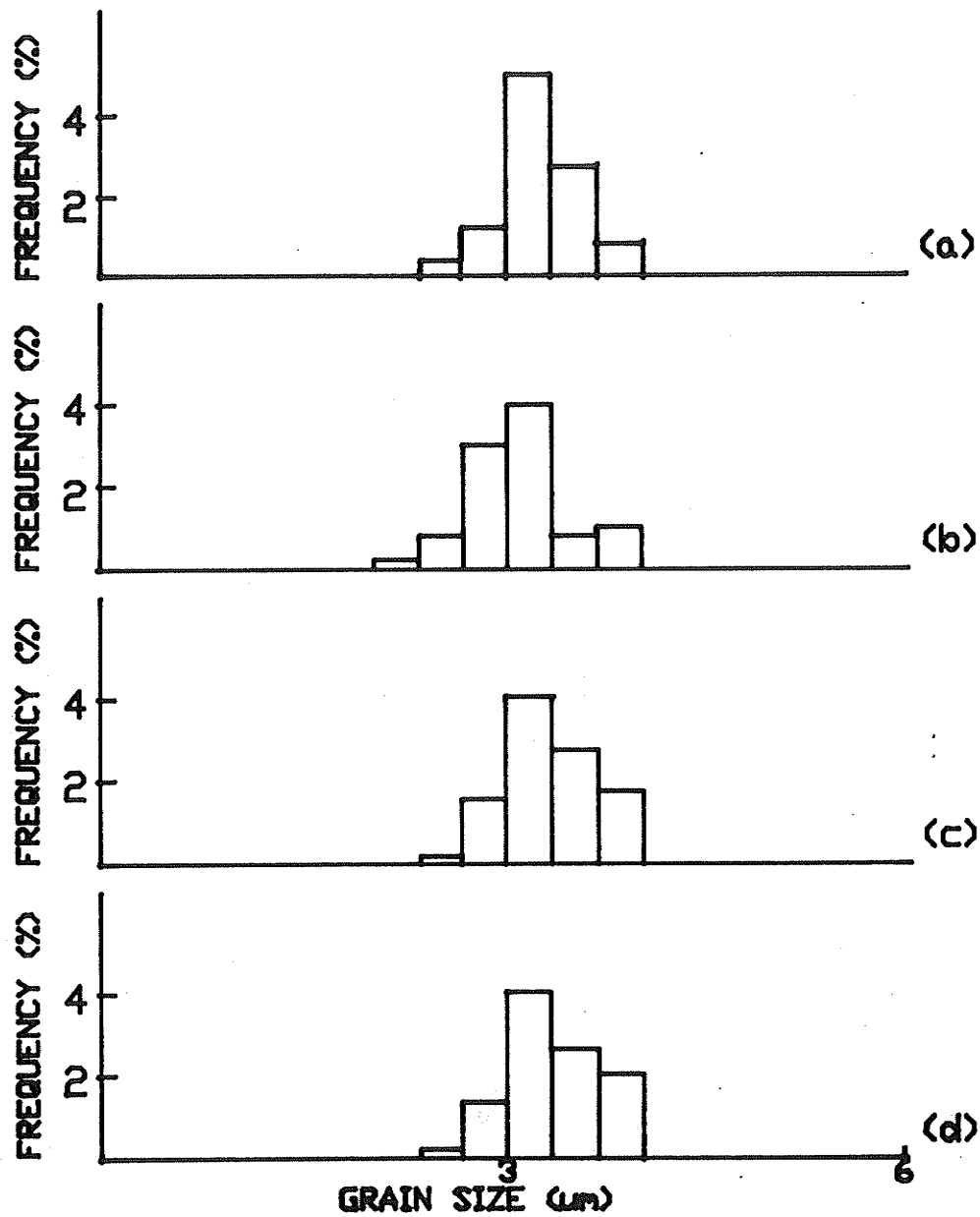
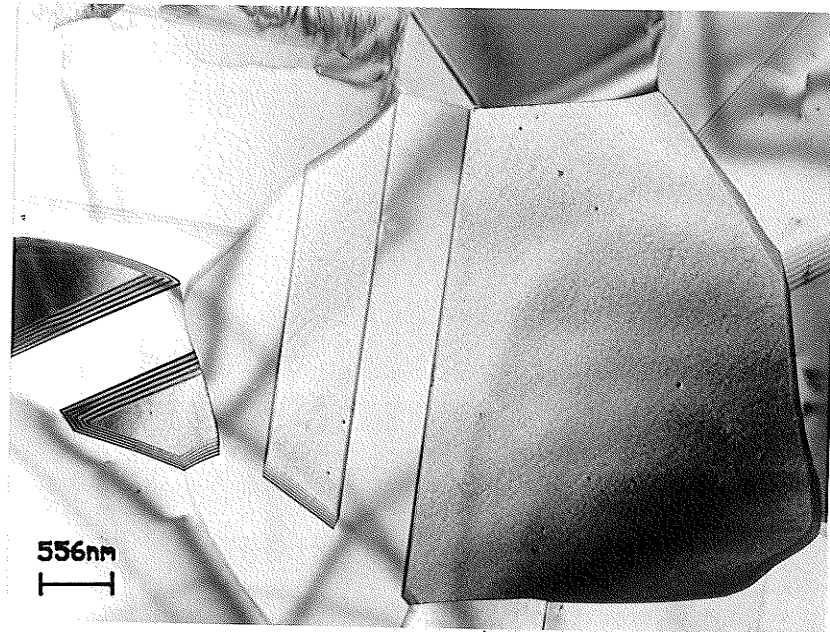
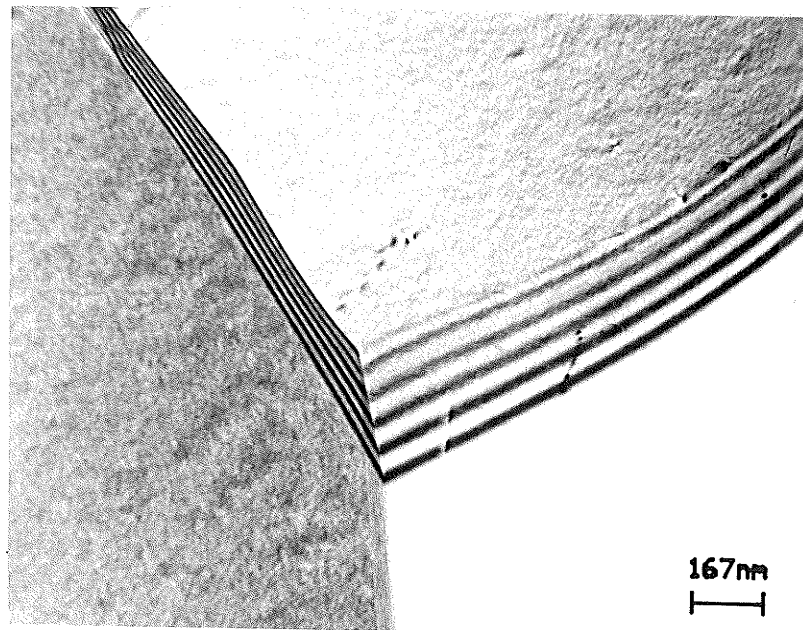


**Figure 4.6:** Distribution of intercept lengths for the (a) as-annealed, (b) 2% pre-strained specimens and subsequently annealed at (c) 600°C and (d) 800°C for 5 minutes.

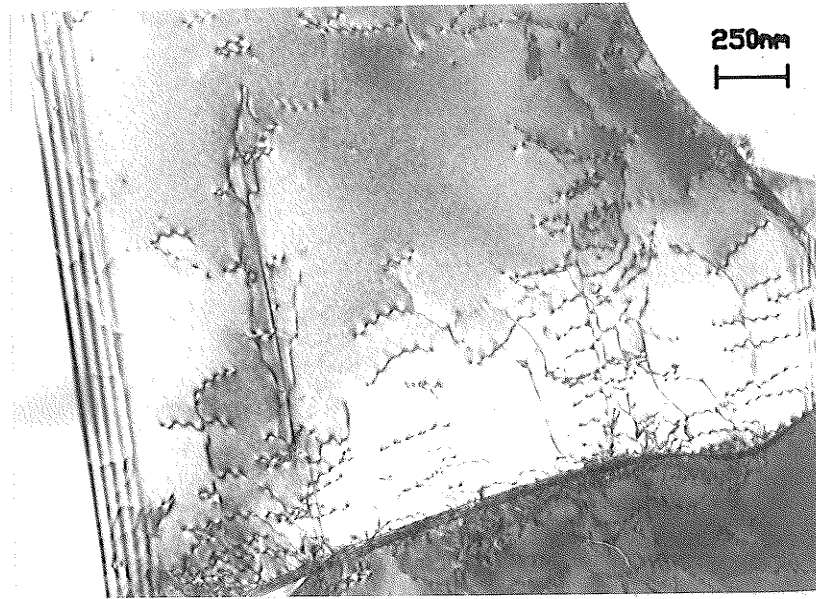


(a)

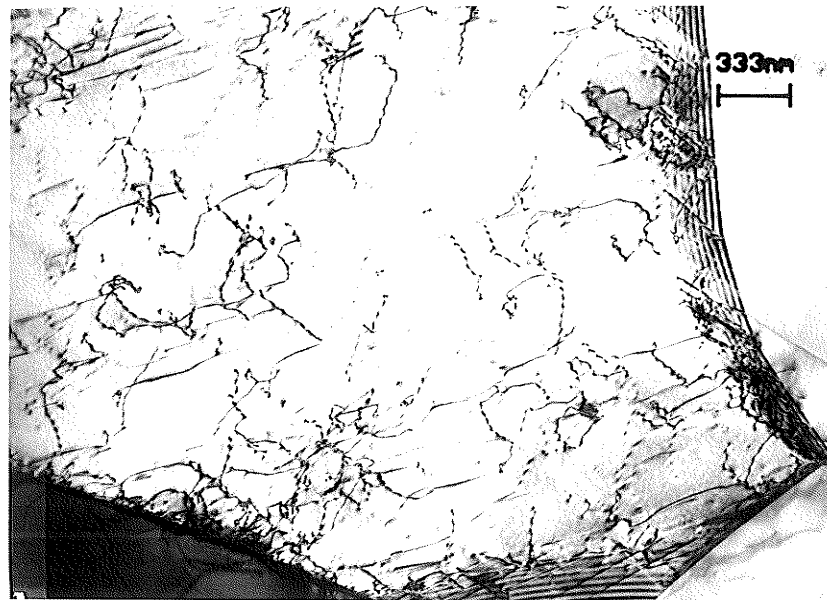


(b)

**Figure 4.7:** TEM micrographs typical of the as-annealed material with grain size of  $3.4\ \mu\text{m}$  showing (a) the grain interior with a low dislocation density and (b) the grain boundaries free of EGBDs.

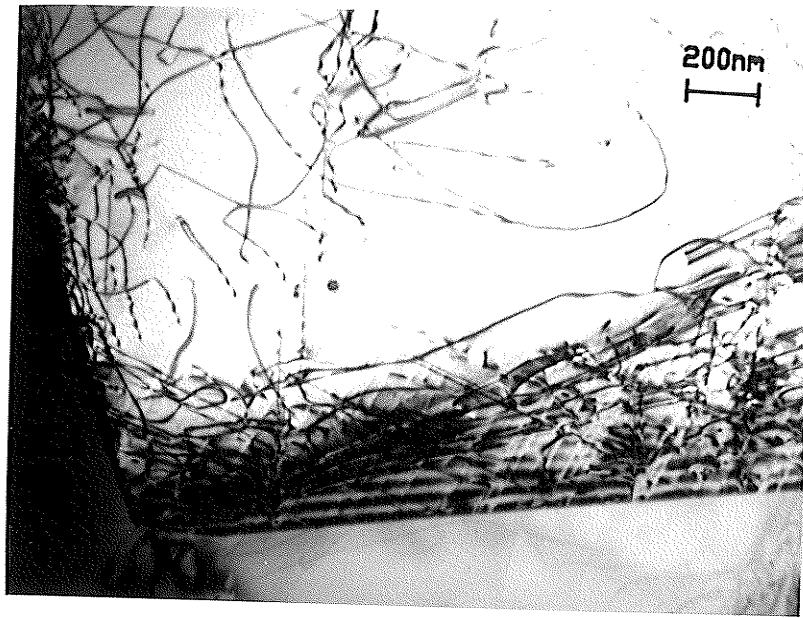


(a)

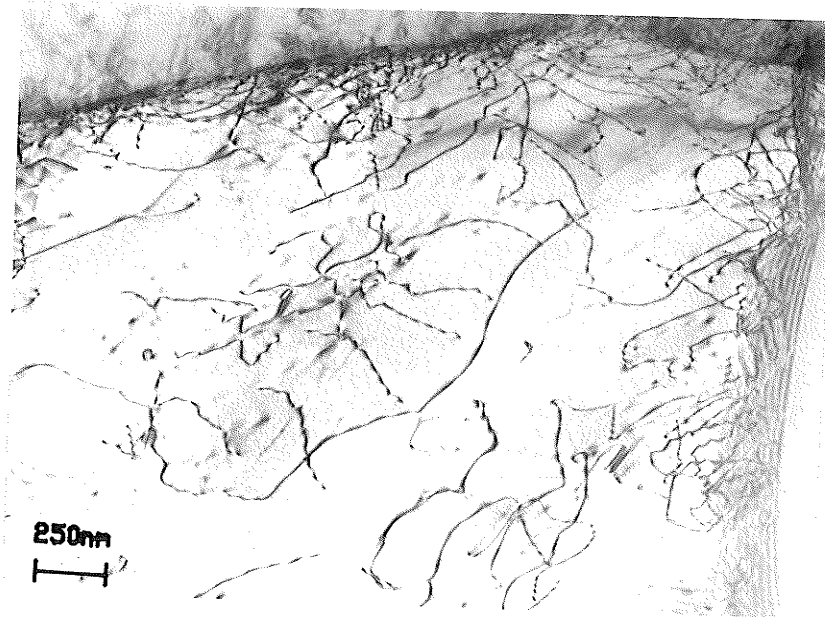


(b)

**Figure 4.8:** TEM micrographs showing the dislocation distribution of 2% pre-strained specimens of grain size  $3.4\ \mu\text{m}$  in (a) the grain boundary vicinity and (b) the grain interior.

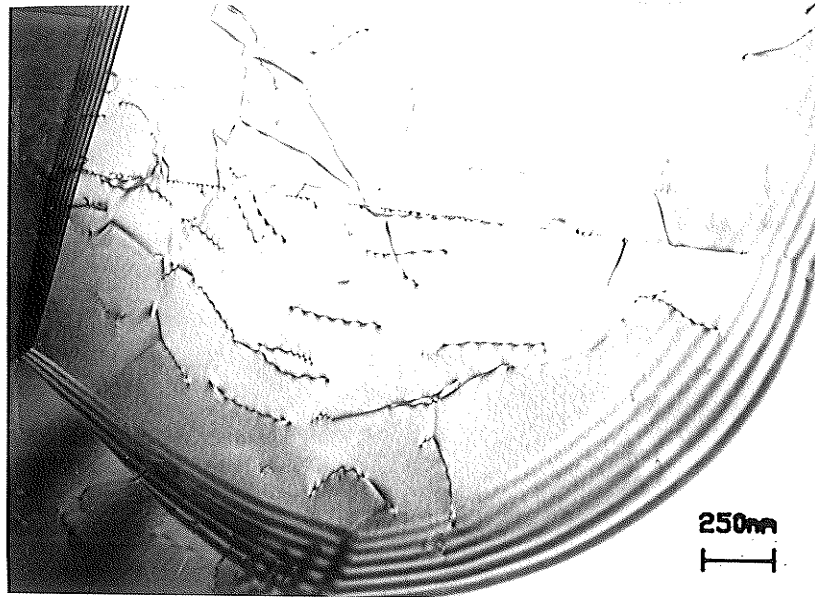


(a)

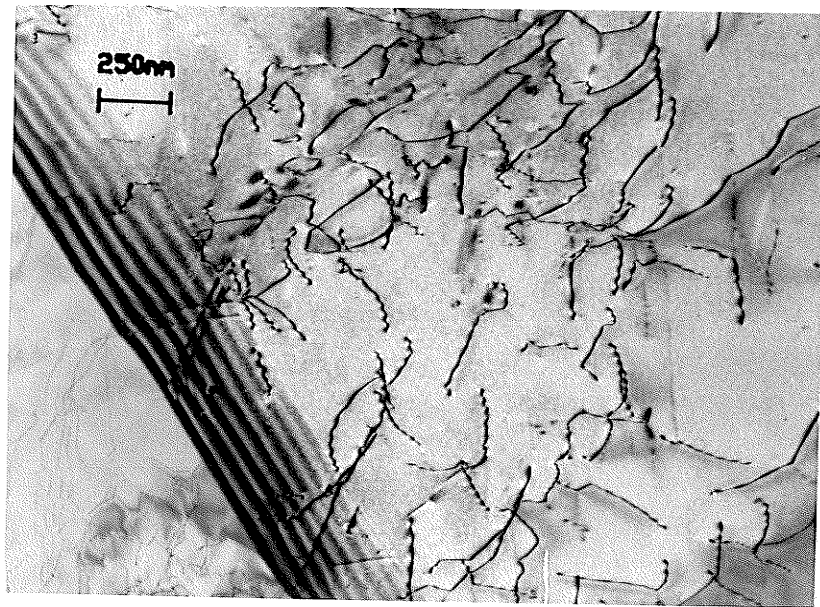


(b)

Figure 4.9: TEM micrographs showing the dislocation distribution in the grain boundary vicinity and the grain interior in specimens of grain size  $3.4\ \mu\text{m}$  which were pre-strained to 2% and annealed at  $600^\circ\text{C}$  for 5 minutes.



(a)



(b)

**Figure 4.10:** TEM micrographs showing (a) a dislocation free zone near a curved grain boundary and (b) a high density of dislocation in the grain interior and a grain boundary free of EGBDs for 3.4  $\mu\text{m}$  grain size specimens which were pre-strained to 2% and annealed at 800°C for 5 minutes.



the micrographs from specimen A (representing the as-annealed condition) which are typical for a fine grained as-annealed materials. The density of dislocations in the grain interior was estimated<sup>\*</sup> to be approximately  $10^7 \text{ cm}^{-2}$ . From figures (4.7) it can also be observed that the grain boundaries are free of EGBDs. After 2% pre-strain the density of dislocations within the grains was observed to increase to about  $2.5 \times 10^9 \text{ cm}^{-2}$ . This value corresponds well with that estimated from the relation between strain  $\epsilon$ , dislocation density  $\rho$  and the mean dislocation path  $\bar{x}$ :

$$\epsilon = \rho b \bar{x} \quad (4.1)$$

assuming that  $\bar{x}$  is equal to the mean intercept length. The dislocations were observed to be non-uniformly distributed within the grain volume, the highest density of dislocations being in the regions close to the grain boundaries. Similar observations made by Murr and Wang (1982) in 304 stainless steel also show such a non-uniform distribution of dislocations. Emission profiles and dislocation pile-ups at the grain boundaries were also observed, as shown in the micrographs of figure (4.8). The density of EGBDs formed as result of 2% pre-strain was observed to be  $10^7 \text{ cm}^{-1}$ .

The density of dislocations within the grains was

---

<sup>\*</sup>The dislocation density was estimated by counting the number of dislocation segments in a given area on the micrographs.

observed to remain approximately constant on subsequent annealing of the pre-strained specimens at 600°C and 800°C for 5 minutes, as shown in the TEM micrographs of figures (4.9) and (4.10). The differences in these two specimens lie in the different dislocation structure at and in the vicinity of grain boundaries. Annealing at 800°C for 5 minutes results in the disappearance of the contrast of EGBDs as can be seen in figure (4.10a) (with the exception of twin boundaries where EGBDs are observed to be stable). The density of dislocations in the vicinity of grain boundaries is significantly lower than the densities observed in the case of the specimen annealed at 600°C for 5 minutes. *Dislocation free zones* near the grain boundaries were observed for the specimen annealed at 800°C. A typical example is shown in figure (4.10a).

TEM observations in all the specimens indicate that the material contains small number of precipitates. Some colonies of precipitates were observed which were identified as  $M_{23}C_6$  type of precipitates. No precipitates were observed at grain boundaries. The pre-straining and the subsequent annealing appeared to have no effect on the precipitate density or the distribution. These observations suggest that the precipitates were present in the bulk material prior to the thermo-mechanical treatment. The micro-probe analysis using an EDAX system showed no changes in the chemical composition

in regions near the grain boundaries and away from the grain boundaries in the grain interior in all the specimens A through D.

#### 4.1.2. STRUCTURE-PROPERTY CORRELATION

Annealing at 600°C, i.e., at the temperature below  $T_c$ , does not change the mean grain boundary length. However, there is a small decrease in the standard deviation of dihedral angles (see Table 4.3) which indicates that a slight rearrangement of the grain boundary network occurs even at this low temperature. TEM observations (shown in figure 4.9) on the same specimen show that there is no significant change in the density of dislocations in the vicinity of grain boundaries. Thus, there is no evidence for significant change in the grain boundary structure as a result of annealing at 600°C. This deduction corresponds to the fact that yield stress does not change up to annealing temperatures of 600°C, as shown in figure (4.1a).

From Table (4.3), it can be seen that annealing at 800°C for 5 minutes results in a significant increase in grain boundary length and a further decrease in the standard deviation of the dihedral angles. The value of the standard deviation of the dihedral angles is even lower than that obtained for the as-annealed material. TEM observations in

figure (4.10) show that as a result of annealing at 800°C the image contrast of EGBDs is not visible in most grain boundaries. There is also a significant reduction in the density of dislocations near the grain boundaries. However, no measurable changes in the density of dislocations were observed in the grain interior. Table (4.4) gives a general overview of the processes occurring as a function of annealing temperature after a given pre-strain  $\epsilon$ .

From the observations listed in Table (4.4), it can be concluded that the recovery of yield stress is associated with changes in both the geometry of the grain boundary network and the density of dislocations at and in the vicinity of grain boundaries. From the observations on the changes in the geometry of the grain boundary network, it is clear that grain boundary migration occurs over small distances as a result of annealing of pre-strained specimens. TEM observations show that annihilation of EGBDs, which leads to the transformation of non-equilibrium grain boundaries to their equilibrium state, is also accompanied with a decrease in the density of dislocations in the vicinity of grain boundaries. This decrease in the density of dislocations occurs due to the incorporation of these dislocations in migrating grain boundaries. The dislocations trapped as a result of grain boundary migration are then subsequently annihilated.

The above mechanism results in both the annihilation of EGBDs and the softening of the region in the vicinity of grain boundaries which in turn leads to the drop in yield stress.

In the next section a theoretical model has been developed to obtain the kinetics of the annihilation of EGBDs. The results of the computations of the model show that the rate of annihilation of EGBDs, i.e., rate of transformation of non-equilibrium grain boundaries to their equilibrium state is in agreement with the observed variation in the yield stress. It can therefore be concluded that the annihilation of EGBDs is the rate controlling process in the relaxation of the stresses in the vicinity of grain boundaries.

#### 4.2. A THEORETICAL MODEL FOR THE KINETICS OF TRANSFORMATION OF NON-EQUILIBRIUM GRAIN BOUNDARIES TO THEIR EQUILIBRIUM STATE

In the previous section it was shown through detailed experimental observations that the changes in the grain boundary state are related to the observed drop in the yield stress (see figures 4.1 and 4.2) during annealing of 2% pre-strained polycrystals of 316L stainless steel. One of the significant conclusions of the experimental observations which may be re-emphasized is that grain boundary migration

TABLE 4.4

An overview of the processes occurring as a function of annealing temperature after a given pre-strain  $\epsilon$ .

Annealing Temperature $T$	Values Compared with That of the Prestrained Sample					Density of Dislocations	
	Yield Stress	Mean Intercept Length	Chemical Composition	Mean Grain Boundary Length	Standard Deviation of Dihedral Angles	At and in the Vicinity of Grain Boundaries	In Grain Interior
$T \leq T_c$	no change			no change	slight decrease	slight decrease	
$T_c < T < T_r$	drop			increase	decrease	decrease	no change
$T \geq T_r$	drop to value of as-annealed material	changes negligible with respect to changes in yield stress	no change in the concentration of the main elements near grain boundaries and in the grain interior	significant increase (as much as 21 pct)	decrease to value of as-annealed sample	most GB's free of EGBD image contrast except twin boundaries	

$T_r$  = temperature of the recovery of yield stress.

occurs as a result of annealing and that this migration is associated with the annihilation of dislocations at and in the vicinity of grain boundaries. In this section a theoretical model has been developed for the transformation of the grain boundaries from the non-equilibrium state to the equilibrium state. The model gives a quantitative description of the kinetics of the recovery process.

The proposed theoretical model relates the changes in the microstructure, as a result of annealing of pre-strained specimens, to the annihilation of EGBDs. The kinetics of the annihilation of EGBDs has been calculated and the results obtained have been found to be in agreement with the experimental observations.

#### 4.2.1. DEVELOPMENT OF THE MODEL FOR THE ANNIHILATION OF EGBDs

The phenomenon of annihilation of EGBDs can be envisaged to be composed of two stages. In stage I the experimentally observed widening of the image of EGBDs on random grain boundaries and its eventual disappearance occurs. In this stage some relaxation of the elastic stresses occurs. The process (discussed in detail in section 2.2) is described either by spreading of the EGBDs core (Pumphrey and Gleiter 1974) or by dissociation of EGBDs (Johannesson and Tholen 1972) into a number of dislocations with small Burgers

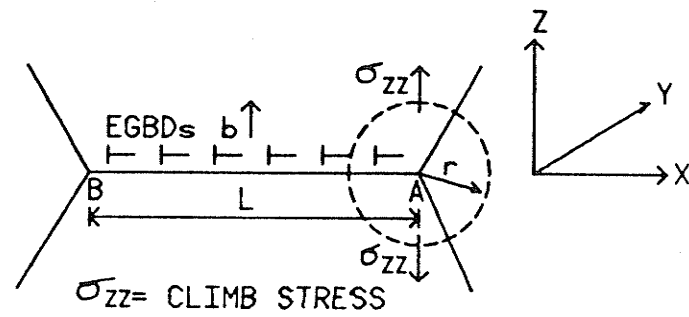
vectors. However, as discussed earlier, such a process can only explain the disappearance of the EGBD contrast in the TEM image but does not explain the complete annihilation of EGBDs which would require the value of the total Burgers vector to go to zero. Thus, on the completion of stage I grain boundaries are still in a non-equilibrium state having residual stresses associated with partially relaxed EGBDs.

In stage II, the annihilation of EGBDs is proposed to occur by climb, under the influence of their interacting stress fields, towards the triple points. For the climb of EGBDs, the required flow of vacancies to the end of the extra half planes involves diffusion through the lattice as well as the grain boundary. Since the diffusion through the lattice is the slower process, it would be rate controlling.

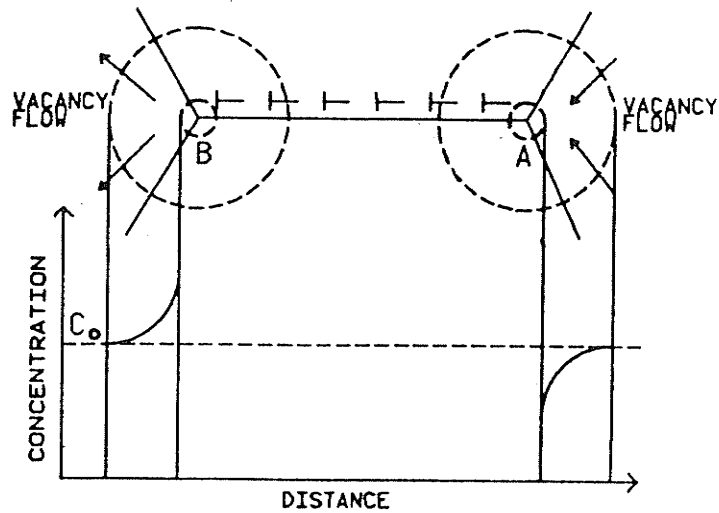
Figure (4.11a) shows a schematic of EGBDs at a grain boundary. It may be noted that the configuration of EGBDs shown in this figure resembles that of a tilt grain boundary. From this figure it can be seen that an outward flow of vacancies from triple point A will result in the climb of the lead dislocation towards the triple point, while the reverse is true for the triple point B.

The mechanism of annihilation of EGBDs at the triple points is believed to occur as a result of reactions with other EGBDs climbing to the triple point on adjacent grain boundaries. However, the details of the dislocation reactions





(a)



(b)

**Figure 4.11:** A schematic of (a) EGBDs at a grain boundary and (b) the vacancy concentration profile in the vicinity of triple points A and B.

which lead to the eventual annihilation of EGBDs are not relevant to the development of the model which describes the kinetics of transformation of non-equilibrium grain boundaries to equilibrium grain boundaries.

In order to quantitatively describe the transformation kinetics, first the stress field and the vacancy concentration gradient will be calculated around the triple points. Then assuming a steady state, the flux of vacancies to or from the triple points will be determined. Finally, the vacancy flux will be related to the dislocation climb rate and the annihilation rate of EGBDs. The equations have been rigorously derived for a meaningful comparison between the theoretical and the experimental results.

#### 4.2.1.1. STRESS FIELD AT THE TRIPLE POINTS

Figure (4.11a) shows a certain density of EGBDs lying on a grain boundary of length  $L$ . The boundary plane is parallel to the  $yz$  plane and the dislocation lines are parallel to the  $z$ -axis. The Burgers vector is perpendicular to the boundary plane, i.e., parallel to the  $x$ -axis.

The stress field of the EGBDs can be calculated by adding the individual stress field of each dislocation. It is evident from figure (4.11a) that  $\sigma_{xx}$  is the only stress component which will produce a climb force on the

dislocations.  $\sigma_{xx}$  is given by the following relationship (Hirth and Lothe 1982):

$$\sigma_{xx} = - \frac{Gb\rho}{2\pi(1-\nu)} \left\{ \frac{x^2}{x^2 + y^2} - \frac{x^2}{x^2 + (y + L)^2} + \frac{1}{2} \ln \left( \frac{x^2 + (y + L)^2}{x^2 + y^2} \right) \right\} \quad (4.2)$$

where  $G$  is the shear modulus,  $\nu$  is the Poisson ratio and  $\rho$  is the density of EGBDs. By applying the transformation:  $x = r \sin\theta$  and  $y = r \cos\theta$ , the climb stress at a distance  $r$  from the triple point A can be written as:

$$\sigma_{xx} = - \frac{Gb\rho}{2\pi(1-\nu)} \left\{ \sin^2\theta - \frac{r^2 \sin^2\theta}{r^2 + L^2 + 2rL \cos\theta} + \frac{1}{2} \ln \left( \frac{r^2 + L^2 + 2rL \cos\theta}{r^2} \right) \right\} \quad (4.3a)$$

Similarly, the climb stress at a distance  $r$  from the triple point B is given by:

$$\sigma_{xx} = \frac{Gb\rho}{2\pi(1-\nu)} \left\{ \sin^2\theta - \frac{r^2 \sin^2\theta}{r^2 + L^2 + 2rL \cos\theta} + \frac{1}{2} \ln \left( \frac{r^2 + L^2 + 2rL \cos\theta}{r^2} \right) \right\} \quad (4.3b)$$

A closer examination of equations (4.3a) and (4.3b) reveals the following:

1. Triple point A is subjected to a compressive stress, while triple point B is subjected to a tensile stress. Therefore, there will be a flux of vacancies from the grain interior into the triple point A and a flux of vacancies from the triple point B into the grain interior.
2. The climb stress is dependent not only on the dislocation density but also on the length of the grain boundary.

#### 4.2.1.2. VACANCY CONCENTRATION PROFILE AT THE TRIPLE POINTS

If  $V$  is the atomic volume, then the energy lost or gained when an atomic length of dislocation line climbs one atomic distance is given by  $\sigma_{xx} V$ . The vacancy concentration can now be determined by equating this energy to the chemical potential of the vacancies. The chemical potential of vacancies is equal to  $kT \ln \left( \frac{C}{C_0} \right)$ , where  $k$  is the Boltzmann constant,  $C$  is the actual number of vacancies per unit volume and  $C_0$  is the equilibrium concentration of vacancies. Thus, the local equilibrium concentration of vacancies at a triple point can be written as (Hirth and Lothe 1982):

$$C = C_o \exp\left(\frac{\sigma_{xx} V}{kT}\right) \quad (4.4)$$

If  $\sigma_{xx} V \ll kT$  (which is a reasonable assumption), then equation (4.4) can be re-written as follows:

$$C \simeq C_o \left(1 + \frac{\sigma_{xx} V}{kT}\right) \quad (4.5)$$

Assuming that the long range stress field (due to the interacting stress fields of other non-equilibrium grain boundaries) can be neglected, the vacancy concentration away from the triple point (at  $r = R_o$ , in the grain interior) is  $C_o$ , while near the triple point (at  $r = r_o$ ) is  $C(r_o, \theta)$ . Substituting the expressions for  $\sigma_{xx}$  from equations (4.3a) and (4.3b) in equation (4.5), the vacancy concentration near the triple point A is given by

$$C(r_o, \theta) = C_o \left\{ 1 - \frac{GbV\rho}{2\pi(1-\nu)kT} \left[ \sin^2\theta - \frac{r_o^2 \sin^2\theta}{r_o^2 + L^2 + 2r_o L \cos\theta} + \frac{1}{2} \ln\left(\frac{r_o^2 + L^2 + 2r_o L \cos\theta}{r_o^2}\right) \right] \right\} \quad (4.6a)$$

and the vacancy concentration near triple point B is given by

$$C(r_o, \theta) = C_o \left\{ 1 + \frac{GbV\rho}{2\pi(1-\nu)kT} \left[ \sin^2\theta - \frac{r_o^2 \sin^2\theta}{r_o^2 + L^2 + 2r_o L \cos\theta} + \frac{1}{2} \ln \left( \frac{r_o^2 + L^2 + 2r_o L \cos\theta}{r_o^2} \right) \right] \right\} \quad (4.6b)$$

The average concentration,  $\bar{C}(r_o)$  at the two triple points A and B can be obtained by integrating equations (4.6a) and (4.6b):

$$\bar{C}(r_o) = \frac{1}{\pi} \int_0^\pi C(r_o, \theta) d\theta \quad (4.7)$$

Using equations (4.6a), (4.6b) and (4.7), the average vacancy concentration  $\bar{C}(r_o)$  at triple points A and B is given by the equations:

$$\bar{C}(r_o) = C_o \left\{ 1 - \frac{GbV\rho}{4\pi(1-\nu)kT} \left[ 1 - 2 \ln \left( \frac{r_o}{L} \right) \right] \right\} \quad (4.8a)$$

and

$$\bar{C}(r_o) = C_o \left\{ 1 + \frac{GbV\rho}{4\pi(1-\nu)kT} \left[ 1 - 2 \ln \left( \frac{r_o}{L} \right) \right] \right\} \quad (4.8b)$$

respectively. See appendix B for the details of the solution of the integral in equation (4.7).

Assuming steady state conditions, i.e.,  $\frac{\delta C}{\delta t} = 0$ , Fick's second law of diffusion can be written as (Shewmon 1963):

$$\frac{\delta^2 C}{\delta r^2} + \frac{1}{r} \frac{\delta C}{\delta r} = 0 \quad (4.9)$$

with the following boundary conditions:

$C = C_o$  at  $r = R_o$  (grain interior),

$C = \bar{C}(r_o)$  at  $r = r_o$  (near a triple point; the concentration is given by equations 4.8a and 4.8b), and

$R_o \gg r_o$ .

Using equations (4.8a) and (4.8b), the solution to equation (4.9) which satisfies the above boundary conditions gives the vacancy concentration profile around the triple point A and is given below:

$$C(r) = C_o \left\{ 1 - \frac{GbV\rho}{4\pi(1-\nu)kT} \left[ 1 - 2 \ln\left(\frac{r_o}{L}\right) \frac{\ln\left(\frac{R_o}{r}\right)}{\ln\left(\frac{R_o}{r_o}\right)} \right] \right\} \quad (4.10a)$$

The vacancy concentration profile around the triple point B is given by

$$C(r) = C_o \left\{ 1 + \frac{GbV\rho}{4\pi(1-\nu)kT} \left[ 1 - 2 \ln\left(\frac{r_o}{L}\right) \frac{\ln\left(\frac{R_o}{r}\right)}{\ln\left(\frac{R_o}{r_o}\right)} \right] \right\} \quad (4.10b)$$

Figure (4.11b) shows the schematic plots of the vacancy

concentration profiles obtained from equations (4.10a) and (4.10b). From the figure it can be seen that the vacancy concentration at triple point A is lower than in the grain interior, while the reverse is true at triple point B. Thus, it is obvious that the climb of dislocations will occur by vacancy annihilation at triple point A and vacancy emission at triple point B. With the knowledge of the vacancy concentration profile, the climb rate and the annihilation rate of EGBDs can now be derived.

#### 4.2.1.3. ANNIHILATION RATE OF EGBDs

Vacancy flux at a triple point is given by

$$J = - D_v \frac{\delta C}{\delta t} \quad (4.11)$$

where  $D_v$  is the diffusion coefficient for vacancies. The net vacancy flow per unit length of the triple edge (in 3-dimension) is given by

$$I = - 2\pi r D_v \frac{\delta C}{\delta r} \quad (4.12)$$

Therefore, the climb rate,  $\frac{dx}{dt}$  of the EGBDs can be written as

$$\frac{dx}{dt} = \frac{I V}{b} \quad (4.13)$$



where  $b$  is the Burgers vector of the dislocations.

In time  $\Delta t$ ,  $\rho \cdot 2\Delta x$  number of dislocations are annihilated, where  $\Delta x$  is the climb distance at each triple point. If  $\Delta\rho$  is the density of dislocations annihilated, then one can relate the climb rate to the annihilation rate in the following manner:

$$\frac{\Delta\rho}{\Delta t} = \frac{\rho}{L} \frac{2\Delta x}{\Delta t} \Rightarrow \frac{d\rho}{dt} = \frac{2\rho}{L} \frac{dx}{dt} \quad (4.14)$$

From equations (4.10) and (4.12) - (4.14), the annihilation rate is given by

$$\frac{d\rho}{dt} = - \frac{GV^2 C_o D_v \left\{ 1 - 2 \ln \left( \frac{r_o}{L} \right) \right\} \rho^2}{L(1-\nu)kT \ln \left( \frac{R_o}{r_o} \right)} \quad (4.15)$$

The term  $(VC_o D_v)$  in equation (4.15) is the atomic self-diffusion coefficient  $D_s$ , where  $D_s = D_o \exp \left( -\frac{\Delta Q}{RT} \right)$ ,  $D_o$  is the frequency factor, and  $\Delta Q$  is the activation energy for lattice self-diffusion. Thus, the annihilation rate of EGBDs becomes:

$$\frac{d\rho}{dt} = - \frac{GVD_s \left\{ 1 - 2 \ln \left( \frac{r_o}{L} \right) \right\} \rho^2}{L(1-\nu)kT \ln \left( \frac{R_o}{r_o} \right)} \quad (4.16)$$

On integration, equation (4.16) yields the following relationship between the density of EGBDs and the annealing temperature and time:

$$\frac{1}{\rho} - \frac{1}{\rho_o} = \left\{ \frac{\text{GVD}_s \left[ 1 - 2 \ln \left( \frac{r_o}{L} \right) \right]}{L(1-\nu)kT \ln \left( \frac{R_o}{r_o} \right)} \right\} t \quad (4.17)$$

where  $\rho$  is the instantaneous density of EGBDs and  $\rho_o$  is the initial density of EGBDs.

On examining equations (4.16) and (4.17), the following important conclusions can be drawn:

1. The rate of annihilation,  $\frac{d\rho}{dt}$ , of EGBDs is dependent on the annealing temperature  $T$ , the grain size or the grain boundary length  $L$  and the instantaneous density  $\rho$ , of EGBDs. The annihilation rate increases as the square of the density of EGBDs. This is expected, since higher dislocation density implies a higher climb stress at the triple points.
2. The density of EGBDs for a given annealing time and temperature and for a given grain size, is a function of the initial density,  $\rho_o$ , of EGBDs. Higher the initial density of EGBDs, a larger time or temperature would be required for the equilibration of non-equilibrium grain boundaries.
3. The relation between grain size and the annihilation

rate of EGBDs appears to be more complicated. From equations (4.16) and (4.17), it can be shown that for a constant initial density of EGBDs, a larger grain size results in a decreased annihilation rate, thereby increasing the annealing time and temperature for the equilibration process. A more detailed discussion on this grain size effect is deferred to section (4.3.7).

#### 4.2.2. CALCULATIONS

Equation (4.17) was employed to calculate the variation of the ratio  $\left( \frac{\rho}{\rho_0} \right)$  of the instantaneous density of EGBDs ( $\rho$ ) to the initial density of EGBDs ( $\rho_0$ ) as a function of the annealing temperature and time for 316L stainless steel. The values of the material parameters of equation (4.17) are given in Table (4.5).

The value of  $r_0$  is taken to be equal to the value of the Burgers vector  $b$ .  $R_0$  is the distance from the triple point where the vacancy concentration is  $C \approx C_0$ . Since some triple points emit vacancies and some absorb vacancies, a reasonable value of  $R_0$  is half the distance between the triple points. From equations (4.16) and (4.17) it can be easily shown that the annihilation rate of EGBDs is insensitive to the precise value of  $R_0$ . The initial density  $\rho_0$  was directly measured

TABLE 4.5

Values of material parameters for 316L stainless steel.

Parameter	Value	Reference
k	$1.18 \times 10^{-23} \text{ J.K}^{-1}$	Weast 1972
G	$8.43 \times 10^{10} \text{ N.m}^{-2}$	Boyer and Gall 1985
V	$8.38 \times 10^{-30} \text{ m}^3$ (calculated from atomic size)	
$D_o$	$1.74 \times 10^{-4} \text{ m}^2.\text{s}^{-1}$	Smith and Gibbs 1969
$\Delta Q$	$68 \text{ kcal.mol}^{-1}$	Smith and Gibbs 1969
b	$2.52 \times 10^{-10} \text{ m}$	
$\rho_o$	$10^8 \text{ m}^{-1}$ (calculated from electron micrographs)	
L	$2.28 \mu\text{m}$ & $12.0 \mu\text{m}$ for grain sizes of $3.4 \mu\text{m}$ & $18.0 \mu\text{m}$ (experimentally measured)	
$\nu$	0.283	Boyer and Gall 1985
R	$1.995 \text{ cal.mol}^{-1}.\text{K}^{-1}$	Weast 1972

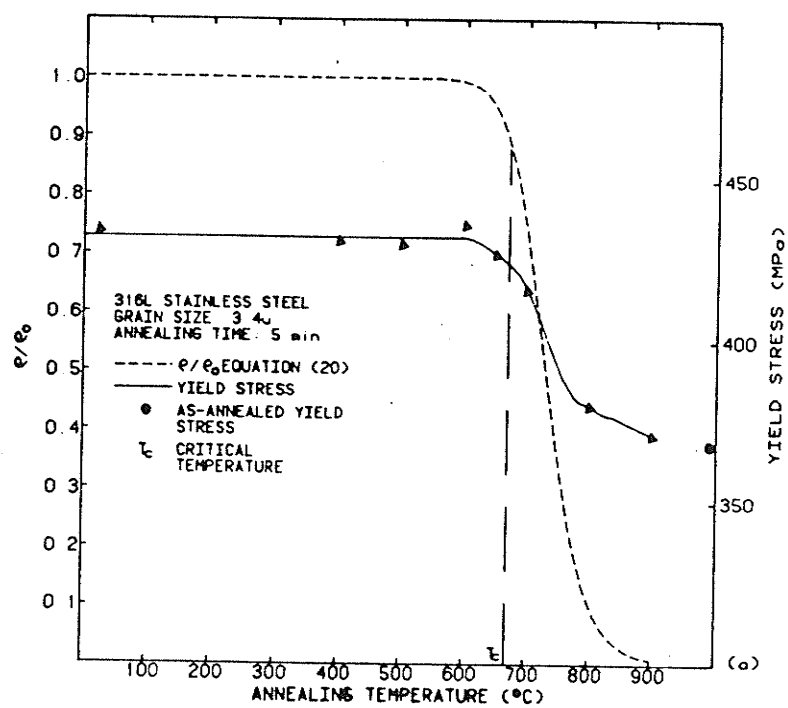
from the electron micrographs for the specimens of grain size  $3.4 \mu\text{m}$ . For the coarse grained specimens (grain size:  $18.0 \mu\text{m}$ ),  $\rho_o$  was assumed to be the same as that for the fine grained specimens.

#### 4.2.3. COMPARISON OF THE PREDICTED RESULTS WITH EXPERIMENTAL OBSERVATIONS

Using equation (4.17), figures (4.12a) and (4.12b) show the calculated plots (broken lines) of the ratio  $\left(\frac{\rho}{\rho_o}\right)$  versus annealing temperature at a constant annealing time of 5 minutes for 316L stainless steel with grain sizes of  $3.4 \mu\text{m}$  and  $18.0 \mu\text{m}$  respectively. Figures (4.13a) and (4.13b) show the calculated variation (broken lines) of the ratio  $\left(\frac{\rho}{\rho_o}\right)$  with annealing time at constant annealing temperatures of  $800^\circ\text{C}$  and  $750^\circ\text{C}$  respectively for 316L stainless steel of grain size  $3.4 \mu\text{m}$ . For the purpose of comparison the yield stress variation (solid lines) with annealing temperature and time shown in figures (4.1) and (4.2) are reproduced in figures (4.12) and (4.13) respectively.

Comparing the predicted and the experimental results from figures (4.12) and (4.13), the following important observations may be deduced.

1. The general trend of the predicted variation of the density of EGBDs with annealing temperature or



(a)

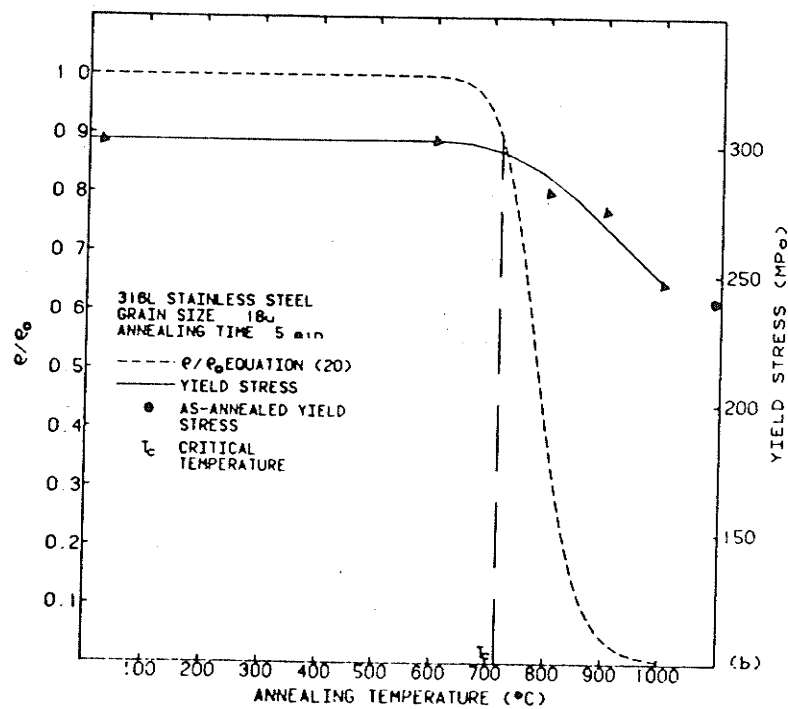
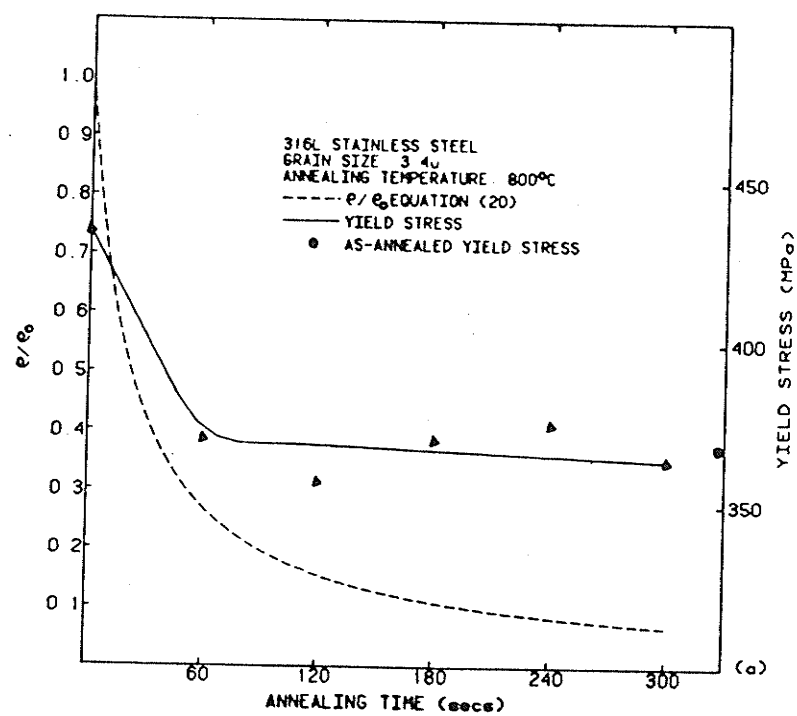
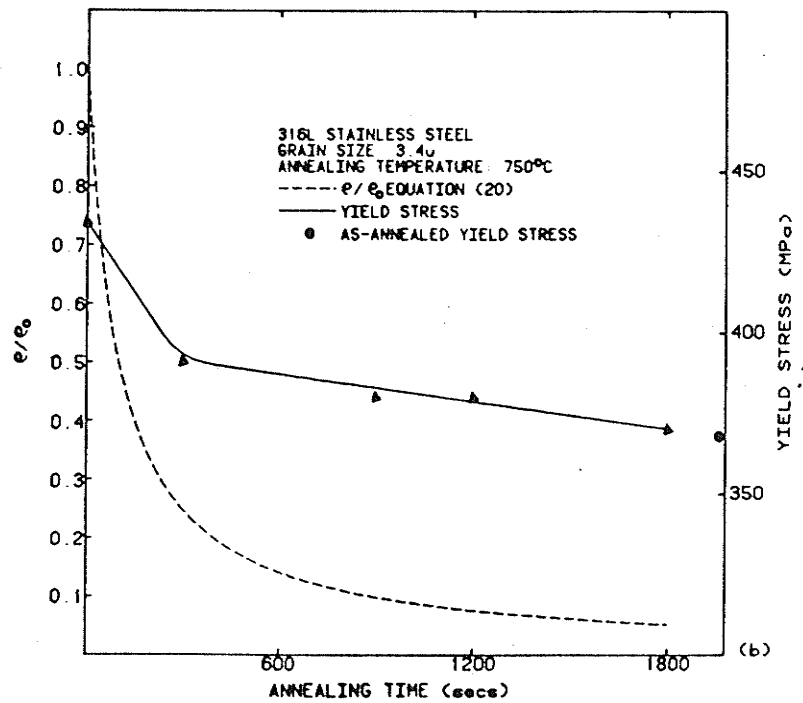


**Figure 4.12:** Variation of  $\frac{\rho}{\rho_0}$  (broken line) and yield stress (solid line) as a function of annealing temperature for a constant annealing time of 5 minutes after 2% pre-strain in 316L stainless steel specimens of grain sizes (a) 3.4  $\mu\text{m}$  and (b) 18.0  $\mu\text{m}$ .



(a)





(b)  
**Figure 4.13:** Variation of  $\frac{\rho}{\rho_0}$  (broken line) and yield stress (solid line) as a function of annealing time for 2% pre-strained specimens of 316L stainless steel specimens of grain size 3.4  $\mu\text{m}$  at constant annealing temperatures of (a) 800°C and (b) 750°C.

annealing time is very similar to the experimentally observed variation of the yield stress with annealing temperature or annealing time.

2. The predicted temperature at which the density of EGBDs is observed to drop is close to the critical temperature  $T_c$  beyond which the yield stress is observed to drop (see Table 4.2). The predicted and the experimental critical temperature are approximately equal ( $T_c \approx 680^\circ\text{C}$  and  $750^\circ\text{C}$  for 316L stainless steel with grain sizes of  $3.4\ \mu\text{m}$  and  $18.0\ \mu\text{m}$  respectively).
3. From figures (4.12a) and (4.12b), it can be seen that the stabilization of the yield stress at high temperatures is in agreement with the very low density (less than 10% of the initial density) of EGBDs predicted by equation (4.17).
4. Figures (4.13a) and (4.13b) show the variation of the density of EGBDs as a function of annealing time for constant annealing temperatures of  $800^\circ\text{C}$  and  $750^\circ\text{C}$  respectively. From the figures it can be seen that the density of EGBDs drops continuously with annealing time until it reaches low values (less than 10%) at annealing times of  $\approx 5$  minutes (figure 4.13a) and  $\approx 30$  minutes (figure 4.13b) for annealing temperatures of  $800^\circ\text{C}$  and  $750^\circ\text{C}$  respectively. The

yield stress curves also show a similar trend, i.e., the yield stress drops continuously with annealing time until it reaches the yield stress of the as-annealed material in approximately 5 minutes (figure 4.13a) and approximately 30 minutes (figure 4.13b) for annealing temperatures of 800°C and 750°C respectively.

5. As discussed in section (4.2.1.3), the model predicts a decreased annihilation rate, thereby increasing the annealing time and temperature for the annihilation of EGBDs with increasing grain size. Such a behavior can be seen in the predicted curves of figures (4.12a) and (4.12b). This observation is corroborated by the experimental results obtained on 316L stainless steel with grain sizes of 3.4  $\mu\text{m}$  and 18.0  $\mu\text{m}$  respectively. Coarse grained specimens (figure 4.12b) had to be annealed at higher temperatures (1000°C) than the fine grained specimens (figure 4.12a) for the recovery of yield stress.

The results of the calculations discussed above and the changes in the geometry of the grain boundary network (discussed in section 4.1.1.2) leads to the conclusion that the process of annihilation of EGBDs occurs together with grain boundary migration. This is not unexpected in view of the in-situ TEM observations (Pumphrey and Gleiter 1974, and

Varin, Lojkowski and Valiev 1981) which show that spreading of EGBDs occurs simultaneously with grain boundary migration. Since the phenomenon of spreading involves climb of partial dislocations (see section 2.2), it may be concluded that climb of grain boundary dislocations results in grain boundary migration. Such a mechanism has also been proposed by Smith and King (1981) which shows that climb of dislocations must result in the migration of grain boundaries. The metallographic measurements made in section (4.1.1.2) confirm that grain boundary migration takes place on annealing of pre-strained specimens. However, it is difficult to obtain from the data a quantitative relationship between the distance of migration and the climb distance of EGBDs (the climb distance can be related to the number of EGBDs annihilated). Therefore, only a qualitative analysis is possible. It is seen that the onset of the changes in the grain boundary geometry (see Table 4.3) correspond to the onset of annihilation of EGBDs (see figure 4.12a) for 316L stainless steel of grain size  $3.4 \mu\text{m}$ . For example, the observed decrease in the standard deviation of dihedral angles (see Table 4.3) suggests that grain boundary migration occurs at an annealing temperature of  $600^{\circ}\text{C}$ . This observation appears to be in agreement with the onset of annihilation of EGBDs (see figure 4.12a) predicted at  $680^{\circ}\text{C}$ . The above results provide considerable support to the validity of the

theoretical model developed for the kinetics of the annihilation of EGBDs.

Even though only a qualitative comparison was possible between the predicted variation of the density of EGBDs and the experimental variation of the yield stress and the changes in the microstructure with annealing treatment, the model developed here is able to explain the experimental results. The model also emphasises the fact that the structure of grain boundaries plays an important role in the mechanical properties of polycrystals. In the next section a more detailed analysis has been carried out on the role of grain boundary structure on the flow stress of polycrystals over a wider range of grain sizes.

#### 4.3. THE ROLE OF GRAIN BOUNDARIES IN THE GRAIN SIZE DEPENDENCE OF FLOW STRESS IN POLYCRYSTALS

The flow stress  $\sigma(\epsilon)$  of polycrystals follows a Hall-Petch type of relationship which is reproduced below from equation (2.10):

$$\sigma(\epsilon) = \sigma_0(\epsilon) + K(\epsilon)\ell^{-1/2} \quad (4.18)$$

where  $\ell$  is the mean grain size and  $\sigma_0(\epsilon)$  and  $K(\epsilon)$  are constants at a given strain  $\epsilon$ .

As discussed in section 2.3, several models (Hall 1951, Petch 1953, Conrad 1963, Ashby 1970, and Thompson et al 1973)

have been proposed to rationalize the linear dependence of  $\sigma(\epsilon)$  on  $\ell^{-1/2}$  in equation (4.18). However, the models are unable to predict uniquely the strain dependence of the Hall-Petch parameters  $\sigma_o(\epsilon)$  and  $K(\epsilon)$ . This may be attributed to the fact, common to all the models, that changes in the properties of grain boundaries during plastic deformation are neglected.

It was shown in sections (4.1) and (4.2) that extrinsic grain boundary dislocations (EGBDs) have a significant influence on the yield stress of polycrystals. It has been suggested by Murr (1974, 1975 and 1981) and shown theoretically by Varin et al (1987) that EGBDs act as stress concentrators thereby reducing the stress required to generate dislocations at and in the vicinity of grain boundaries (discussed in section 2.3.2).

In this section the influence of EGBDs on the grain size dependence of flow stress in 316L stainless steel has been examined. The variation of the Hall-Petch parameters  $\sigma_o(\epsilon)$  and  $K(\epsilon)$  have been discussed in terms of the microstructural changes at the grain boundaries and in the grain interior.

#### 4.3.1. EXPERIMENTAL RESULTS

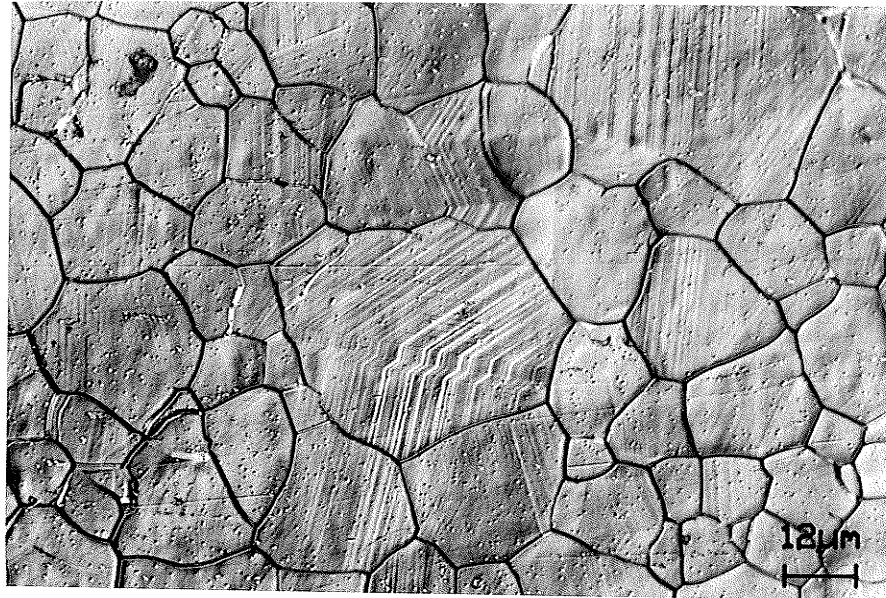
Experiments were performed on 316L stainless steel specimens of grain sizes varying from 3.4  $\mu\text{m}$  to 22.4  $\mu\text{m}$ .

Table (3.2) lists the individual values of grain sizes produced at different annealing temperatures.

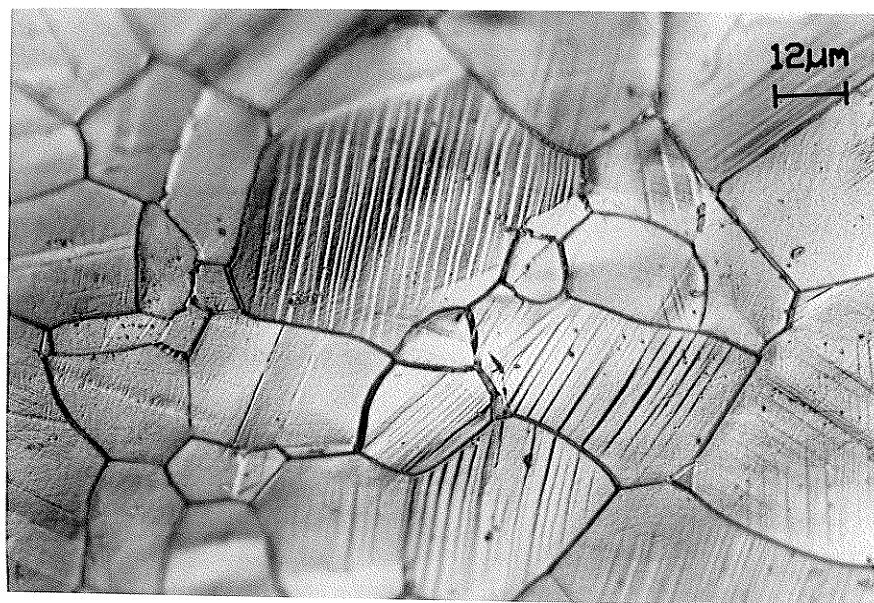
The specimens were strained to 2% and 5% under tension at room temperature. The 2% pre-strained specimens were then annealed at temperatures in the range of 550°C to 800°C for annealing times varying from 1 to 30 minutes. The pre-strained and annealed specimens were again tested in tension at room temperature.

#### 4.3.1.1. SLIP LINE OBSERVATIONS

Figures (4.14a) and (4.14b) show typical optical micrographs of slip lines observed on the surface of the specimens after 2% and 5% plastic deformation respectively. From the figures it can be seen that the slip lines are straight indicating that the dislocations in this material are confined to their slip planes and as such cross-slip is not prevalent. Since 316L stainless steel is a low stacking fault energy material (SFE), no cross-slip is expected at such small strains at room temperature. Another important observation that can be made from figure (4.14) is that all the slip lines appear to cross twin boundaries. Therefore, it may be inferred that the twin boundaries are not a barrier to slip at small strains. In view of this observation, twin boundaries were ignored in the grain size size measurements



(a)



(b)

**Figure 4.14:** Optical micrographs of slip lines after (a) 2% and (b) 5% plastic deformation in 316L stainless steel specimens of grain size  $22.4\ \mu\text{m}$ .



(see section 3.4).

#### 4.3.1.2. TENSION TEST RESULTS

##### 4.3.1.2.1. AS-ANNEALED SPECIMENS

Figure (4.15) shows the stress-strain curves for the as-annealed specimens of varying grain sizes deformed up to 2% strain. This figure shows that the stress-strain curves exhibit a linear hardening characteristic beyond 0.2% plastic strain. It may be noted that a few specimens were strained to 5% (not shown in figure 4.15) and their stress-strain curves also exhibited linear hardening. Therefore, the flow stress,  $\sigma(\epsilon)$  in the range of 0.2% to 5% strain can be related to the plastic strain ( $\epsilon$ ) by the Ludwik's equation (Ludwik 1909) in which the strain exponent is unity:

$$\sigma(\epsilon) = A + B\epsilon \quad (4.19)$$

where A and B are constants. B in equation (4.19) represents the work-hardening rate  $\left(\frac{d\sigma}{d\epsilon}\right)$ . The values of A and B were calculated by fitting a least square line on the data shown in figure (4.15). The individual values of A and B for different grain size specimens are listed in Table (4.6). This table shows that the work-hardening rate increases with increasing grain size. The constant A decreases with increasing grain size.

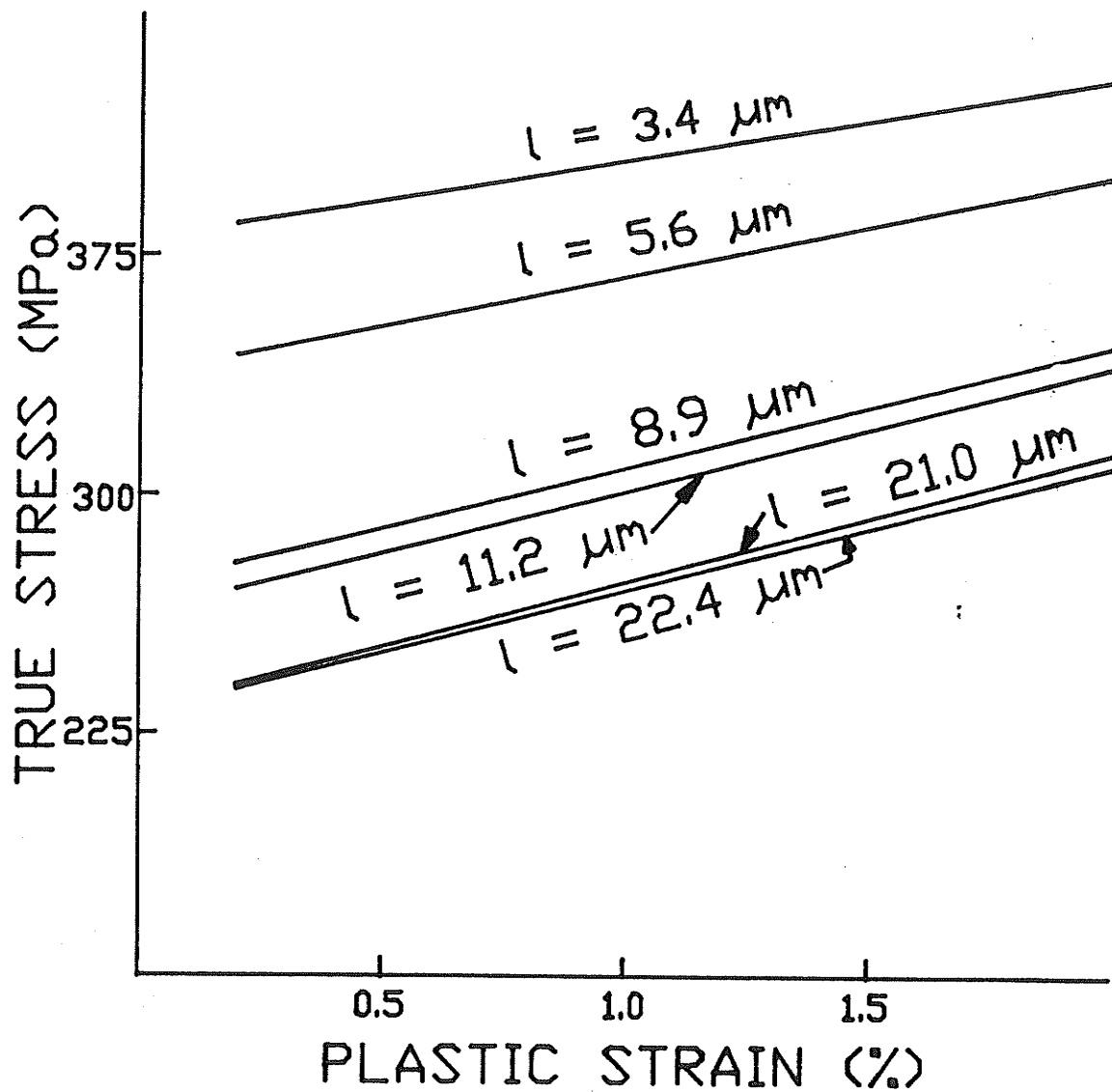


**Figure 4.15:** Stress-strain curves for the as-annealed specimens of varying grain sizes, deformed up to 2% strain.

TABLE 4.6

Values of the constants A and B in equation (4.19) for specimens of different grain sizes.

$\ell$ ( $\mu\text{m}$ )	As-annealed		2% pre-strained and annealed for 30 minutes at temperatures of			
			550°C		800°C	
	A (MPa)	B (MPa)	A (MPa)	B (MPa)	A (MPa)	B (MPa)
3.4	360.0	24.9	395.0	24.9	332.0	32.0
5.6	337.0	31.2	357.0	31.2	257.3	44.3
8.9	270.7	37.7			225.0	42.0
11.2	262.3	36.6				
21.0	232.3	40.3	240.0	40.3		
22.4	231.3	37.6			175.9	47.0

In order to determine the effect of grain size on the flow stress, the Hall-Petch relationship given by equation (4.18) was employed. Plots of  $\sigma$  versus  $\ell^{-1/2}$  are shown in figure (4.16). Using the least-square fit, the Hall-Petch parameters  $\sigma_o(\epsilon)$  and  $K(\epsilon)$  were determined at different strains. Figure (4.17) shows the variation of  $\sigma_o(\epsilon)$  and  $K(\epsilon)$  as a function of plastic strain  $\epsilon$  in the range of 0 to 2%. From the figure it can be seen that  $\sigma_o(\epsilon)$  increases linearly with strain.  $K(\epsilon)$  shows an initial increase in the micro-strain region ( $\epsilon < 0.2\%$ ), going through a peak at about 0.2% strain and then linearly decreases with strain. The slopes of the curves  $\sigma_o(\epsilon)$  and  $K(\epsilon)$  versus  $\epsilon$  are 4431 MPa and  $-3052 \text{ MPa} \cdot (\mu\text{m})^{1/2}$  respectively.

#### 4.3.1.2.2. PRE-STRAINED AND ANNEALED (AT 550°C) SPECIMENS

The 2% pre-strained specimens with different grain sizes were annealed at 550°C for 30 minutes. The annealing temperature of 550°C is sufficient (Varin and Tangri 1982, Kurzydowski et al 1985) for the delocalization of the core of EGBDs on the majority of grain boundaries to such an extent that their image is no longer visible in TEM.

Figure (4.18a) shows the stress strain curves for the specimens annealed at 550°C (solid line) and for the as-annealed specimens (broken line). From the figure it can

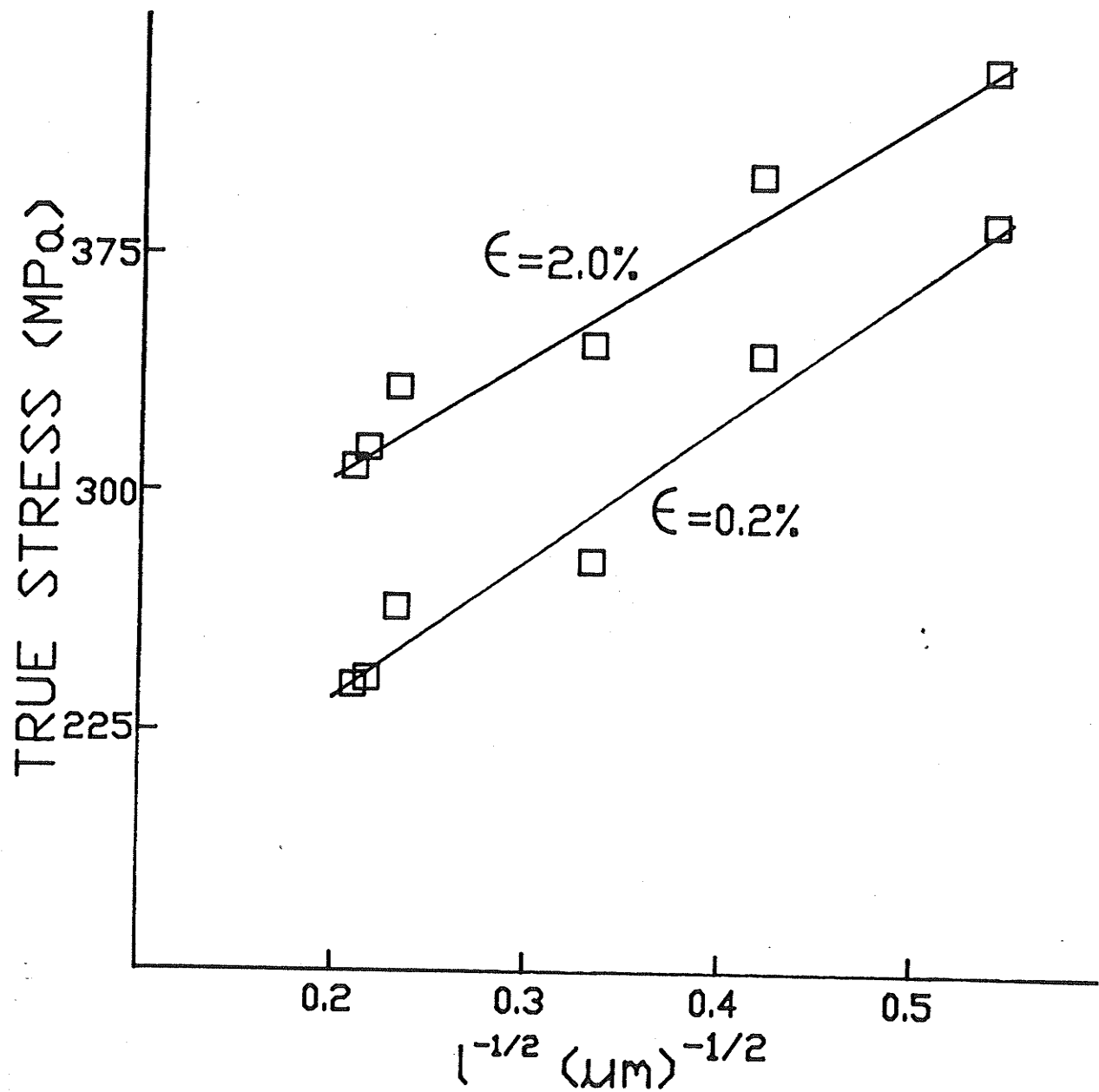
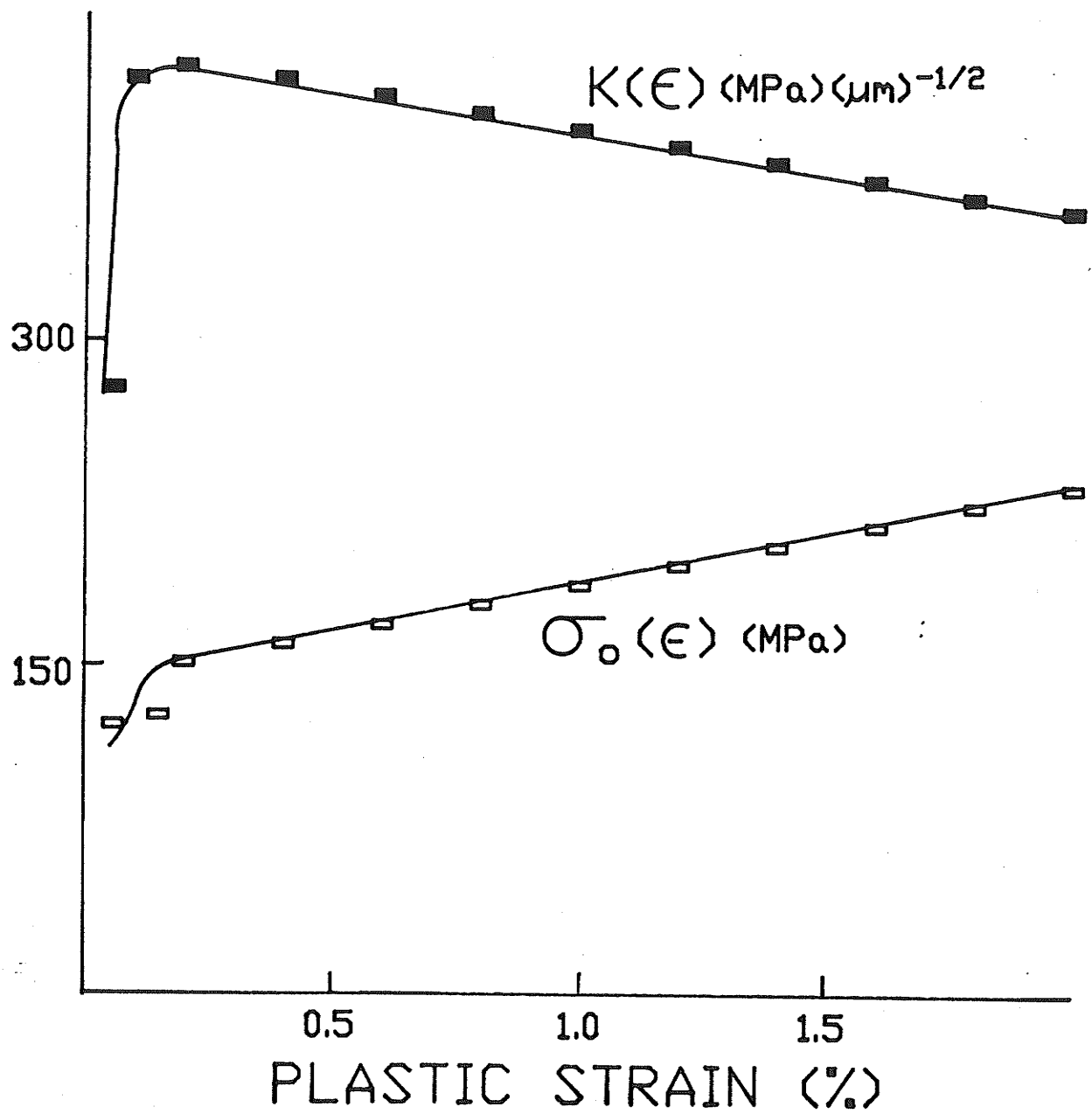
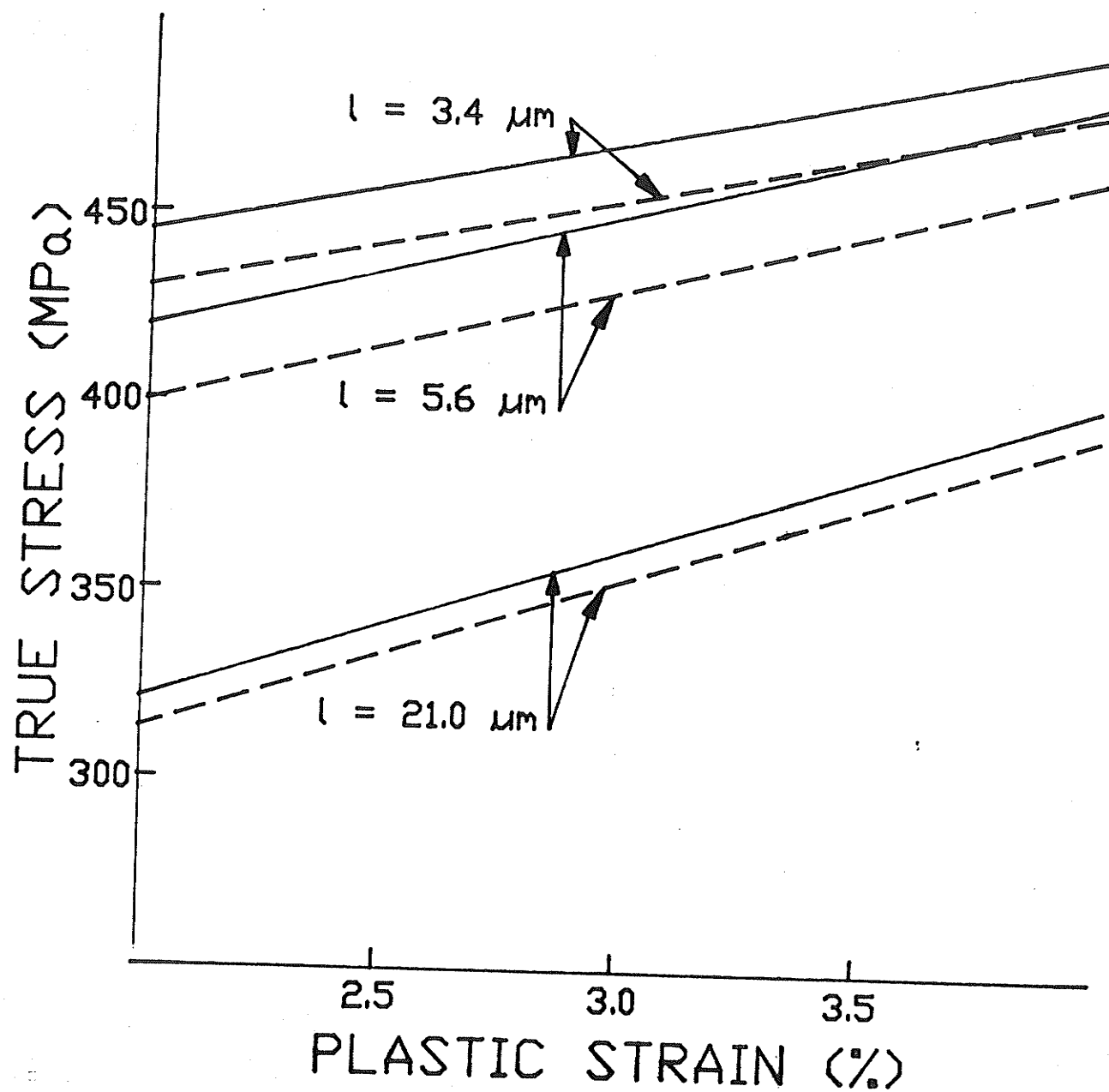


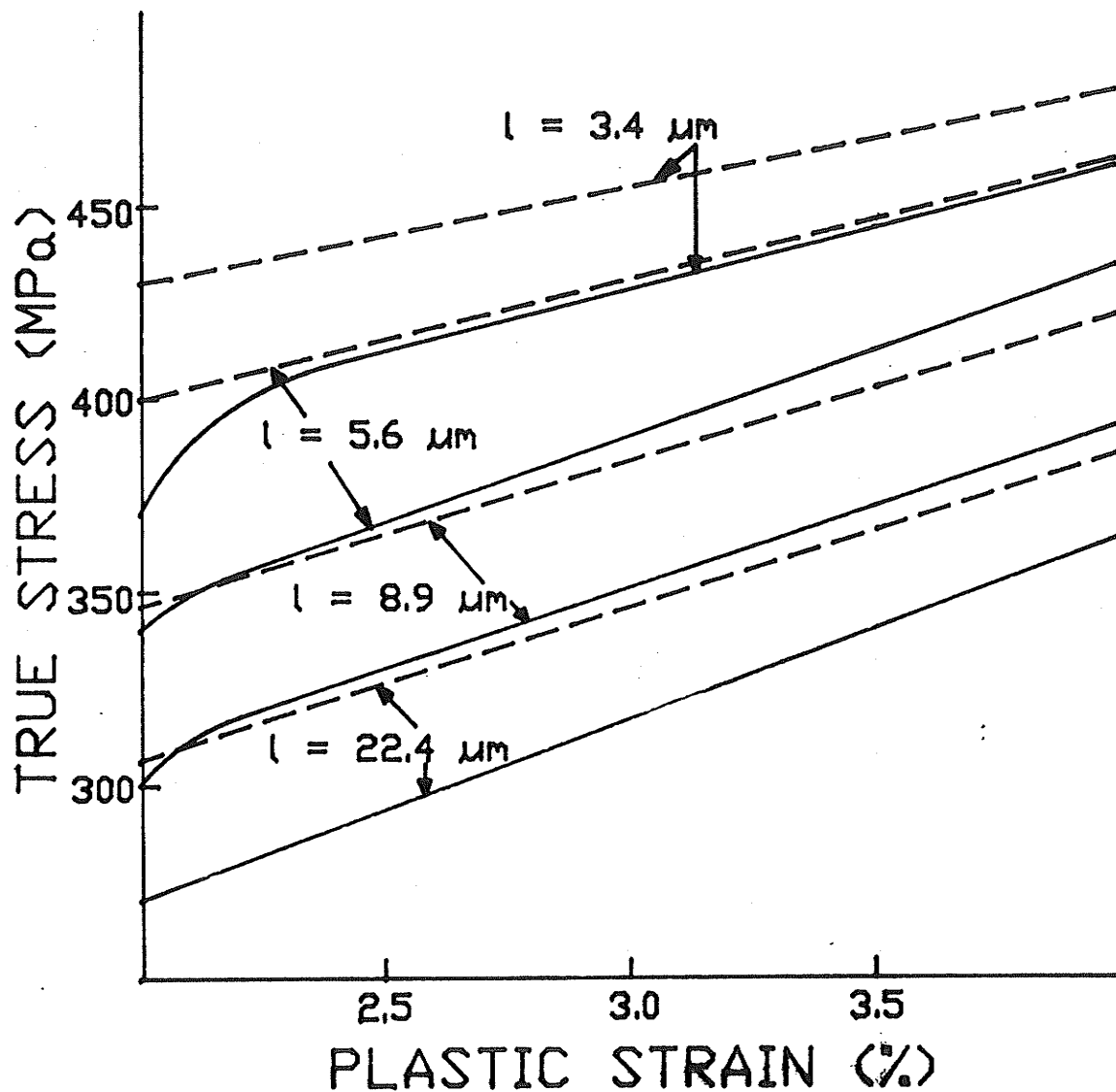
Figure 4.16: Plots of flow stress,  $\sigma(\epsilon)$  versus  $l^{-1/2}$  at different plastic strains  $\epsilon$ .



**Figure 4.17:** The variation of the Hall-Petch parameters  $\sigma_0(\epsilon)$  and  $K(\epsilon)$  with plastic strain  $\epsilon$ .



(a)



(b)

**Figure 4.18:** Stress-strain curves for the as-annealed specimens (broken line), and 2% pre-strained specimens subsequently annealed for 30 minutes (solid line) at temperatures of (a) 550°C and (b) 800°C. Note: origin for the solid line lies at 2% while for the broken line it is at 0%.



be seen that the flow stress is higher for the specimens annealed at  $550^{\circ}\text{C}$  than that for the as-annealed specimens. The difference in the flow stress is small but consistent. The flow stress difference does not have any systematic variation with grain size. The values of the constants A and B in equation (4.19) which describes the stress-strain curves are listed in Table (4.6).

#### 4.3.1.2.3. PRE-STRAINED AND ANNEALED (AT $800^{\circ}\text{C}$ ) SPECIMENS

Figure (4.18b) shows the stress-strain curves for the specimens annealed at  $800^{\circ}\text{C}$  (solid line) and for the as-annealed specimens (broken line). The stress-strain curves (solid line) for the specimens annealed at  $800^{\circ}\text{C}$  also exhibit linear hardening and therefore they can be represented by the constitutive relation given by equation (4.19). The flow stress is lower than that observed for the as-annealed specimens. The difference in the flow stress decreases with increasing strain. Annealing at  $800^{\circ}\text{C}$  results in a higher work-hardening rate than that obtained in the case of the as-annealed specimens. The variation in the work-hardening rate with grain size is similar to that observed in the as-annealed specimens, i.e., B increases with grain size. Table (4.6) gives the values of the constants A and B as a function of grain size. It can also be seen that for all the grain

sizes investigated, the constant A decreases and the work-hardening rate B increases as a result of 2% pre-strain and subsequent annealing at 800°C for 30 minutes.

#### 4.3.2. VARIATION OF $\sigma_o(\epsilon)$ WITH STRAIN

The observed linear increase in  $\sigma_o(\epsilon)$  with increasing  $\epsilon$  (figure 4.17) is in agreement with the linear increase in  $\sigma_o(\epsilon)$  observed in  $\alpha$  - brasses (figure 2.15) which like 316L stainless steel is also a low SFE material. The linear increase in  $\sigma_o(\epsilon)$  with increasing strain has been correlated (Armstrong et al 1962) with the linear stage II hardening observed in mono-crystals. The linear hardening in stage II is related to dislocation interactions in the absence of any recovery processes (e.g., cross-slip). Since no recovery processes are expected to operate in the range of strain under investigation in 316L stainless steel, the dislocation processes in the grain interior would be similar to those observed in stage II of mono-crystals. The slope  $d\tau/d\gamma$  of stage II hardening of many fcc mono-crystals has been found to be  $G/300$  (Hirsch 1975) where G is the shear modulus. Therefore, using equation (2.14), the expected slope  $\frac{d\sigma_o(\epsilon)}{d\epsilon}$  for fcc polycrystals can be expressed as:

$$\frac{d\sigma_o(\epsilon)}{d\epsilon} = m^2 \frac{d\tau}{d\gamma} = m^2 \frac{G}{300} \quad (4.20)$$

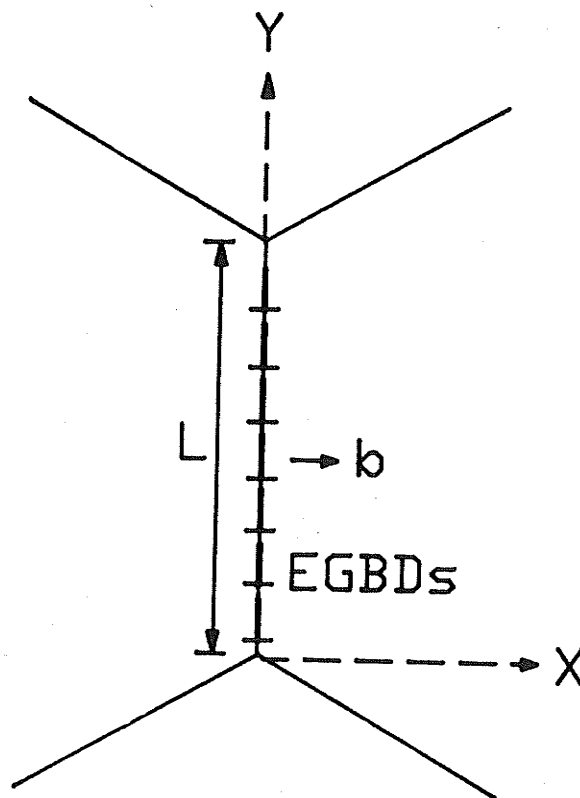
where  $m$  is the Taylor orientation factor which in fcc materials has a mean value of 3.1. Equation (4.20) gives the slope,  $\frac{d\sigma_o}{d\epsilon}$  equal to 2700 MPa which is considerably lower than the experimental value of 4431 MPa. This difference as shown in the following section, can be explained in terms of the stress field created by the EGBDs.

#### 4.3.3. THE EFFECT OF EGBDs

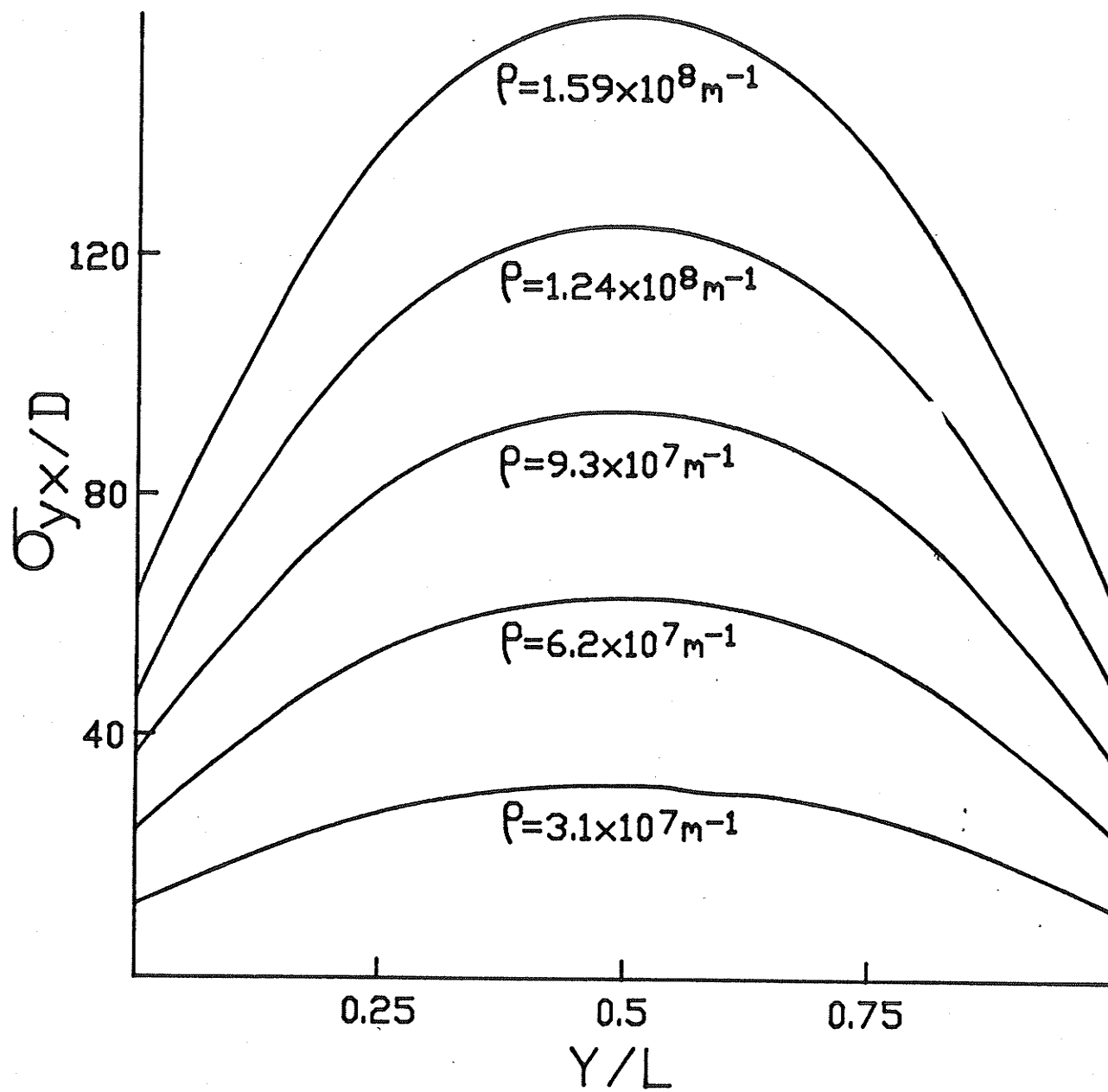
Figure (4.19a) shows schematically an array of EGBDs at a grain boundary. The stress field from such an array of dislocations is usually computed by assuming the array to be of an infinite length. In polycrystals EGBDs form an array of finite length  $L$  ( $L$  is the grain boundary length). The stress field  $\sigma_{yx}$  of such an array can be calculated by summing up the stresses from the individual dislocations. The stress field of an edge dislocation is given by the following relation (Hirth and Lothe 1982):

$$\sigma_{yx} = D \cdot x \frac{x^2 - y^2}{(x^2 + y^2)^2} \quad (4.21)$$

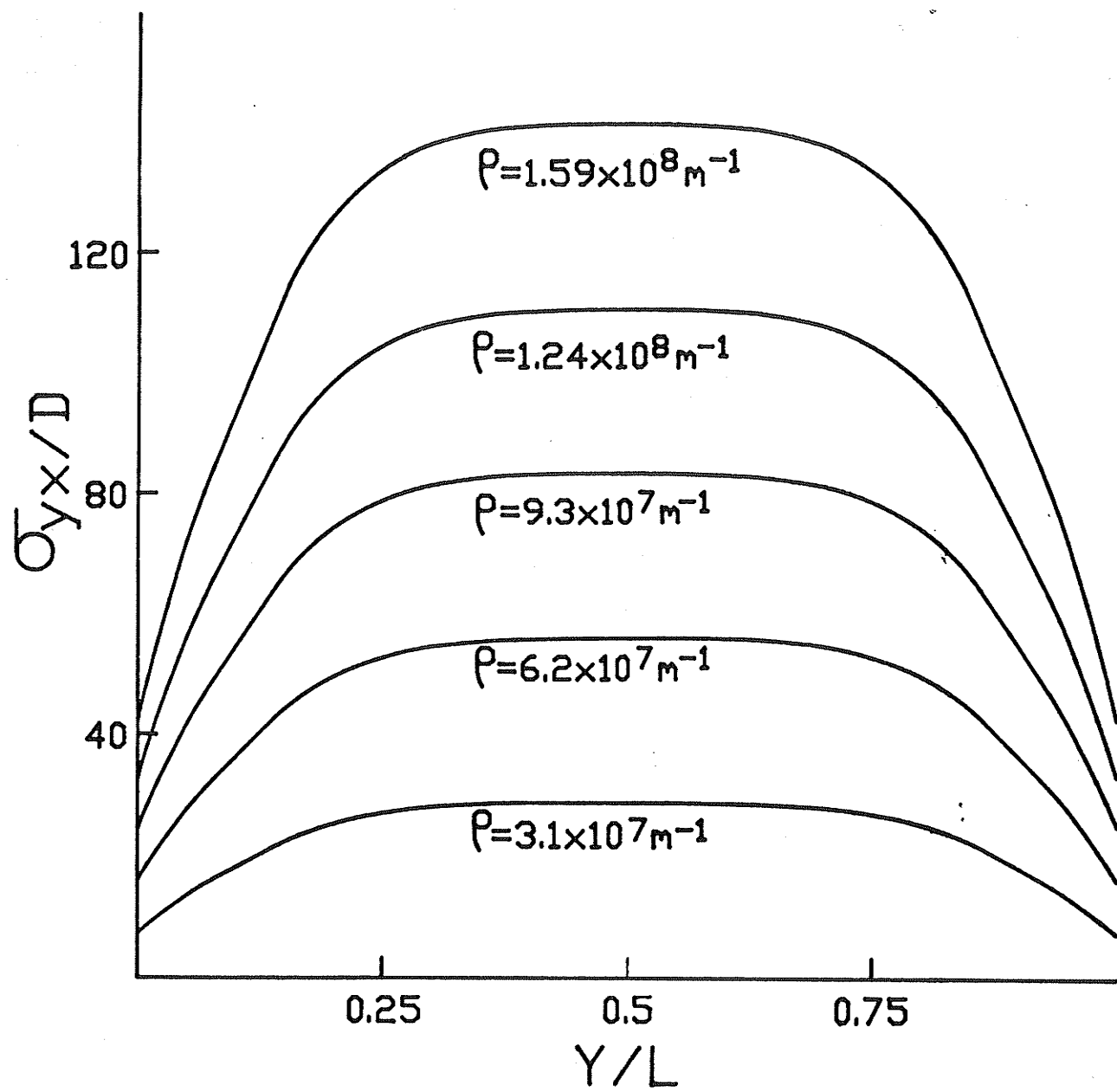
where  $D = \frac{Gb}{2\pi(1-\nu)}$ . If there are  $N$  EGBDs on a grain boundary of length  $L$  in figure (4.19a), then the total stress  $\sigma_{yx}^T$  is given by summing up equation (4.21) over  $N$  dislocations:



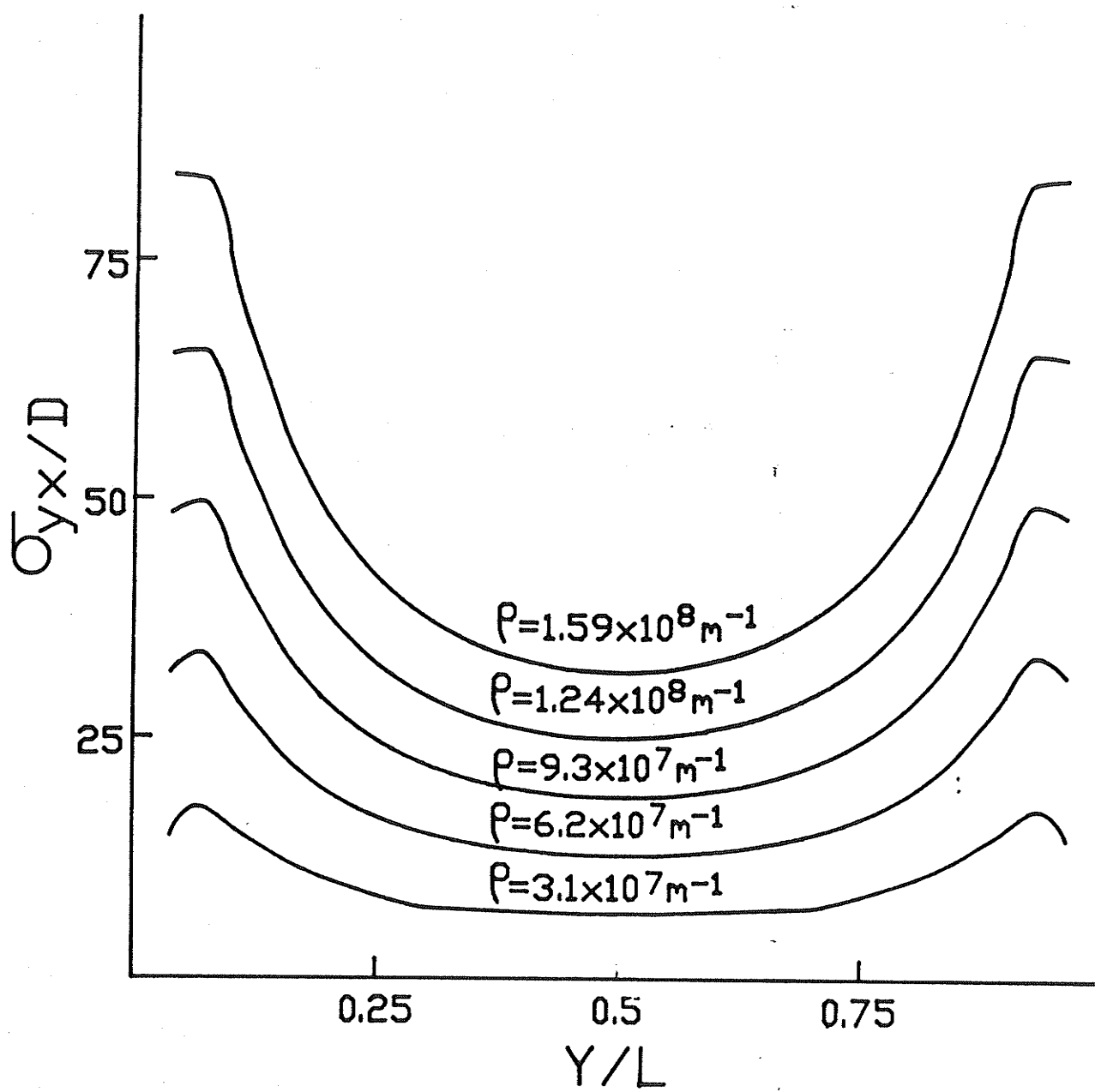
(a)



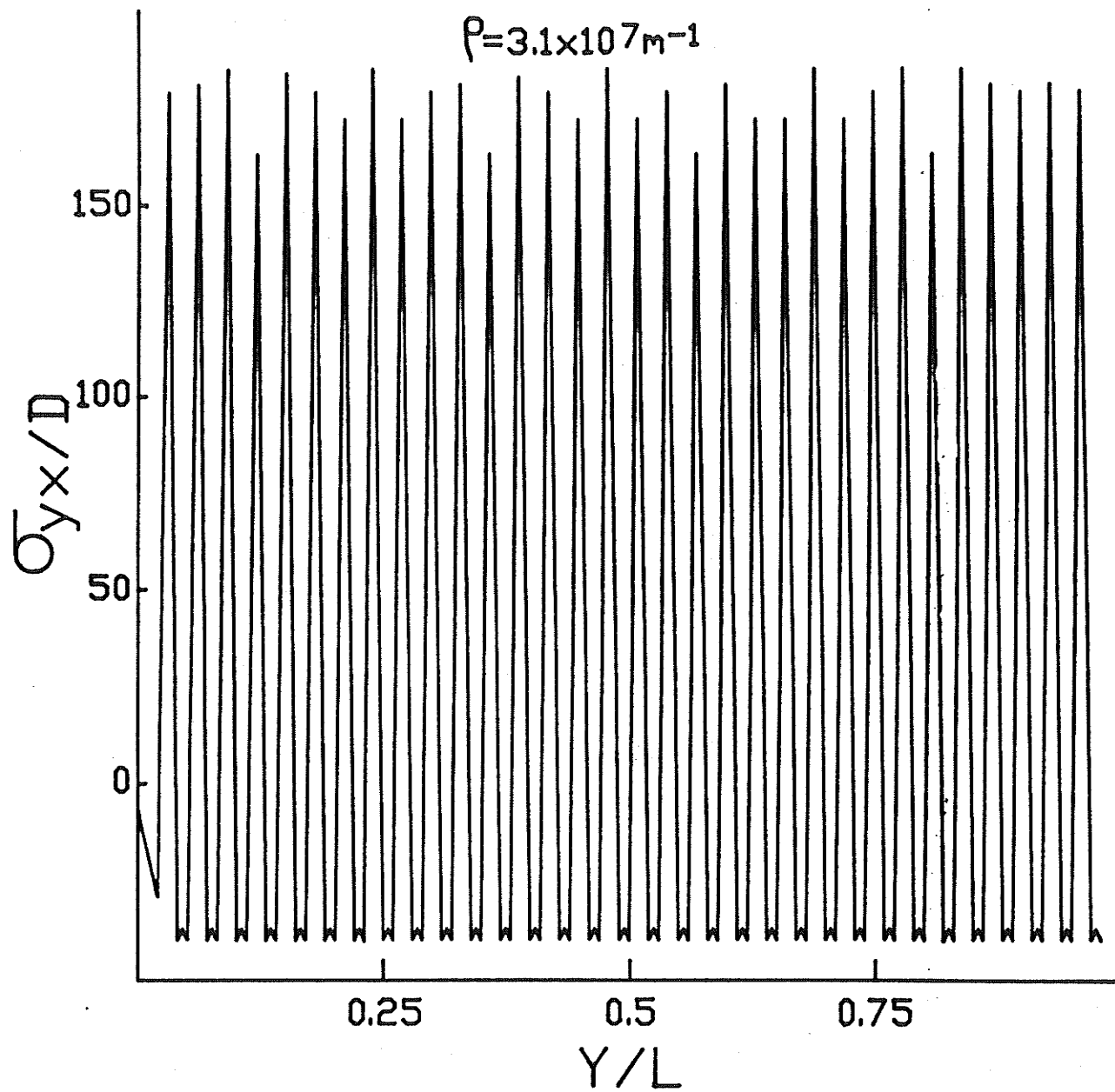
(b)



(c)

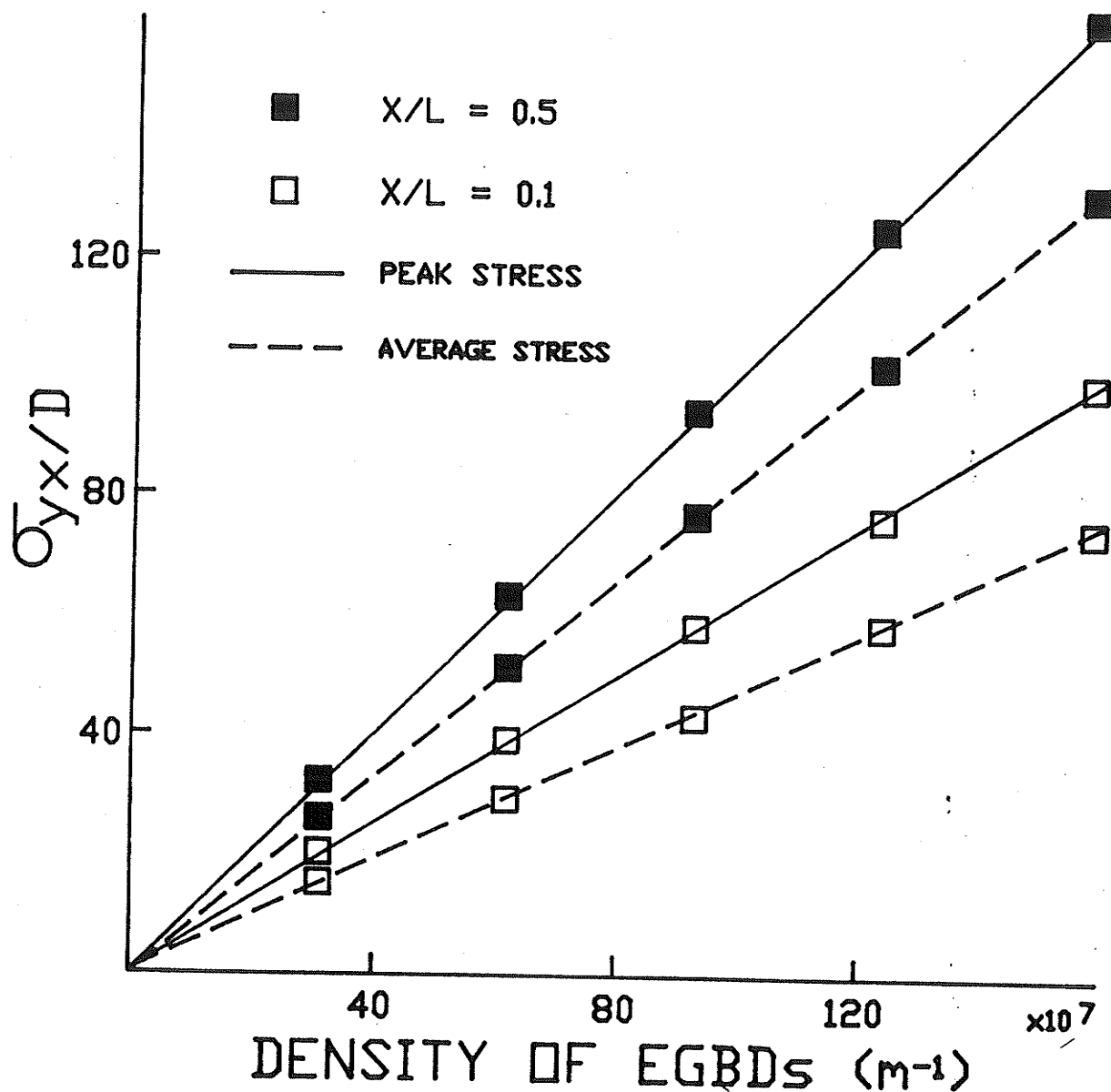


(d)



(e)





(f)

Figure 4.19: (a) A schematic of an array of EGBDs of a finite length  $L$  at a grain boundary; the variation in  $\sigma_{yx}^I$  (calculated from equation 4.22) for varying density,  $\rho$  of EGBDs at (b)  $X = 0.5L$ , (c)  $X = 0.3L$ , (d)  $X = 0.05L$ , and (e)  $X = 0.005L$  as a function of  $Y$ ; (f) the variation in the peak stress and the average stress as a function of the density of EGBDs;  $D = \frac{Gb}{2\pi(1-\nu)}$ .

$$\sigma_{yx}^T = \sum_{i=1}^N \sigma_{yx}^i = \sum_{i=1}^N D \times \frac{x^2 - (y - i \Delta y)^2}{(x^2 + (y - i \Delta y)^2)^2} \quad (4.22)$$

where  $\sigma_{yx}^i$  is the stress exerted by the  $i_{th}$  dislocation in the dislocation array of figure (2.19a), and  $\Delta y = \frac{L}{N}$ , is the average distance between dislocations. Equation (4.22) was used to compute the stress field of the array of EGBDs (shown in figure 4.19a) for various densities of EGBDs at varying distances from the grain boundary. The results of the calculations are shown in figures 4.19b, c, d, e and f.

Figures (4.19b) and (4.19c) show the nature of the long range stress field far from the grain boundary ( $X = 0.5L$  and  $0.3L$  respectively). It can be seen that the stresses are characterized by a peak stress which occurs along the centre of the grain boundary at  $Y = 0.5L$ . The peaks become broader with decreasing distance from the grain boundary up to a distance of  $0.005L$ . A detailed analysis shows that the peak stress increases linearly with increasing density of EGBDs as shown in figure (4.19f). An average stress was calculated as a function of the density of EGBDs for a given distance from the grain boundary. The results plotted in figure (4.19f) show that the average stress also increases linearly with increasing density of EGBDs.

A dislocation moving towards a grain boundary containing EGBDs has to overcome not only the friction stress of the

grain interior but also the repulsive stress created by the EGBDs. Therefore,  $\sigma_o(\epsilon)$  can be expressed as a superposition of the long range stresses  $\sigma_o^{\text{EGBDs}}(\epsilon)$  and the work-hardening in the grain interior  $\sigma_o^{\text{GI}}(\epsilon)$  (which as discussed in the previous section is related to the stage II type of linear hardening observed in mono-crystals):

$$\sigma_o(\epsilon) = \sigma_o^{\text{GI}}(\epsilon) + \sigma_o^{\text{EGBDs}}(\epsilon) \quad (4.23)$$

TEM observations (Varin and Tangri 1982 and Murr and Wang 1982) show that in the range of small strains the density of EGBDs increases linearly with strain\*. The contribution of the long range stress field to  $\sigma_o(\epsilon)$  would on an average (see figure 4.19f) increase linearly with strain. Thus, both the contributions to  $\sigma_o(\epsilon)$  increase linearly with strain and equation (4.23) predicts that  $\sigma_o(\epsilon)$  would also increase linearly with strain in the small strain regime of 0 to 2%. This is in agreement with the experimental observation shown in figure (4.17).

In the close vicinity ( $X < 0.05L$ ) of the grain boundary, the nature of the stress field is very different. It is

---

\*A simple geometrical consideration also shows that to a first approximation the density of EGBDs increases linearly with strain and is independent of grain size: if  $V_g$  is the grain volume,  $A_{gb}$  is the area of the G.B. plane, and  $\rho_m$  is the density of mobile dislocations then density of EGBDs,  $\rho_o = \rho_m \cdot V_g / A_{gb}$ ; since  $\rho_m = \epsilon / b\ell$ ,  $V_g \propto \ell^3$ , and  $A_{gb} \propto \ell^2$  gives a linear relation between density and strain:  $\rho_o \propto \epsilon / b$ .

characterized by distinct peaks as shown in figure (4.19d) and (4.19e). With decreasing distance from the grain boundary, the number of peaks increases until it becomes equal to the number of EGBDs at  $X \approx 0.005L$  (figure 4.19e). The magnitude of the peak stress is independent of the density of EGBDs for  $X < 0.005L$ . The peak stress at a given distance  $X$  is equal to the stress exerted by a single EGBD. Thus, sites of high stress concentration are created near the individual EGBDs. The implication of this observation, viz, the Hall-Petch parameter  $K(\epsilon)$  is discussed in the next section.

#### 4.3.4. VARIATION OF $K(\epsilon)$ WITH STRAIN

A decrease in  $K(\epsilon)$  with strain has been usually found to be a characteristic of high SFE materials (see section 2.3), where it is attributed to the development of substructure (e.g., cells or sub-grains). It may be pointed out that the formation of substructure implies that the initial grain size  $\ell$  can no longer be used in the Hall-Petch relationship. Therefore, the observed decrease in  $K(\epsilon)$  with strain has no physical significance in reference to equation (4.18). However, the observed decrease in  $K(\epsilon)$  in low SFE materials, as in the present case (figure 4.17) cannot be explained on the basis of substructure formation because in the absence of

recovery processes substructure is not expected to develop during room temperature deformation. The absence of substructure is confirmed by the TEM observations made in section (4.1.1.3). It is proposed that the observed decrease in  $K(\epsilon)$  with strain can be explained in terms of the influence of EGBDs on the conditions for the generation of lattice dislocations at grain boundaries.

As mentioned earlier, the EGBDs act as stress concentrators (Murr 1974,1975 and 1981, Varin et al 1987) leading to a significant decrease in the stress required to generate dislocations in the grain boundary region. It was formally shown in section 4.3.3 (figure 4.19e) that the density of the stress concentration sites is equal to the density of EGBDs. Since the density of EGBDs increases with increasing plastic strain, the density of potential sites where dislocations can be generated also increases with increasing plastic strain. Thus,  $K(\epsilon)$  which is a function of the stress required to generate dislocations would decrease with increasing plastic strain.

No attempt was made to explain the initial increase in  $K(\epsilon)$  in the micro-strain regime (figure 4.17) because the experimental data showed a large scatter in the flow stress and therefore no analysis was possible.

#### 4.3.5. GRAIN SIZE DEPENDENCE OF THE WORK-HARDENING RATE

Using the Hall-Petch relation given by equation (4.18) the work-hardening rate  $B$  in equation (4.19) can be related to the parameters  $\sigma_o(\epsilon)$  and  $K(\epsilon)$  by

$$B = \frac{d\sigma(\epsilon)}{d\epsilon} = \frac{d\sigma_o(\epsilon)}{d\epsilon} + \ell^{-1/2} \frac{dK(\epsilon)}{d\epsilon} \quad (4.24)$$

In the absence of any recovery mechanism in the range of small strains employed here,  $\sigma_o(\epsilon)$  must increase monotonically with strain as a result of dislocation accumulation in the grain interior and at grain boundaries. Thus, the term  $\left( \frac{d\sigma_o(\epsilon)}{d\epsilon} \right)$  in equation (4.24) is positive. If the parameter  $K(\epsilon)$  decreases with strain, then the term  $\left( \ell^{-1/2} \frac{dK}{d\epsilon} \right)$  in equation (4.24) is negative but its absolute value decreases with increasing grain size. Therefore, the work-hardening rate would increase with increasing grain size. This is in agreement with the observed increase in the value of parameter  $B$  with increasing grain size as shown in Table (4.6). From equation (4.24), it can be seen that the work-hardening rate  $B$  is a function of both the work-hardening in the matrix  $\left( \frac{d\sigma_o(\epsilon)}{d\epsilon} \right)$  and the change in the conditions for dislocation generation (reflected by  $\frac{dK(\epsilon)}{d\epsilon}$ ) at

grain boundaries. The grain size dependent term  $\left( \ell^{-1/2} \frac{dK}{d\epsilon} \right)$  will become small for large grain sizes and the work-hardening rate will be essentially determined by the accumulation of dislocations inside the grains.

#### 4.3.6. EFFECT OF PRE-STRAIN AND ANNEALING AT 550°C

The results of tensile tests on specimens which were pre-strained to 2% and subsequently annealed at 550°C for 30 minutes showed a small increase in the flow stress as compared with the as-annealed specimens (see figure 4.18a). In-situ TEM observations (Varin and Tangri 1982 and Kurzydowski et al 1985) show that annealing at 550°C results in the spreading and the eventual disappearance of the image contrast of EGBDs on the majority of grain boundaries in austenitic stainless steel. However, it was shown in sections (4.1) and (4.2) that the non-visibility of EGBDs in the TEM image does not imply their complete annihilation. Computations of the stress field of these partially spread out EGBDs (calculations are carried out in the same manner as in section 4.3.3) show that the magnitude of the long range stresses is unaffected by the spreading process. TEM observations made in section 4.1 also indicate that as a result of the above heat treatment there is no change in the density of dislocations in the vicinity of grain boundaries

or in the grain interior. As such, no change in the flow stress is to be expected as a result of annealing at 550°C for 30 minutes. Thus, it is concluded that the observed increase in the flow stress is the result of strain ageing which is known to occur in 316L stainless steel (Kashyap, McTaggart and Tangri 1988).

#### 4.3.7. EFFECT OF PRE-STRAIN AND ANNEALING AT 800°C

Annealing at 800°C for 30 minutes results in the decrease of flow stress as compared with the as-annealed specimens (see figure 4.18b). This 800°C anneal also results in a decrease in the value of the constant A and in an increase in the value of the constant B (i.e., the work-hardening rate) as shown in Table (4.6). It can also be seen that the decrease in flow stress is larger for the fine grain size specimens than for the coarse grain size specimens. This grain size dependence can be rationalized in terms of the changes in the microstructure and their affect on the Hall-Petch parameters  $\sigma_0(\epsilon)$  and  $K(\epsilon)$ .

Annealing of pre-strained specimens at 800°C results in the annihilation of EGBDs accompanied with a decrease in the density of dislocations in the grain boundary region (section 4.1). It was proposed in the earlier sections that the decrease in the density of dislocations occurs as a result of



their incorporation and subsequent annihilation in migrating grain boundaries during annealing. The kinetics of annihilation of EGBDs can be estimated by equations (4.16) and (4.17).

The percentage of EGBDs annihilated (denoted by  $\Delta\rho/\rho_0$ , where  $\Delta\rho$  is the density of EGBDs annihilated and  $\rho_0$  is the initial density of EGBDs) at a given annealing temperature and time was calculated from equation (4.17) as a function of grain size. The results of the calculations are listed in Table (4.7). It may be noted that the extent of annihilation (i.e., density of EGBDs annihilated) decreases with increasing grain size.

The annihilation of EGBDs results in the decrease in the long range stress field and also a decrease in the stress concentration in the vicinity of grain boundaries. This would result in a decrease in  $\sigma_0(\epsilon)$  (which is a function of both the density of EGBDs and the density of dislocations inside the grains) and an increase in  $K(\epsilon)$  (which is a function of the stress required to generate dislocations at grain boundaries). The decrease in  $\sigma_0(\epsilon)$  being larger than the increase in  $K(\epsilon)$  leads to an overall decrease in the flow stress.

In view of the above we can now compare the work-hardening behaviour of fine and coarse grained specimens annealed at 800°C. In the case of fine grained specimens

TABLE 4.7

Estimated percentage annihilation of EGBDs  $\left( \frac{\Delta\rho}{\rho_o} \right)$  as a function grain size ( $\ell$ ) as a result of annealing at 2% pre-strained specimens at 800°C for 30 minutes.

$\ell$ ( $\mu\text{m}$ )	$\frac{\Delta\rho}{\rho_o}$ (%)
3.4	100.0
5.6	88.0
8.9	51.0
22.4	46.0

(grain size of  $3.4\mu\text{m}$ ) annealing at  $800^{\circ}\text{C}$  leads to a complete annihilation of dislocations at and in the vicinity of grain boundaries as shown in the TEM micrographs of figure (4.10). As a consequence the value of  $\sigma_0(\epsilon)$  decreases and the value of  $K(\epsilon)$  increases to that observed in the as-annealed specimens. In the coarse grained material, however, annealing at  $800^{\circ}\text{C}$  results only in an incomplete annihilation of dislocations at and in the vicinity of grain boundaries. For example, in grain sizes beyond  $8.9\mu\text{m}$  the maximum annihilation of dislocations is approximately 50% (see Table 4.7). As a result only small changes in the values of  $\sigma_0(\epsilon)$  and  $K(\epsilon)$  occur leading to a smaller change in the flow stress (see figure 4.18b and Table 4.6).

In both the fine and coarse grained specimens, annealing at  $800^{\circ}\text{C}$  results in an increased work-hardening rate  $B$  (Table 4.6) as compared with the as-annealed specimens. This higher work-hardening rate is attributed to the fact that the pre-strained and annealed specimens contain a higher initial density of dislocations in the grain interior than the as-annealed specimens. Thus further straining leads to higher work-hardening rate in the grain interior.

## CHAPTER 5

### CONCLUSIONS

The following important conclusions can be drawn from this study which relate the changes in the structure of grain boundaries as a result of pre-straining and annealing to the room temperature deformation behavior of 316L austenitic stainless steel.

1. Significant structural changes take place at and in the vicinity of grain boundaries. TEM observations show that the annihilation of dislocations occurs at and in the vicinity of grain boundaries as a result of annealing of 2% pre-strained specimens of 316L stainless steel. The observations also indicate no significant changes in the grain interior.
2. The recovery of yield stress as a result of annealing of pre-strained specimens is associated not only with the annihilation of dislocations in the grain boundaries and its immediate environs but is also associated with an increase in the grain boundary length, and a decrease in the standard deviation of dihedral angles. In other words the recovery of yield stress and the annihilation of dislocations are accompanied by grain boundary migration.
3. The observed drop in yield stress after annealing of

pre-strained specimens is attributed to the effect of the transformation of non-equilibrium grain boundaries to equilibrium grain boundaries and the annihilation of dislocations in their vicinity.

4. The theoretical model developed to describe the the kinetics of the transformation of non-equilibrium grain boundaries to their equilibrium state involves the annihilation of extrinsic grain boundary dislocations (EGBDs) via climb along the grain boundary plane.
5. The model predicts that the rate of annihilation of EGBDs is dependent on the annealing temperature, grain size and the density of EGBDs. The rate of annihilation is higher at higher temperatures, smaller grain sizes and higher instantaneous density of EGBDs.
6. The experimental variation of yield stress with annealing time and temperature is in agreement with the predicted variation of the density of EGBDs in 316L stainless steel.
7. The onset of the changes in the geometry of the grain boundary network correspond to the onset of the annihilation of EGBDs as predicted by the model.
8. The Hall-Petch analysis used on 316L stainless steel in the grain size range of  $3.4\mu\text{m}$  to  $22.4\mu\text{m}$  shows

that in the range of small strains (0 to 5%) the Hall-Petch parameter  $\sigma_0(\epsilon)$  increases linearly with strain and the parameter  $K(\epsilon)$  decreases linearly with strain.

9. The linear increase in  $\sigma_0(\epsilon)$  with strain has been associated with the work-hardening processes in the grain interior and the long range stress field of EGBDs.
10. The decrease in  $K(\epsilon)$  with strain occurs as a result of the increased stress concentration created by the increase in the density of EGBDs.
11. The drop in the flow stress as a result of annealing at 800°C of pre-strained specimens has been related to the annihilation of dislocations at and in the vicinity of grain boundaries. The rate of annihilation of dislocations decreases with increasing grain size and therefore the extent of the drop in flow stress also decreases with increasing grain size.

## REFERENCES

- Abrahamson, E.P., 1970, in *Ultrafine grain metals*, eds. Bruke, J.J. and Weiss, V., Syracuse, Syracuse University Press, p. 71.
- Armstrong, R., 1983, in *Yield, Flow and Fracture of Polycrystals*, ed. Baker, T.N., Applied Science Pub., London and New York, p. 1.
- Armstrong R., Codd, I., Douthwaite, R.M. and Petch, N.J., 1962, *Phil. Mag.*, 7, p. 45.
- Ashby, M.F., 1970, *Phil. Mag.*, 21, p. 399.
- Ashby, M.F., 1971, in *Grain Boundaries and Interfaces, Proceedings of the International Conference on the Structure and Properties of Grain Boundaries and Interfaces*, eds. Chaudhari, P. and Matthews, J.W., Yorktown Heights, New York, p. 498.
- Balluffi, R.W. (ed.), 1980, *Materials Science Seminar on Grain Boundary Structure and Kinetics*, Milwaukee, Wisconsin, Sept. 15 - 16, 1979, American Society of Metals, Metals Park, Ohio.
- Balluffi, R.W., Komen, Y. and Schober, T., 1972, *Surface Sci.*, 31, p. 68.
- Balluffi, R.W. and Schober, T., 1972, *Scripta Metall.*, 6, p. 697.
- Bishop, G. and Chalmers, B., 1968, *Scripta Metall.*, 2, p. 193.
- Bollmann, W., 1967, *Phil. Mag.*, 16, p. 363 and 383.
- Bollmann, W. (ed.), 1970, *Crystal Defects and Crystal Interfaces*, Springer, Berlin.
- Bollmann, W., Michaut, B. and Sanifort, G., 1972, *Phys. Status Sol. (a)*, 13, p. 637.
- Bollmann, W. and Perry, A.J., 1969, *Phil. Mag.*, 20, p. 33.
- Boyer, H.E. and Gall, T.L. (eds.), 1985, *Metals Handbook, Desk Edition*, ASM, Metals Park, Ohio, p. 2-16 and 15-3.

- Bragg, W.L., 1940, *Proc. Phys. Soc.*, London, 52, p. 54.
- Burgers, J.M., 1940, *Proc. Phys. Soc.*, London, 52, p. 23.
- Chadwick, G.A. and Smith, D.A. (eds.), 1976, *Grain Boundary Structure and Properties*, Academic Press, New York.
- Chalmers, B. and Gleiter, H., 1971, *Phil. Mag.*, 21, p. 1541.
- Chaudhari, P. and Matthews, J.W. (eds.), 1972, *Surface Sci.*, 31.
- Clark, W.A.T. and Smith, D.A., 1979, *Journal Mat. Sci.*, 14, p. 776.
- Conrad, H., 1963, in *Electron Microscopy and Strength of Crystals*, eds. Thomas, G. and Washburn, J., Interscience, New York, p. 299.
- Conrad, H., Feuerstein, S. and Rice, L., 1967, *Mater. Sci. Eng.*, 2, p. 157.
- Cottrell, A.H., 1958, *Trans. TMS-AIME*, 212, p. 192.
- Darby, T.P., Schindler, R. and Balluffi, R.W., 1978, *Phil. Mag.*, 37, p. 245.
- Frank, F.C., 1950, in *Proc. Symp. on Plastic Deformation of Crystalline Solids*, Carnegie-Mellon University, Pittsburgh, PA, May 19 - 20, U.S. Department of Commerce, Washington DC, p. 150.
- Fujita, H. and Tabata, T., 1973, *Acta Metall.*, 21, p. 353.
- Gleiter, H., 1977, *Korngrenzzen in metallischen Workstoffen*, Gebrüder, Bornträger, Berlin, p. 18.
- Gleiter, H., 1982, *Mat. sci. Eng.*, 52, p. 91.
- Gleiter, H. and Chalmers, B., 1971, *Prog. Mat. Sci.*, 16, p. 1.
- Grabski, M.W., 1982, in *Heterogeneites de deformation et endommagement*, Colloque Franco - Polonais, Orsay.
- Grabski, M.W. and Korski, R., 1970, *Phil. Mag. A*, 22, p. 707.
- Grabski, M.W., Valiev, R.Z., Wyrzykowski, J.W. and Lojowski, W., 1981, *Res Mechanica Letters*, 1, p. 489.



- Grange, R.A., 1966, *ASM Trans. Quart.*, 59, p. 26.
- Hall, E.O., 1951, *Proc. Phys. Soc.*, 864, p. 747.
- Hansen N., 1983, in *Yield, Flow and Fracture of Polycrystals*, ed. Baker, T.N., Applied Science Pub., London and New York, p. 311.
- Hansen, N. and Bay, B, 1982, in *The International Conference on the Strength of Metals and Alloys*, ed. Gifkin, R.C., Pergamon Press, Oxford, p. 401.
- Hansen N. and Ralph, B., 1982, *Acta Metall.*, 30, p. 411.
- Hasson, G.C. and Goux. C., 1971, *Scripta Metall.*, 5, p. 889.
- Hirsch, P.B., 1975, in *The Physics of Metals*, ed. Hirsch, P.B., 2, p. 189.
- Hirsch, P.B., Howie, A., Nicholson, R.B., Pashley, D.W. and Whelan, M.J., 1977, in *Electron Microscopy of Thin Crystals*, Robert E. Krieger Pub. Co., Florida, p. 485.
- Hirth, J.P. and Lothe, J., 1982, *Theory of Dislocations*, Second Edition, Wiley-Interscience, p. 76, 79, and 783.
- Ishida, Y., Hasegawa, T. and Nagata, F., 1968, *Trans. Japan Inst. Metals*, 9 (suppl.), p. 504.
- Johannesson, T. and Tholen, A., 1972, *Metal Sci.*, 6, 189.
- Johnson, W.C. and Blakely, J.M. (eds.), 1979, in *Interfacial Segregation*, American Society of Metals, Metals Park, Ohio.
- Kashyap, B.P., McTaggart, K. and Tangri, K., 1988, *Phil. Mag. A.*, 57, p. 97.
- Kocks, U.F., 1970, *Metall. Trans.*, 1, p. 421.
- Kronberg, M.L. and Wilson, F.H., 1949, *Trans. Metall. Soc. AIME*, 185, p. 501.
- Kurzydowski, K.J., Wyrzykowski, J., Pakiela, Z. and Grabski, M.W., 1985, *Mat. Sci. Eng.*, 72, p. 213,
- Lasalmonie, A. and Strudel, J.L., 1986, *Journal Mat. Sci.*, 21, p. 1837.
- Li, J.C.M., 1961, *Journal Appl. Phys.*, 32, p. 525.

- Li, J.C.M., 1963, *Trans. Metall. Soc. AIME*, 227, p. 239.
- Lloyd, D.J., 1980, *Metal Sci.*, p. 193.
- Lojkowski, W. and Grabski, M.W., 1979, *Scripta Metall.*, 13, p. 511.
- Lojkowski, W. and Grabski, M.W., 1981, in *Deformation of Polycrystals: Mechanisms and Microstructures*, Second Riso International Symposium on Metallurgy and Materials Science, eds. Hansen, N., Horsewell, A., Leffers, T. and Lilholt, H., Riso National Laboratory, Roskilde, p. 329.
- Ludwik, P., 1909, *Elemente der Technologischen Meckanik*, Verlag von Julius Springer, Berlin, p. 32.
- Malis, T. and Tangri, K., 1979, *Acta Metall.*, 27, p. 25.
- Meakin, J.D. and Petch, N.J., 1974, *Phil. Mag.*, 29, p. 1149.
- Mecking, H., 1981, in *Deformation of Polycrystals: Mechanisms and Microstructures*, Second Riso International Symposium on Metallurgy and Materials Science, eds. Hansen, N., Horsewell, A., Leffers, T. and Lilholt, H., Riso National Laboratory, Roskilde, p. 73.
- Miyazaki, S., Shibata, K. and Fujita, H., 1979, *Acta Metall.*, 27, p. 855.
- Mori, T. and Tangri, K., 1979, *Metall. Trans. A.*, 10, p. 773.
- Morrison, W.B., 1966, *ASM Trans. Quart.*, 59, p. 84.
- Murr, L.E., 1974, *Appl. Phys. Letters*, 24, p. 533.
- Murr, L.E., 1975, *Metall. Trans. A*, 6, p. 505.
- Murr, L.E., 1981, *Mat. Sci. Eng.*, 51, p. 71.
- Murr, L.E. and Wang, S.H., 1982, *Res. Mechanica*, 4, p. 237.
- Petch, N.J., 1953, *Journal Iron Steel Inst.*, 174, p. 25.
- Philips, W.L. and Armstrong, R.W., 1972, *Metall. Trans.*, 3, p. 2571.
- Pond, R.C. and Smith, D.A., 1977, *Phil. Mag.*, 36, p. 353.
- Pumphrey, P., 1972, *Scripta Metall.*, 6, p. 107.

- Pumphrey, P., 1976, in *Grain Boundary Structure and Properties*, eds. Chadwick, G.A. and Smith, D.A., Academic Press, London/New York, p. 139.
- Pumphrey, P. and Gleiter, H., 1974, *Phil. Mag.*, 30, p. 593.
- Pumphrey, P. and Gleiter, H., 1975, *Phil. Mag.*, 32, p. 881.
- Ralph, B., Howell, P.R. and Page, T.F., 1977, *Phys. status sol. (b)*, 55, p. 641.
- Read, W.T. and Shockley, W., 1950, *Phys. Rev.*, 78, p. 275.
- Schober, T. and Balluffi, R.W., 1971, *Phys. Status Sol. (b)*, 44, p. 115.
- Shewmon, P.G., 1963, *Diffusion in Solids*, McGraw-Hill Book Co., p. 6.
- Singh, R.N. and Tangri, K., 1970, *Metall. Trans. A*, 1, p. 3151.
- Smith, C.S., 1948, *Trans. Metall. Soc, AIME*, 175, p. 15.
- Smith, A.F. and Gibbs, G.B., 1969, *Metal Sci.*, 3, p. 93.
- Smith, D.A. and King, A.H., 1981, *Phil. Mag. A.*, 44, p. 333.
- Speigel, M.R., 1968, *Mathematical Handbook of Formulas and Tables*, Schaum's Outline Series, McGraw-Hill, p. 72 and 100.
- Speigel, M.R., 1975, *Schaum's Outline of Theory and Problems of Statistics*, Schaum's Outline Series, McGraw-Hill, p. 211.
- Stephenson, J.M., 1979, *Sheet Metal Industries*, 56 (January), p. 45-46, 49-50 and 57.
- Taylor, G.I., 1934, *Proc. Royal Soc. London, Ser. A*, 145, p. 388.
- Thomas, G., 1963, *Acta Metall.*, 11, p. 1369.
- Thompson, A.W., 1975, *Acta Metall.*, 22, p. 1337.
- Thompson, A.W., 1977, in *Work Hardening in Tension and Fatigue*, ed. Thompson, A.W., Metall. Soc, AIME, Cleveland, Ohio, p. 89.
- Thompson, A.W. and Baskes, M.J., 1973, *Phil. Mag.*, 28, p.301.

- Thompson, A.W., Baskes, M.J. and Flanagan, W.F., 1973, *Acta Metall.*, 21, p. 1973.
- Valiev, R.Z., Gertsman, V.Yu and Kaibyshev, O.A., 1980, *Phys. Status Sol. (a)*, 61, p. K95.
- Valiev, R.Z., Gertsman, V.Yu and Kaibyshev, O.A., 1986, *Phys. Status Sol. (a)*, 97, p. 11.
- Varin, R.A., 1979, *phys. status sol. (a)*, 52, p. 347.
- Varin, R.A., 1982, *Z. Metallkde*, 73, p. 654.
- Varin, R.A. and Kurzydowski, K.J., 1983, *Z. Metallkde*, 74, p. 177.
- Varin, R.A., Kurzydowski, K.J. and Tangri, K., 1987, *Mat. Sci. Eng.*, 85, p. 115.
- Varin, R.A., Lojkowski, W. and Valiev, R.Z., 1981, *Scripta Metall.*, 15, p. 795.
- Varin, R.A. and Tangri, K., 1980, *Scripta Metall.*, 14, p. 337.
- Varin, R.A. and Tangri, K., 1981, *Metall. Trans A*, 12, p. 1859.
- Varin, R.A. and Tangri, K., 1982, *Z. Metallkde*, 73, p. 144.
- Warrington, D.H. and Bollmann, W., 1972, *Phil. Mag.*, 25, p. 1195.
- Weast, R.C., 1972, *CRC Handbook of Chemistry and Physics*, The Chemical Rubber Co., Cleveland, Ohio, p. F-196.
- Weins, H., Chalmers, B., Gleiter, H. and Ashby, M.F., 1969, *Scripta Metall.*, 3, p. 601.

## APPENDIX A

### IMPLEMENTATION OF METALLOGRAPHIC TECHNIQUES ON AN IMAGE ANALYSIS SYSTEM

The computer program developed for the measurement of intercept lengths is described schematically by the flow chart given in figure (A.1). The technique involves the generation of an image of a grid of parallel lines which is superimposed in three different orientations  $120^{\circ}$  apart on the image of grain boundaries. The individual intercepts are obtained by logical combinations of the image of grain boundaries with the image of the grid (see figure A.2). The intercepts are then measured by counting the number of pixels on each intercept. However, such a procedure can lead to large errors if the specimen image consists of polishing/etching artifacts (e.g., etch pits) within the grains. In the case of fine grain size specimens, the intercepts generated will be very small in size. Since the individual pixels on each intercept have a finite size, smaller the intercept larger would be the error in estimating its length.

The polishing/etching artifacts can be eliminated by a suitable image processing procedure. For example, the artifacts visible in the image of figure (A.3a) have been completely removed, as can be seen in figure (A.3b). The

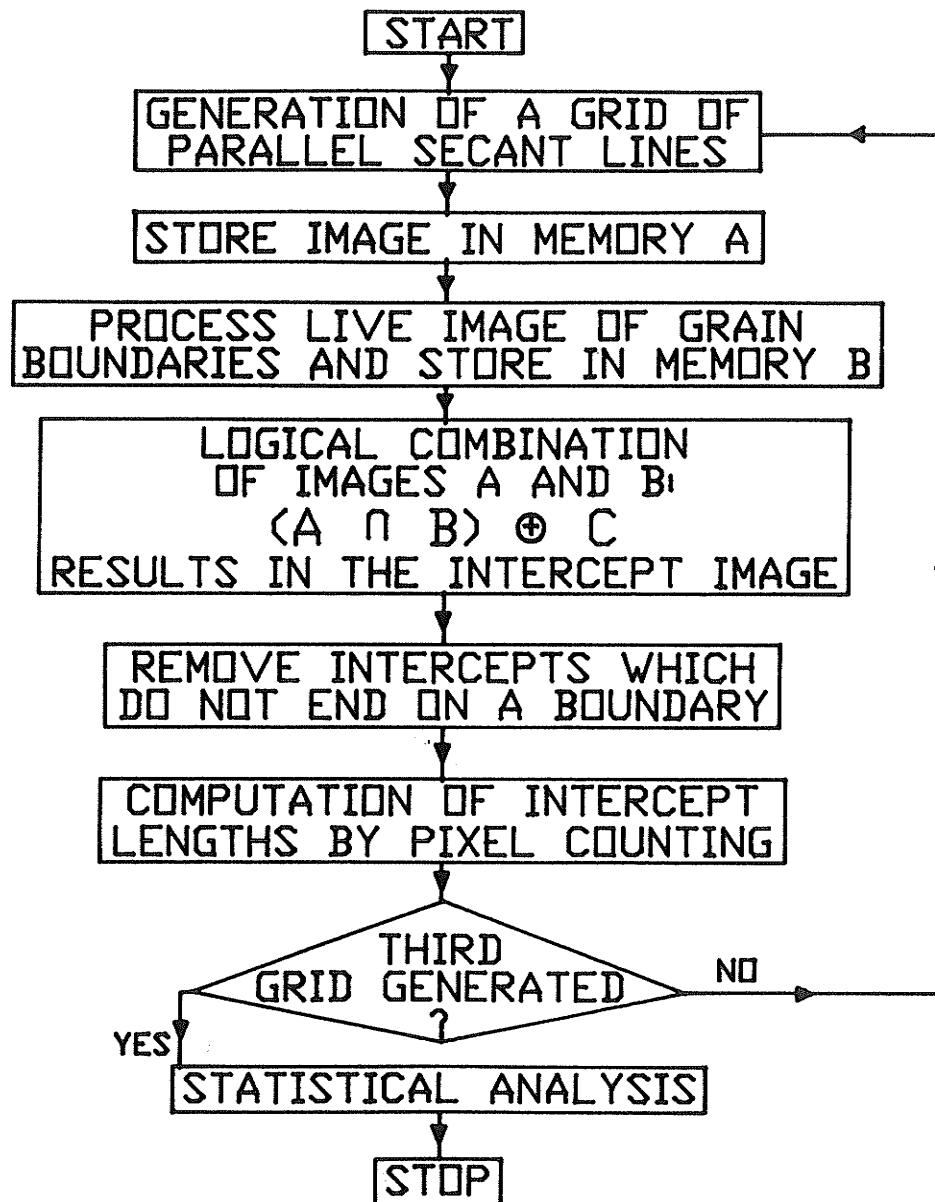
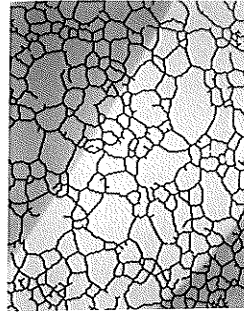
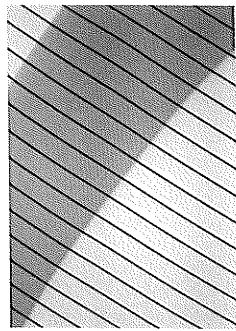


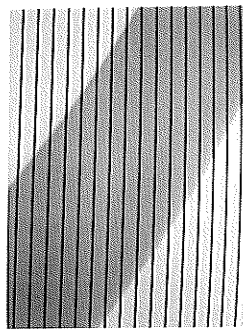
Figure A.1: Flow chart of the program developed for intercept length measurements.



(a)



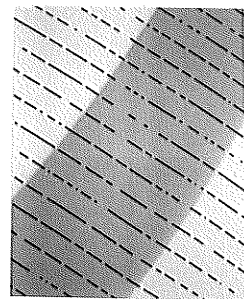
(b)



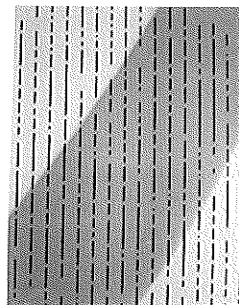
(c)



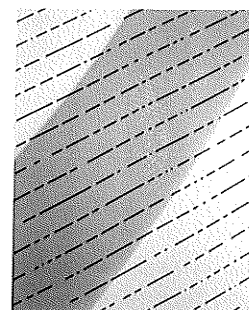
(d)



(e)

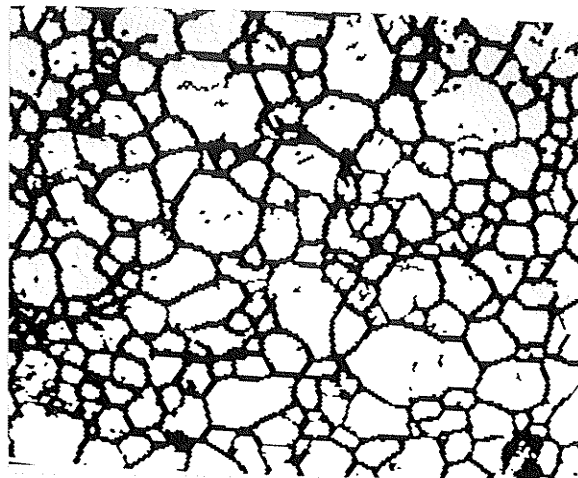


(f)

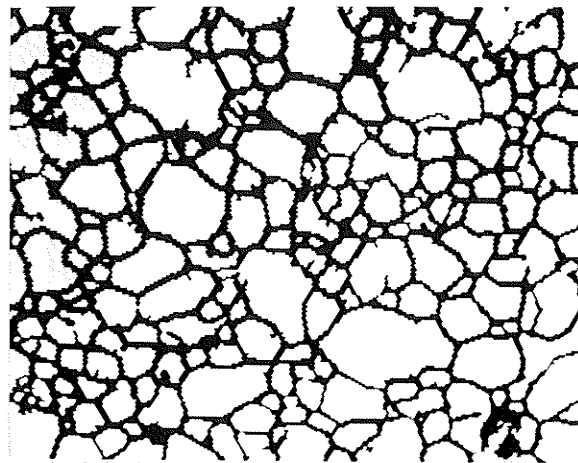


(g)

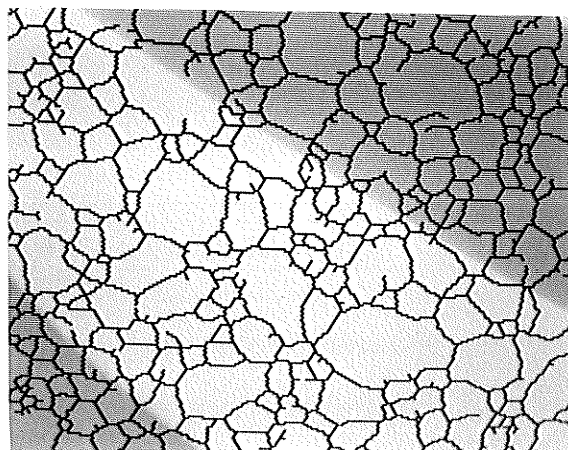
Figure A.2: The logical combinations of the grain boundary image shown in (a) with the images of the grid of parallel lines in three different orientations  $120^\circ$  apart, shown in (b), (c) and (d) produce the images of the individual intercepts shown in (e), (f) and (g) respectively.



(a)



(b)



(c)

Figure A.3: Grain boundary image: (a) consisting of polishing/etching artifacts, (b) the artifacts have been removed after image processing, and (c) thick grain boundaries have been thinned.



measurement error introduced in the case of fine grain size specimens can be reduced by choosing a higher magnification. However, too high a magnification results in a diffused contrast (for example, broadening of grain boundaries) which can again lead to a decrease in the precision of measurements. The program minimises this error by employing a thinning procedure which thins thick grain boundaries as shown in figure (A.3c). Further precision in the measurements was obtained by eliminating the intercepts which do not end on a grain boundary. The program thus developed produces results with a high degree of reproducibility.

Figure (A.4) illustrates the program developed for the measurements of dihedral angles, grain boundary length and grain boundary curvature. This program requires operator interaction for determining the positions of the triple points on an image of grain boundaries displayed on the screen. The selection of the curved grain boundaries is also dependent on operator judgment. The details of the measurement procedure of the above metallographic parameters have been described earlier (section 3.4, figure 3.4). Since this program requires operator judgment, the precision of the measurements depends on operator bias. However, the program allows for correction of the selected positions of the triple points. Since a large number of measurements can be made easily, a high measurement precision can be obtained.

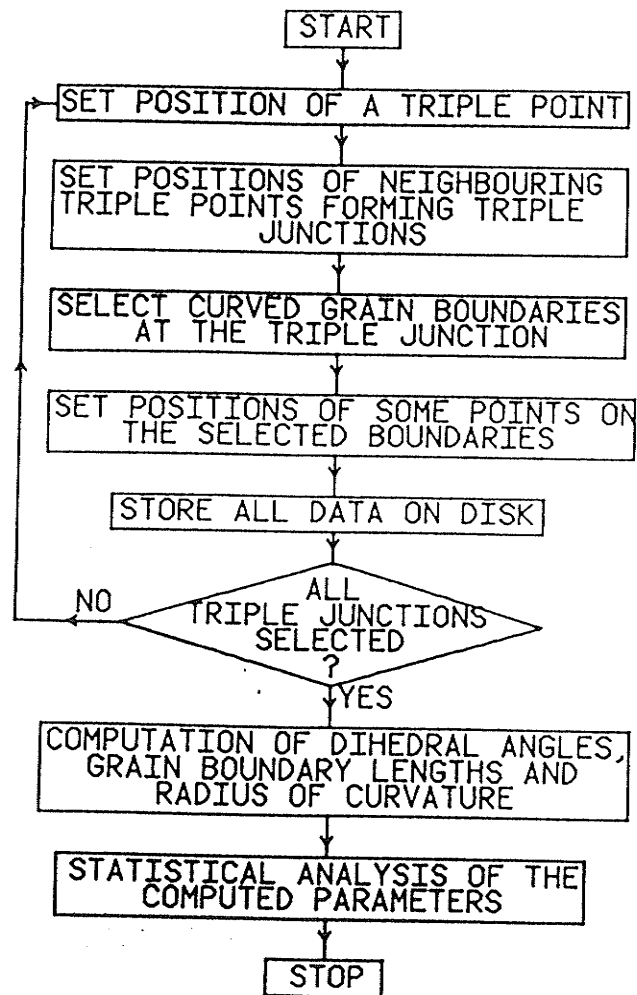


Figure A.4: Flow chart of the program developed for the measurements of dihedral angles, grain boundary length and grain boundary curvature.

## APPENDIX B

### DERIVATION OF THE AVERAGE VACANCY CONCENTRATION NEAR THE TRIPLE POINTS

The average vacancy concentration at distance  $r_o$  from the triple point A (figure 4.11a) is given from equations (4.6a) and (4.7) as follows:

$$\begin{aligned} \bar{C}(r_o) = \frac{C_o}{\pi} \left\{ \int_0^\pi d\theta - \frac{GbV\rho}{2\pi(1-\nu)kT} \left[ \int_0^\pi \sin^2\theta d\theta - \right. \right. \\ \left. \left. r_o^2 \int_0^\pi \frac{\sin^2\theta d\theta}{r_o^2 + L^2 + 2r_o L \cos\theta} + \right. \right. \\ \left. \left. \frac{1}{2} \int_0^\pi \ln \left( \frac{r_o^2 + L^2 + 2r_o L \cos\theta}{r_o^2} \right) d\theta \right] \right\} \quad (B.1) \end{aligned}$$

The solutions to the individual integrals in equation (B.1) are given below:

$$\int_0^\pi d\theta = \pi \quad (B.2)$$

$$\int_0^\pi \sin^2\theta d\theta = \frac{\pi}{2} \quad (B.3)$$

The integral

$$\int_0^\pi \frac{\sin^2\theta d\theta}{r_o^2 + L^2 + 2r_o L \cos\theta} \quad (B.4)$$

in equation (B.1) can be rewritten as

$$\int_0^{\pi} \frac{\sin^2 \theta \, d\theta}{a + b \cos \theta} \quad (\text{B.5})$$

where  $a = r_o^2 + L^2$  and  $b = 2r_o L$ . Making the substitution,  $x = a + b \cos \theta$ , the above integral becomes:

$$- \frac{1}{b^2} \int_{a+b}^{a-b} \frac{\sqrt{X}}{x} \, dx = - \frac{1}{b^2} \left[ \frac{B}{2} \int_{a+b}^{a-b} \frac{dx}{\sqrt{X}} + A \int_{a+b}^{a-b} \frac{dx}{x\sqrt{X}} \right] \quad (\text{B.6})$$

where  $X = A + Bx + Cx^2$ ,  $A = b^2 - a^2$ ,  $B = 2a$ , and  $C = -1$ . The solutions to the integrals of equation (B.6) is given below (Speigel 1968):

$$\frac{1}{b^2} \left[ \frac{1}{\sqrt{-C}} \sin^{-1} \left( \frac{2Cx + B}{\sqrt{q}} \right) + \frac{1}{\sqrt{-A}} \sin^{-1} \left( \frac{Bx + 2A}{|x|\sqrt{q}} \right) \right]_{a+b}^{a-b} \quad (\text{B.7})$$

where  $q = B^2 - 4AC$ . Substituting the values of  $A$ ,  $B$  and  $C$  in integral (B.7), the final solution of the integral (B.4) can be written as

$$\int_0^{\pi} \frac{\sin^2 \theta \, d\theta}{r_o^2 + L^2 + 2r_o L \cos \theta} = \frac{\pi}{L^2 - r_o^2} \simeq \frac{\pi}{L^2} \quad (\text{B.8})$$

for  $r_o \ll L$ .

The integral

$$\int_0^\pi \ln \left( \frac{r_o^2 + L^2 + 2r_o L \cos\theta}{r_o^2} \right) d\theta \quad (B.9)$$

in equation (B.1) can be simplified as

$$\int_0^\pi \ln(a + b \cos\theta) d\theta \quad (B.10)$$

where  $a = 1 + \frac{L^2}{r_o^2}$  and  $b = \frac{2L}{r_o}$ . The solution of integral (B.10) is as follows (Speigel 1968):

$$\pi \ln \left( \frac{a + (a^2 - b^2)^{1/2}}{2} \right) \quad (B.11)$$

Substituting the values of a and b in equation (B.11), the solution to the integral (B.9) is given by

$$\int_0^\pi \ln \left( \frac{r_o^2 + L^2 + 2r_o L \cos\theta}{r_o^2} \right) d\theta = - 2\pi \ln \left( \frac{r_o}{L} \right) \quad (B.12)$$

Substituting equations (B.2), (B.3), (B.8) and (B.12) in equation (B.1), the average vacancy concentration near the triple point A is given by the following equation:

$$\bar{C}(r_0) = C_o \left\{ 1 - \frac{GbV\rho}{4\pi(1-\nu)kT} \left[ 1 - \left( \frac{r_o}{L} \right)^2 - 2 \ln \left( \frac{r_o}{L} \right) \right] \right\} \quad (B.13)$$

Since  $\frac{r_o}{L} \ll 1$ , equation (B.13) is reduced to equation (4.8a, which gives the average vacancy concentration near triple point A:

$$\bar{C}(r_0) = C_o \left\{ 1 - \frac{GbV\rho}{4\pi(1-\nu)kT} \left[ 1 - 2 \ln \left( \frac{r_o}{L} \right) \right] \right\} \quad (4.8a)$$

Similarly, using equations (4.6b) and (4.7) the average vacancy concentration near triple point B (figure 4.11a) can also be derived:

$$\bar{C}(r_0) = C_o \left\{ 1 + \frac{GbV\rho}{4\pi(1-\nu)kT} \left[ 1 - 2 \ln \left( \frac{r_o}{L} \right) \right] \right\} \quad (4.8b)$$